University of Southampton

The integration of chalcogenide materials with nanophotonic circuits for reconfigurable control of light

by
Matthew Delaney

Supervisors:
Prof. Daniel W. Hewak and Prof. Otto L. Muskens

A Thesis for the degree of
Doctor of Philosophy

at the

Optoelectronics Research Centre
Faculty of Engineering and Physical Sciences
December 2020

Abstract

This thesis aims to develop a new conceptual approach for programmable nanophotonic devices, by combining the silicon photonics platform with low-loss phase change materials (PCMs). The approach brings together silicon photonics and phase change technology into a hybrid platform. Digital patterns of pixels are written in the phase change layer using an optical pump laser, which shapes the flow of light by weakly perturbing light transport in the hybrid photonic waveguide. The advantage of this approach is that once set, the phase change materials are self-holding and therefore passive operation would be possible, all at an unparalleled device foot print.

Traditional phase change materials were tested for this application but were found to have an intrinsic absorption loss that prevented their use, as any guiding effects were offset by the lower total transmission. Therefore, in order to achieve the goals set out in this thesis, an entirely new material platform was needed. A large part of the efforts in this project involved the development of a new family of optical phase change materials with ultra-low losses. Sb_2Se_3 was selected as the most suitable material and integrated into a range of photonic devices to characterize the optical and electrical properties before finally realizing a reconfigurable wavefront shaper based on an MMI design. With transmission losses of 100 dB/cm for a straight waveguide clad with 25 nm of crystalline Sb_2Se_3, this represents the lowest loss PCM available, whilst still maintaining a sizable refractive index shift between the amorphous and crystalline phases of Δn=0.77.

A reconfigurable router was demonstrated, capable of reversibly switching the output between two waveguides using a pixel pattern of Sb_2Se_3 distributed in a layer above an MMI. The results in this thesis are the first of their kind and clearly demonstrate the viability of the conceptual approach of freeform patterning of the flow of light using an ultralow-loss phase change material. This work is an initial step towards the development of fully programmable low-loss integrated photonic devices, allowing for optical routing within larger circuits to be realized. This will open up the possibility of low loss, on-chip wavefront shaping applications such as mode converters, neuromorphic computing and LiDAR.

Publications

The following publications are directly relevant to the work presented in this thesis:

M. Delaney, I. Zeimpekis, D. Lawson, D. W. Hewak and O. L. Muskens, "A new family of ultralow loss reversible phase-change materials for photonic integrated circuits: Sb_2S_3 and Sb_2Se_3" Adv. Fun. Mater. 30, 2002447 (jul 2020)

M. Delaney, I. Zeimpekis, H. Du, X. Yan, M Banakar, D. J. Thompson, D. W. Hewak and O. L. Muskens, "Non-volatile programmable silicon photonic router through on-chip wavefront shaping using an ultralow-loss Sb_2Se_3 phase change material." Science Advances, (accepted may 2021)

Other publications:

J. Faneca, L. Trimby, I. Zeimpekis, M. Delaney, D. W. Hewak, F. Y. Gardes, C. D. Wright, and A. Baldycheva, "On-chip sub-wavelength Bragg grating design based on novel low loss phase-change materials" Opt. Express 28, 16394-16406 (may 2020)

N. J. Dinsdale, P. R. Wiecha, M. Delaney, J. Reynolds, M Ebert, I. Zeimpekis, D. J. Thompson, G. T. Reed, P. Lalanne, K. Vynck and O. L. Muskens, "Deep learning enabled design of complex transmission matrices for universal optical components" ACS Photonics 8, 283-295 (jan 2021)

Dedication

This work would not have been possible without the help and support of so many around me. Firstly, thanks must go to my supervisors Dan and Otto, for giving me the freedom to chase ideas as they arose, and the support to see them through. To Nic, for keeping me sane and providing a wealth of great ideas, as well as to the rest of my research groups for their help and enthusiasm. I'm grateful to my flatmates: Wilson, Ulas and Max, for their unending patience in learning far more about silicon photonics than they ever asked to. To all my colleagues in the ORC and Physics departments, who enriched my time there, and to the staff that worked in the background to keep everything afloat.

Finally, to my parents for their love and encouragement in my pursuits, no matter how ill conceived, and to my partner Claire, without who this thesis would likely not exist.

Declaration of Authorship

I declare that this thesis and the work presented in it is my own and has been generated by me as the results of my own original research.

I confirm that:

1. This work was done wholly or mainly while in the candidature for a research degree at this university;

2. Where any part of this thesis has previously been submitted for a degree or any other qualification at this University or any other institution, this has been clearly stated;

3. Where I have consulted the published work of others, this is always clearly attributed;

4. Where I have quoted from the work of others, the source is always given. With the exception of such quotations, this thesis is entirely my own work;

5. I have acknowledged all main sources of help;

6. Where the thesis is based on work done by myself jointly with others, I have made clear exactly what was done by others and what I have contributed myself;

7. Parts of this work have been published as shown in the List of Publications;

Signed: Date:

Contents

Chapter 1

Background

1.1 Motivation

Silicon photonics is an established billion dollar industry, with an expected compound annual growth of 20% [1]. The explosion in the growth of the photonics market is due to the rise of the so-called information age and a need to replace existing electronic solutions. To illustrate the scale of this revolution, it is estimated that 90% of the data ever created has been done so in the last two years [2], with projections only set to increase. This growth has resulted in data centers consuming a significant fraction of the world's electricity and contributing around 2% of all greenhouse gas emissions [3]. The growing interconnectivity of data is expected to transform a wide range of industries such as personalized health care, weather predictions and collective transportation to name a few, with huge benefits to society and the environment.

There are three pillars that are the foundation for the infrastructure needed to support the information industry: data processing, storage and distribution. Photonic technologies play a vital role in the future of each of these fundamental roles, from optical memory [4] to neuromorphic computing [5], integrated optical interconnects and fiber optics [6]. In this work I focus on the third pillar, data distribution. Over the last 50 years, the distances over which it is becoming important to move from an electronic to optical connection are constantly diminishing. Long haul copper cables have been entirely replaced with optical fibers with short-range fiber optics deployed in most neighborhoods and all data centers. Within data centers, due to the high bandwidth required, copper intra-rack connections have also been moved entirely to the optical domain. Soon the industry is anticipating moving towards on-chip optical connections to further increase bandwidth

and speed, and reduce transmission losses as the next stage of this photonic revolution. However, this requires removing the electronic interface between the fiber connections and the data handling, a challenging step that has so far not been widely adopted.

In this work, we address the need to remove completely the electronic interfaces from data networks by developing a new conceptual framework for a reconfigurable, on-chip device based on wavefront shaping in a hybrid silicon - phase change materials platform. This optical router is non-volatile once written and has the potential to enable fully photonic computing without the large space and energy requirements of current photonic technologies. This device represents the implementation of a general planar beam steering technique that has broader applications in optical processing, LiDAR and neural networking to name a few.

1.2 Reconfigurable Silicon Photonics

Reconfigurable photonic networks are a vital component of the next generation of optical technologies to be deployed in data centers [7–11]. This growing need for compact optical devices [12–15], in particular for the fields of nanophotonics, metasurfaces and neuromorphic photonics [16–21] has resulted in a large area of active research. Currently there exists no equivalent to the CMOS gate for photonics [10, 14]. A rewritable photonic element could add the tunability and versatility of an electronic circuit and pave the way for a programmable photonic processor, the ultimate application of these technologies. There is a range of technologies being developed for on-chip programmable photonics, each with its own benefits and drawbacks [22–24]. The most popular approaches are detailed in this section, however this is not an exhaustive review due to the scale of the work in the field [15, 25].

1.2.1 PN junctions

PN junctions are one of the most mature technologies for electrical programmability. The scale of their pervasion through modern life is hard to

comprehend, with 8 trillion transistors being produced per second in 2014 alone [26]. It is no surprise then that a large proportion of switchable photonics research has been devoted to exploiting the same effect in photonics, to take advantage of the existing facilities and knowledge base. Due to their flexibility they have been demonstrated as optical amplitude [27–29], phase [30, 31] or polarization modulators [32, 33]. They function similarly in photonic and electronic circuits, with a variable charge density being used to control the signal. However in contrast to an electronic PN junction, where the electrical resistance of the junction can be used to modulate transmission, in a photonic circuit the charge density can be used to vary different optical properties. The real part (known as electro-refraction) or imaginary part (known as electro-absorption) of the refractive index of a material can be modulated, and used in a phase or amplitude sensitive circuit for control. Traditionally this is through the Pockels effect, the Kerr effect or the Franz-Keldysh effect, however non-linear effects are also possible [34]. Exploiting these effects in different configurations has led to a huge range of optical modulators [35–42]. Due to the fast carrier recombining time these switches can be operated at very high speed, up to 40 GHz [43–45] and beyond [46], and are easily integrated into a hybrid photonic circuit with electronic control. However, the underlying index changes are weak in silicon, and a low loss scalable solution has yet to be demonstrated. Due to the magnitude of the effect, device footprints for optical PN junctions are also a concern, with devices ranging from hundreds of micrometers up to millimeters being common. Electro-refraction is by far the most popular approach, due to the simplicity of the device design and control scheme. There are two approaches to converting this index perturbation to an intensity or phase modulation, which are the goals of most work in this field. By introducing the index perturbation into a phase-sensitive device, such as one arm of a Mach-Zehnder Interferometer (MZI) the interference pattern can be shifted, and through constructive or destructive wave mixing, amplitude modulation can be achieved at the output. Similarly, a resonant structure such as a ring resonator or bus coupled waveguide can be used with the index perturbation used to modify the resonant conditions, allowing the coupling strength of the device to be tuned over a range, again allowing for amplitude modulation. This is a cross platform approach and has been used in silicon [47], silicon nitride [48] and gallium nitride [49] platforms. Dopants have also been introduced to increase the magnitude of the perturbation such as germanium using ion implantation, but the index perturbation remains small in all cases

($\Delta n = 0.01$ [50]), so a large device footprint or very high voltage is needed to achieve a π phase shift for full depth modulation. This, coupled with a continuous energy demand [51] for operation makes these unattractive for large scale circuits. The optical losses are also high, ranging from 10 dB/cm [52] for the low loss high voltage junctions, to 65 dB/cm [53] for the high efficiency gates.

1.2.2 Hybrid polymer-silicon photonic devices

Polymer-based photonic integrated circuits have been explored for a number of years, with this approach garnering more interest in the last decade. The low cost and ease of fabrication, as well as compatibility with flexible substrates offers something that traditional photonic platforms lack. In addition, when doped with organic nonlinear chromophores, it is possible to create electro-optic polymers, with a large range in electro-optic coefficients. This has allowed polymer waveguides to be used in a range of active devices in the same way as silicon [54, 54, 55]. In particular the ability to create waveguides featuring an electro-optic coefficient far higher than that of the typical $LiNbO_3$ [56–59] is a promising prospect in reducing the size and power consumption of on-chip electro-optic modulators with numerous demonstrations [60–62]. However, polymer waveguides are often far less stable than a silicon alternative, with their susceptibility to water and oxygen damage reducing their working lifetimes, despite extensive capping systems designed to protect them. In parallel with silicon based thermo-optic and electo-optic modulators the other drawback is the need for a permanent voltage to maintain any given state. Whilst the power requirements are typically lower than in silicon (due to the higher electro-optic coefficients), their design necessitates a significant heat loss to the substrate, which over a devices lifetime will significantly contribute to the costs.

1.2.3 Thermal modulation

Direct thermal modulation of the silicon is also used to vary the index (known as thermo-optical modulation), in a similar scheme to the PN technologies discussed. Using an embedded electronic heater, the temperature dependence

of the refractive index of silicon can be exploited in a phase sensitive device such as a ring resonator, or MZI. In general, this effect is stronger than electro-refraction for a given power [63], resulting in smaller devices [64–66], however they are still large compared to the waveguide width (the smallest being of the order of 100 μm in length). This decrease in size comes with a lower modulation speed, with typical rise times in the μs regime [67–70] due to the limitations of thermal dissipation, although some sub-μs switching has been shown for more complicated substrate structures [71]. The power consumption is also high, due to the active nature of the device, with the majority of single modulators requiring 10-100 mW [64, 72–79]. It should be noted that the lowest power devices (down to 0.1 mW) often make use of biased voltages which are not included in their switching energies but would contribute to the overall device consumption. The lowest "true" power consumption for a π phase shift is 25 mW [65]. Given that the largest driving forces to move to silicon photonics within data centers is to increase transmission speed and power efficiency, this technique seems poorly suited as the embedded heaters are not discretionary, but heat large areas of the substrate. Large integrated circuits with thousands or millions of embedded heaters would increase, not decrease the thermal output of data centers.

Despite these drawbacks, the simple fabrication and operation have led to large electro-optical networks with thousands of components on a single chip [68, 80–82]. For precise tuning, highly accurate voltage control is needed for the embedded heaters, which can be achieved with modern electronics, further reducing the cost and complexity of a device. The technique also does not benefit from 50+ years of development as is the case for PN junctions, so it is expected that power consumption and device footprint will continue to fall rapidly as this technology advances. The other key advantage is that the thermo-optical index perturbation is limited to the real part in most cases, with the absorption losses typically being in the 1 dB range for a thermo-optical modulator [83]. This relatively low loss is an advantage that most other photonic solutions cannot offer and has enabled larger circuits already demonstrated. The possibility of using the same embedded heaters to switch phase change materials in a similar device is fast becoming a popular approach to benefit from the cheap and easy control from the electrical heaters, and the low power consumption and small device size from the large index shift from the phase change materials. This will be discussed in detail in the photonic phase change section of this review.

1.2.4 MEMS

Microelectromechanical system (MEMS) based optical devices are a promising alternative [84], with a range of different design approaches. MEMS switches are currently in use for optical routing within data centers, the only commercial optical routers to date. Current generation MEMS switches use micro-mirror free space coupling between different fiber for optical switching, with 1100 × 1100 switches available [85]. However these are bulky, expensive and have a limited lifetime of 1-2 years, compared to what an integrated solution could offer. Removing any free space optics is important for stability as well as transmission loss, with current free space systems showing 6dB loss per port coupling, mostly due to the poor coupling efficiency between free space and fiber systems.

Using MEMS in an integrated circuit to tune the coupling of ring resonators is a popular scalable method for on-chip control, with 128×128 [86–88] port count switches and 240×240 [88] switches being demonstrated. In contrast, thermo and electro-modulation have only been extended to 32 port count switches. These devices are based on an Ohmic switch, which can be controlled by electrostatic cantilevers. In parallel with PN junctions and thermo-optical modulation, electronic control is essential for the fast and precise operation of optical MEMS devices. This brings with it the benefits of easily integrated control for hybrid photonic-electric systems, as well as the drawback of being incompatible with a fully photonic circuit. Unlike the static PN junction and thermo-optical modulation, MEMS devices are susceptible to failure from metal fatigue causing cantilever deformation over time. The operating lifetime of these devices is dependent on the individual design and fabrication tolerances, however it is unlikely to provide a solution as robust as a static integrated approach.

With MEMS waveguide actuators, it is possible to avoid the use of ring resonators or MZI's, and directly alter the path of the light using a movable coupling waveguide [89]. This helps to keep these circuits compact [90–93], and enables very low cross talk of -40 dB being common [94–97] with -60dB being possible. However, this is accompanied with an increase in transmission loss in all cases, 1dB per device. Other challenges still remain, as they remain active switches with a constant voltage needed to maintain the de-

flection needed in most devices, and switching speeds are not comparable to the electronic solutions, with current demonstrations using a driving frequency of 214 kHz. The fabrication of MEMS is also non-trivial as it requires many more lithographic steps than conventional silicon photonic circuits to fabricate the complex structures used and they are more sensitive to fabrication tolerances as the movement possible with a nanoscale MEMS device is sub-wavelength. This added complexity increases both the cost of individual circuits, as well as the fabrication failure rate.

1.2.5 Germanium implantation

A degree of reconfigurability has been explored using ion implantation [98, 99]. Here the crystalline silicon structure of a waveguide is broken by implanting larger ions into the lattice, leaving a quasi-amorphous region within the silicon from the kinetic implantation, creating an index perturbation. The silicon can then be annealed to regrow the initial crystalline structure, with the germanium easily incorporated into the lattice due to the same outer shell electronic configuration. This has proved to be a powerful technique in post fabrication device trimming [100], with minimal losses due to the direct index change, without the need for an applied voltage. However, this is not reversible or reconfigurable as the ion implantation which is responsible for the perturbation is not possible for a device in-situ. This reduces the utility to the point of manufacture, or one time use devices. A large prefabricated mesh could be programmed in-situ for a specific application in a similar fashion to a one use FPGA. Another application of this technology could be a large integrated circuit with a common single point of failure. When this failure occurs, an embedded thermal heater could be used to anneal a pre-implanted region, bypassing the failure to a redundant circuit. For photo-lithographic circuits the cost of additional components is only the substrate space they require so it may be possible to greatly increase the working lifetime of a large circuit with a small increase in overall size and cost. This is not uniquely possible with germanium implantation, however it offers the lowest optical losses out of the reviewed approaches, and would be a one-time energy cost. Whilst an interesting and unique approach, implantation is not suitable for reconfigurable devices.

1.3 Phase Change Chalcogenide Photonics

Phase change silicon photonics provides a different avenue for non-volatile, on-chip reconfigurability. By using a silicon waveguide clad with a chalcogenide phase change material (PCM), the effective index of the waveguide is coupled to the index of the PCM via the evanescent field. With an exceptionally large difference in the real part of their refractive index between their phases, (n=4.6 for amorphous GST, and n=7.45 for crystalline GST at 1550 nm, $\Delta n = 2.85$ for GST [101]) PCMs provide a much stronger perturbation than the electro-optical or thermo-optical effects, and for phase stable PCMs they do not require a threshold voltage to stay activated, offering significant power savings over the device lifetime.

Chalcogenide materials have been used in optical systems for over 50 years. Since the discovery of their semiconducting properties in 1955 [102] they have been proposed for use in phase change memory among other data storage techniques [103, 104]. The non-volatile and low power thresholds make these materials ideal for phase change memory, and has been the main focus of past chalcogenide research. The hugely successful CD, DVD and now Blu-ray formats all make use of chalcogenide layers, with a read and write laser to decode/encode data. More recently phase change memory has moved into the electronic domain [105], with commercial PCM solid state storage drives available.

The same qualities that make PCMs attractive for conventional computing have attracted attention from the photonics community. The existing body of research into these materials, in particular $Ge_2Sb_2Te_5$ (GST), as well as the current CMOS compatibility have kick started the field. In the vast majority of PCM photonic devices, the PCM is used as a thin film coating on top of a prefabricated structure such as metamaterials, a waveguide or in critical coupling regions, such as between two bus coupled waveguides. By changing their phase, the associated change in refractive index can be exploited in the same way as the thermo-optical or electro-optical effects have been for a range of applications. There have been some demonstrations of waveguides written directly into bulk chalcogenide substrates [106], however these materials have not been shown to be easily reversible, so are not suitable for reconfigurable circuits.

I will review the most common material families in use today for integrated photonics and discuss the application benefits and drawbacks, then compare the intrinsic material properties of each in Table 1. I do not include details of specific stoichiometric compositions or dopants due to the huge parameter space this offers. In general the fundamental properties of a material are modified by these changes but rarely does this change the material so drastically as to warrant individual discussion. The different stoichiometric possibilities of GST provide a good example of this, with at least 10 different elemental compositions being explored in the literature, all suffering from the same fundamental absorption losses. A notable exception to this assumption would be Ge-Sb-Se-Te (GSST), where despite being from the same material family as GST, it is discussed in detail separately due to the vastly different optical properties.

1.3.1 GST

The dramatic refractive index difference in both the real and imaginary part of GST between the two phases ($\Delta n = 2.85$, $\Delta k = 1.37$ in the C-band) promises compact optical devices ($< 100\ \mu m^2$), which previously only MEMS based approaches could compete with. There are numerous demonstrations of integrated devices, such as single and multi-level photonic optical memory based on GST cells [85, 105, 107–117], photonic modulators [118–126], directional couplers [127], resonance tuning [128, 129], beam steering [130], neural networks [20, 131], metamaterial switches [132–134] and photonic switches, both theoretical [135–137] and experimental [138]. All of these devices are based on using a small volume of GST to modulate a local refractive index. The strong absorption of the crystalline phase is used as the "off" state, as any device with a crystalline cladding becoming highly lossy, compared with an amorphous clad device. The lower loss amorphous state remains as the "on" state, although still with significant optical loss.

Optical memory is perhaps the most obvious application, with a straight waveguide capped with GST able to function as photonic memory with no further fabrication. The memory state is easily distinguishable based on the optical transmission of the two phases [139]. This idea has been taken further by exploiting partial crystallinity in the PCM to act as multi-level

memory [140]. It is possible to crystallize very small regions within a single PCM patch, giving separate addressable levels of photonic memory. Furthermore, Rios *et al.* [140] showed for the first time in-plane switching, using a high power laser coupled into the same waveguide to phase switch the GST, removing the need for a separate "write" laser incident at a normal angle to the chip, creating a fully integrable on-chip system. A lattice of crossed waveguides (also known as a "wood-pile" device) would be the logical evolution of this work and be capable of doing matrix operations simultaneously.

The obvious drawback to the current waveguide configuration is the inability to stack many memory cells within the same optical trace, greatly reducing memory density. Once the first cell is crystallized, the absorption is strong enough to prevent the required intensity for further crystallization from being reached in subsequent patches. Compound optical and electrical control could be used to address this to produce large on-chip memory arrays following a similar scheme to that published by Au *et al.* [141]. The largest issue for using GST in photonic memory is that the loss, in either state, is very high compared with the intrinsic losses of photonic waveguides, with an insertion loss of -30 dB being common [123, 139] in the "low loss" amorphous phase. This limits GST to small circuit designs with frequent and costly amplification. One proposed solution that seeks to minimize the overall loss is to use an MMI to provide a small region of high intensity (at the self-imaging point) to reduce the volume of GST required and therefore the amorphous losses, without compensating on the modulation depth [122, 124].

In contrast to the optical memory and modulators, phase change couplers and tunable switches exploit the change in the real part of effective index to shape the wavefront, compared to using the imaginary part to change the amplitude. By positioning the GST at a critical dimension, such as the gap in a ring resonator, waveguide coupler or on top of a nanoantenna, the index change is used to tune the resonance over an impressive range. However, the losses from even these very small additions are significant and prevent these components from being incorporated into larger networks.

The wide array of literature published on the use of GST in silicon photonics includes reports of a huge range of devices, however there is some confusion about the definition of different types of photonic devices with photonic memory, switches, modulators and routers all being used inter-

changeably to describe two fundamental devices. For the purposes of this work, I shall refer to any planar device which has a single input and output with a controllable intensity as a photonic modulator (photonic memory is a subset of this definition, distinguished only by the ability to passively hold its state, which is a common trait of all GST based devices). Photonic routers are the second type of devices, which do not operate using direct amplitude modulation, but by guiding light to any number of multiple outputs, with minimum insertion losses. A photonic switch is simply a 2-port optical router. Due to the intrinsic losses of all photonic PCMs, a true photonic router has not been realized in the phase change photonics field and is the goal of this work.

1.3.2 GSST

The material $Ge_2Sb_2Se_4Te_1$ (GSST) has recently been proposed as a lower loss competitor to GST, [142] with the selenium addition known to increase the transmission window. Experimental results have show this material performs well in amplitude modulating devices such as MZI's [143], with little to no optical loss in the amorphous phase, whilst maintaining a comparable absorption in the crystalline phase to that of GST. This may provide the improvement that the field has been lacking. This research is still in its infancy, with the initial results published in 2018, so it is unclear if the selenium addition has compromised the switching speed or energy that made GST an attractive material in the first case. It is however likely that this material will continue to be used for amplitude modulation given the impressive 40dB extinction ratio shown for a ring resonator modulator. Whereas GST is academically interesting in a photonic setting, but not commercially viable for large circuits due to the very high insertion losses, GSST could be the future of planar optical amplitude modulation if the published demonstrations can be converted into a packaged product. For photonic routing however, the intrinsic crystalline losses still prohibit a high-efficiency router.

1.3.3 VO_2

VO_2 is another popular phase change material for photonic networks, due to the fast electrical switching speeds [144] and low transition temperature of 68 °C [145]. The metallic state is volatile at room temperature [18] which makes it an attractive material for some applications such as modulation [146] and reconfigurable antennas [147], but presents challenges for others such as optical storage. The optical loss is also an issue for larger photonic circuits with the absorption at 1550 nm in both phases being comparable to GST but with a smaller $\Delta n = 0.5$ [148]. Recent work by Currie *et al.* [149] has shown an improvement in the absorption using atomic layer deposition (ALD) over other deposition methods, however as is the case with GST, the absorption ($k = 0.5$) is still too high for VO_2 to be integrated into larger photonic circuits for phase modulation. One of the key benefits of chalcogenide PCMs is the phase stability, which for a switch can lead to very low per bit power consumption due to passive operation. The low transition temperature (T_c) reduces the switching energies, however for data center use the T_c is too close to operational temperatures for VO_2 to be considered stable, and has been discounted on this basis as a potential material for this work.

1.3.4 GeTe

GeTe was initially investigated for use in optical phase change memory. It exhibits a high melting and glass transition temperature which gives it great stability in both phases, however limits the crystallization speed and raises the switching energy. Because of this it was doped with Sb_2Te_3, another PCM known to be less stable. Eventually the composition of $Ge_2Sb_2Te_5$ was settled on as the best compromise of switching speed and stability. At the time, the optical losses were not considered an important property as long as there was a large index contrast between the two phases. Silicon photonics started to make use of GST due to the common availability and low switching temperatures, with GeTe being largely overlooked, despite a $\Delta n = 1.6$, no absorption at 1550 in the amorphous phase and a relatively low absorption of k = 0.35 in the crystalline phase [150]. These values compare very favorably with GST for low loss applications and are similar to GSST, however there is no published work on the integration of this material with silicon photonics,

perhaps due to this material being bypassed in favor of GST, which was considered the phase change material of choice for non-planar applications. There have however been a few demonstrations of GeTe in free space devices such as optical modulators [151], IR bandpass filters [152], tunable color filters [153] and Q-switched lasing [122], showing that the materials optical properties are suited to the needs of the photonic industries.

The apparent lack of GeTe photonic devices can be partially explained by the high amorphization temperature. In literature the crystallization temperature is quoted to be between 150°C and 230°C, with the most recent work putting the value at 190°C [154], however the amorphization temperature is known to be significantly higher, around 600°C. This presents significant problems for on-chip switching, even with Joule heating. The free space demonstrations all rely on a tight lattice of metal contacts to achieve the required temperatures for phase control. This approach would introduce high losses if used directly on waveguides, and optical switching presents different constraints on device design and footprint. Ultimately an electrically switchable solution would need to be demonstrated, and this may not be possible for integrated GeTe devices if power consumption is limited.

1.3.5 Novel PCMs

Antimony trisulfide (Sb_2S_3) and antimony triselenide (Sb_2Se_3) are alternative low loss chalcogenides to GST, due to their negligible losses in the near infrared spectral range and refractive index difference between the amorphous and crystalline phases. Both materials have been studied for over 50 years for their thermoelectric semiconductor properties [155], and to this day the overwhelming focus of research for these materials is the photovoltaic industry [156–160] due to the low toxicity [161] and band gap in the visible wavelength range. Sb_2S_3 has been explored previously for optical and electric data storage applications, with it being described as a "write once read many" material or WORM [162–165]. At the time it was noted to have no intrinsic losses in the near IR in either phase, the importance of which was overlooked due to the goals of the research. The reason for the lack of reversible switching was cited as sulfur loss causing film degradation. This description as a "write once" material, combined with the lack of focus on

the transparency led to little further development of this material for phase change applications. This classification was recently disputed in work by Dong *et al.* [166] with both electrical and optical switching demonstrated. However, it is important to note that whilst reversible switching was reported, no experimental demonstration of this key result was presented in the published work. The integration of Sb_2S_3 with silicon photonics also proved to be challenging, with an Al-SiN mirror substrate used to enhance absorption and improve thermal conductivity which is unsuited for integrated photonic devices.

The optical properties of Sb_2Se_3 have been well known for many years, and recently there has been some interest in the phase change properties of the material [167]. However this work has always been in the context of electrical applications such as non-volatile memory. Outside of this work, no photonic demonstrations of Sb_2Se_3 have been shown.

1.3.6 Material overview

The key properties of each phase change material have been compiled in Table 1.1. These properties include the n and k values in both phases (as well as the ΔN for easy comparison), phase change speeds, cyclability and volatility. The values presented here are unlikely to be the fundamental limits of each material, but a reflection of the published work in the field. More advanced fabrication techniques or new stoichiometries are likely to improve the materials for specific applications, given the time and resources for additional development. As such, materials that have benefited from more research are further along their development curves. Another important factor to consider is that in many cases the comparisons are not between similar experiments and are provided as a guide of what has been demonstrated, not what is possible only. The crystalline and amorphous n and k values are all confirmed by ellipsometry and so are comparable, however the switching speeds are primarily functions of the device design and switching regime. In the literature they are often compared, with no discussion of the difference. It is possible to demonstrate vastly different "switching speeds" by using different cell sizes. For example, the fast crystallization of GST is achieved using electrically switched cells of the order of 25 nm squared. By comparison, the

values given for Sb_2S_3 and Sb_2Se_3 were measured using an optically switching area of 1000 nm squared, which will be slower due to the larger thermal mass and distance for crystal growth. In this work the material switching speeds are not measured directly, but instead a measure of the cycle speed was made using the optical pulse length required for a phase change. More work is needed to understand the material limitations using time resolved reflectivity measurements.

The cycle durability is used as a measure of the lifetime of these materials. With proper encapsulation, phase change materials can have a shelf life of many decades, as evidenced by DVD's, however they can only be subject to a limited number of phase switches before the change in refractive index is reduced below a useful threshold. This is a function of both the application and the material. For commercial phase change devices, very long cycle durabilities have been demonstrated, with the materials introduced in this work falling far short of the impressive results shown by GST. Finally, there can be large differences between materials that are nominally the same, for example from stoichiometric changes during deposition affecting absorption spectra or changes to the crystal grain size and structure due to different annealing temperatures, which again makes it challenging to accurately compare between materials. A like for like experimental comparison of materials would be needed which goes beyond the scope of the current work.

Table 1.1: Table comparing the key parameters of the most common phase change materials.

		GST	GSST	GeTe [150]	Sb_2S_3 (this work)	Sb_2Se_3 (this work)
Crystalline values at 1550 nm	n	7.91	4.91	5	3.31	4.05
	k	1.03	0.284	0.27	0	2.13^{-4}
Amorphous values at 1550 nm	n	4.56	2.71	3.50	2.72	3.28
	k	0.06	1.23^{-4}	0.02	0	0
	Δn at 1550 nm	3.56	2.20	1.50	0.590	0.764
	Crystallisation time (s)	10^{-8}	10^{-7}	10^{-6}	10^{-3}	10^{-6}
	Amorphisation time (s)	10^{-9}	10^{-7}	10^{-8}	10^{-7}	10^{-8}
	Cycle durability	10^7	10^3	NA	10^3	10^4
	Volatile	No	No	No	No	No

1.4 Thesis Outline

I aim to develop a novel conceptual approach for programmable nanophotonic devices, based on wavefront shaping using a phase change material, such that an incoming signal can be guided towards any port with very low loss, in a single device. To date the majority of integrated photonic research has focused on optical switches/modulators, with optical routing receiving less attention due to the increased complexity. The most popular approaches for photonic reconfigurability are based on meshes of cascading switches and all have an associated large increase in optical losses, device footprint and power consumption compared with this work.

Other attempts at phase change photonic routers based on phase change technology have suffered from the inherent loss of the PCMs used. Here we have developed Sb_2S_3 and Sb_2Se_3 as novel low loss PCMs to circumvent this limit. By annealing amorphous pixels in an otherwise crystalline thin film PCM on top of an MMI, we aim to shape the wavefront within the MMI such that the light is guided towards a selected output. This pattern can be erased and rewritten to change the output intensity, creating an optical router.

A similar approach to MMI wavefront shaping has already been undertaken in reference [168] using a different technique to modulate the refractive index. A pulsed laser was incident vertically onto the surface of a silicon device, varying the refractive index by $\Delta n = -0.25$, using a free carrier injection. The light propagating through the MMI was guided by the effective index created by the free carrier injection. However, this technique has the drawback of only being an ultrafast dynamic change, and requires precise timing between the pump and probe lasers. With a phase change material, the refractive index change is permanent and rewritable, allowing for a continuous probe signal to be manipulated. We shall build on this work towards the goal of a passive optical router. As this is the first demonstration of this technique I will limit the work to a router with a single input and two outputs, however it could be scaled up to many more inputs/outputs.

This thesis sets out by examining the theory of optical waveguiding and, in particular, the behavior of MMI devices as a function of their dimensions in

chapter 2. A brief overview of the most commonly used phase change materials is included in this chapter with the underlying theory for the chalcogenide phase transition.

The basic simulations for the individual photonic elements are presented in chapter 3, with a focus on the simulation techniques used to design and optimize each component. A more detailed explanation of the perturbation modeling follows in chapter 4, where the different approaches used to identify the best performing perturbation patters for a range of devices and applications.

Chapter 5 details the procedures used for device and film fabrication in the cleanrooms as well as the experimental set-up needed for the in-situ testing and characterization of integrated photonic circuits that are presented in the final chapters.

After identifying the need for a new low loss phase change material, the development of Sb_2S_3 and Sb_2Se_3 is described in chapter 6, where the key parameters such as switching temperatures, refractive indices for both phases and optical pulse requirements are presented and compared to existing phase change materials.

The final results for a compact phase tuner and a novel photonic router are shown in chapter 7. Using an MZI with a phase change material cladding above one arm, nearly lossless phase tuning was demonstrated using a compact waveguide length compared to other approaches, with a self-holding but reversible material change. Finally using an MMI, the idea for a phase change perturbation based optical router was demonstrated experimentally, with reconfigurable optical routing between two different outputs achieved with an extinction ratio of 11 dB between the two ports.

Chapter 2

Theory and Method

2.1 Silicon Photonics Theory

This work is the product of two distinct areas of research, silicon photonics and phase change chalcogenides. Conventional silicon photonics is a mature technology with a well established theory, and a wide range of simulation software available. By contrast, despite huge industrial efforts to understand these materials for use in optical storage, chalcogenide PCMs are less well understood with the core mechanisms still under debate. The wide range of elemental compositions and the stoichiometric variation within each composition only adds to this complexity. In this chapter I will first outline the fundamental photonic operating principles and devices that form the basis for chalcogenide integration, before moving on to explore the most current phase change research.

2.1.1 Total Internal Reflection

The theory behind the interaction of light and a material interface which gives rise to waveguide confinement was first described in full by Ibn Sahl in 984, and was since rediscovered a handful of times most popularly by Willebrord Snellius who gave his name to the equation, Snell's law. It can be derived using a number of approaches such as heuristic momentum conservation, Fermat's principle, or as a by-product of Maxwell's equations, but in any case describes the relationship between the refractive indices and angles of incidence for light between two mediums. It makes the assumption that light propagates in straight lines through a homogeneous medium (known as the geometrical optics or ray optics approximation).

$$n_1 sin(\theta_1) = n_2 sin(\theta_2) \tag{2.1}$$

In the case where $n_1 < n_2$, and the angle of incidence (θ_1) is large, Snell's law requires that the sine of the angle of refraction be greater than 1. This is impossible and gives rise to a boundary condition known as total internal reflection, where the light is reflected at a boundary interface as opposed to refracted. The largest possible angle of incidence is known as the critical angle, above which light will be unable to exit the medium and Snell's law can be rewritten in the following form to express it:

$$\theta_c = sin^{-1}(\frac{n_2}{n_1}) \tag{2.2}$$

2.1.2 Dielectric waveguides

The critical angle can be exploited to "trap" light in a medium by injecting it into a structure with a lower index material on all sides at or above the critical angle. Shortly after the invention of the laser, fiber optic waveguides were developed that could transmit optical signals over great distances as shown in figure 2.1. The light is constrained to the core by a small index step change between the core and cladding of the fiber, both of which are made from silica. With the rise in demand for integrated solutions, planar waveguides have also been developed, built on the same principles and typically using silicon as the guiding medium and silica as the cladding, although other platforms exist such as silicon nitride. Different waveguide geometries can be seen in figure 2.2. The large difference in index between the two materials allows for low radius bends without loss, and builds on existing CMOS fabrication capabilities. The most popular waveguide structures are shown in figure 2.2, with the rib waveguide structure being used in this work, where the light is confined to a 220nm thick silicon slab which has been etched back to leave a 500 nm wide, 100nm high rib. Other geometries are possible with the ridge and embedded waveguides operating in the same way as the rib waveguide. The slot waveguide stands apart from the other designs due to the mode being partially confined to a lower index region, between two silicon ridges, neither of which is wide enough to support a mode. The dimensions of these

waveguides are smaller than the wavelength of the light that propagates within in, as such the ray optics assumption is no longer valid and a more complete modal description is required.

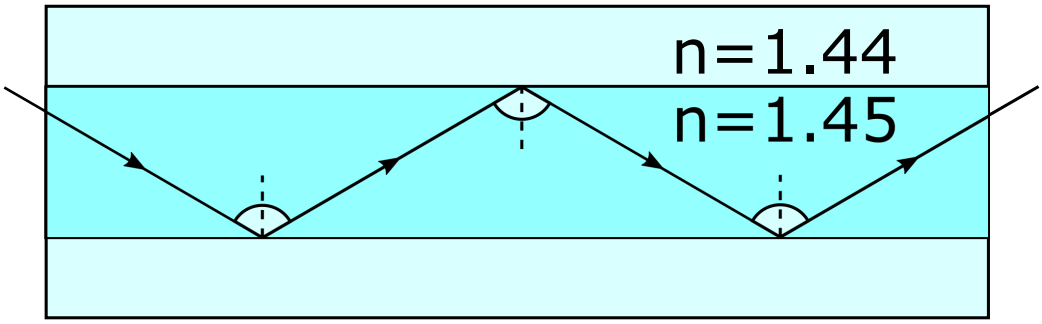

Figure 2.1: The propagation of light in a modern 1550 nm fiber.

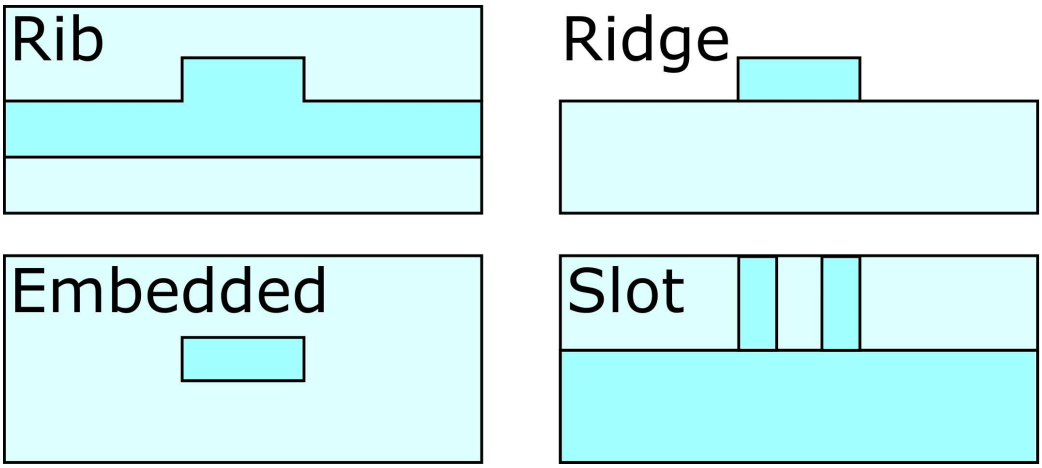

Figure 2.2: The most common types of planar photonic waveguide geometries, where the darker shade represents the higher index material in each case.

A full electromagnetic description of the propagation of light inside photonic structures can be derived from Maxwell's equations, however as non-planar dielectric waveguides do not have analytical solutions (except for the special case geometry of circular optical fibers), I will outline the effective index method which is made use of throughout this work, both for understanding the wave propagation within a device, as well being the method

of choice for 2D approximations of 3D models that effectively reduce the computational requirements in terms of time and memory.

The effective index method assumes that the lateral dimensions are significantly greater than the longitudinal dimensions, and that the vertical index contrast is low. As such the waveguide modes can be approximated by the time dependent wave equation (or Helmholtz equation) [169]:

$$\nabla^2\Psi(x,y,z) + k_0^2 n^2(x,y)\Psi(x,y,z) = 0 \tag{2.3}$$

Where Ψ represents any of the field components. Due to the invariance in the z direction, the z dependence of Ψ is given by

$$\Psi(x,y,z) = \psi(x,y)e^{-i\beta z} \tag{2.4}$$

This reduces equation 2.3 to

$$\nabla_{xy}^2\psi(x,y) + (k_0^2 n^2(x,y) - \beta^2)\psi(x,y) = 0 \tag{2.5}$$

By writing $\psi(x,y) = F(x,y)G(y)$ where $F(x,y)$ is a slowly varying function of y, such that

$$\frac{\partial F}{\partial y} = 0 \tag{2.6}$$

equation 2.5 becomes

$$\begin{aligned} &F(x,y)\frac{d^2G(y)}{dy^2} + 2\frac{\partial F(x,y)}{\partial y}\frac{dG(y)}{dy} + G(y)(\frac{\partial^2 F(x,y)}{\partial x^2} + \frac{\partial^2 F(x,y)}{\partial y^2}) + \\ &(n^2k_0^2 - \beta^2)F(x,y)G(y) = 0 \end{aligned} \tag{2.7}$$

which reduces further to

$$\frac{1}{G}\frac{d^2G}{dy^2} + \frac{1}{F}\frac{\partial^2 F}{\partial x^2} + (k_0^2 n^2(x,y) - \beta^2) = 0 \tag{2.8}$$

By separating the variables and introducing the y-dependent variable $n_{\text{eff}}(y)$ due to the weak y-dependency of $F(x,y)$ we recover

$$\frac{1}{F}\frac{\partial^2 F}{\partial x^2} + k_0^2 n^2(x,y) = k_0^2 n_{\text{eff}}^2(y) \tag{2.9}$$

$$\frac{1}{G}\frac{d^2G}{dy^2} - \beta^2 = -k_0^2 n_{\text{eff}}^2(y) \tag{2.10}$$

To apply these equations, first the waveguide is divided into sections which are assumed to have a refractive index profile independent of y, reducing equation 2.9 to

$$\frac{\partial^2 F_i}{\partial x^2} + k_0^2 n_i^2(x) F_i = k_0^2 N_{eff,i}^2 F_i \tag{2.11}$$

Solving this equation gives the effective index distribution $n_{\text{eff}}(y)$ which can then be used to solve 2.10 to recover the propagation constant β and the mode profile $G(y)$:

$$\frac{d^2G}{dy^2} + (k_0^2 N_{\text{eff}}^2(y) - \beta^2)G = 0 \tag{2.12}$$

2.1.3 Multi-modal Interference Theory

Multimode interference devices (MMIs) have been under investigation for over three decades due to their use as switches [170], modulators [171], balanced coherent receivers [172] and ring lasers [173]. They are small, easily fabricated, polarization insensitive [174] and importantly show self-imaging

points for given geometries which simplifies their design and enables extremely efficient signal splitting. If the effective index could be modulated, their self-imaging points will be changed, providing a powerful tool for integrated optics.

A multimode interference device is built around its inherent property of self-imaging points. Self-imaging points within a slab waveguide were first described by Bryngdahl in 1973 [175]. He showed that for a given input field profile, it is reproduced in single or multiple images at periodic intervals along the propagation direction of the waveguide. A thin slab waveguide only supports a single mode in the transverse direction, so the propagation of the light can be investigated in a 2D regime. Throughout this work I will refer to MMI devices as $M \times N$ devices, where M is the number of inputs, and N the number of outputs of the device.

An MMI device has a width that can support many modes. The interference of these modes leads to the intensity patterns that are exploited to create high efficiency splitters by positioning output tapers (to increase the coupling efficiency) at points of high intensity. To calculate the optimum length for an unperturbed device we start with the dispersion equation for a rib waveguide of width W that can support m modes ($\nu = 1, 2, 3...(m-1)$) at a free-space wavelength λ_0.

$$\left(\frac{(\nu+1)\pi}{W}\right)^2 + \beta_\nu^2 = k_0^2 n_r^2 \tag{2.13}$$

Where the first term is the lateral wavenumber ($k_{y,\nu}$) squared and β_ν is the propagation constant, n_r is the effective index of the waveguide. (A full derivation of this is beyond the scope of this work, and has been conducted by Lucas B. Soldano and Erik C. M. Pennings [170].)

By using the binomial expansion with $(\frac{(\nu+1)\pi}{W})^2 \ll k_0^2 n_r^2$ the propagation constant can be found as

$$\beta_\nu \simeq k_0 n_r - \frac{(\nu+1)^2 \pi \lambda_0}{4 n_r W^2} \tag{2.14}$$

Defining L_π as the beat length between the two lowest-order modes

$$L_\pi = \frac{\pi}{\beta_0 - \beta_1} \simeq \frac{4n_r W_e^2}{3\lambda_0} \tag{2.15}$$

we can write the propagation constants spacing as

$$(\beta_0 - \beta_\nu) \simeq \frac{\nu(\nu+2)\pi}{3L_\pi} \tag{2.16}$$

With a field profile of $\Psi(y,0)$ input at $z = 0$, a modal field distribution of $\psi_\nu(y)$ is found for all modes:

$$\Psi(y,0) = \sum_\nu c_\nu \psi_\nu(y) \tag{2.17}$$

The field excitation coefficient c_ν can be estimated using the overlapping integrals

$$c_\nu = \frac{\int \Psi(y,0)\psi_\nu(y)dy}{(\int \psi_\nu^2 dy)^{0.5}} \tag{2.18}$$

and assuming there are no unguided modes (a reasonable assumption for a slab structure), the input field becomes

$$\Psi(y,0) = \sum_{\nu=0}^{m-1} c_\nu \psi_\nu(y) \tag{2.19}$$

At a distance z this becomes

$$\Psi(y,z) = \sum_{\nu=0}^{m-1} c_\nu \psi_\nu(y) exp[i(\omega t - \beta_\nu z)] \tag{2.20}$$

From this, it can be found that at

$$L = \frac{1}{N}\left(\frac{3L_\pi}{4}\right) \tag{2.21}$$

there will be N-fold images for the first time, where $N \geq 1$ are integers with no common divisor. So for a 1 × 2 MMI silicon rib waveguide to function as a 50/50 splitter with a width of 6 μm at 1550nm, the length should be 32 μm, and doubling this length should recover the initial input field. Simulating a 64μm device does indeed show two high intensity areas 32 μm from the input, and a self-imaging point at the full length of the device (Figure 2.3).

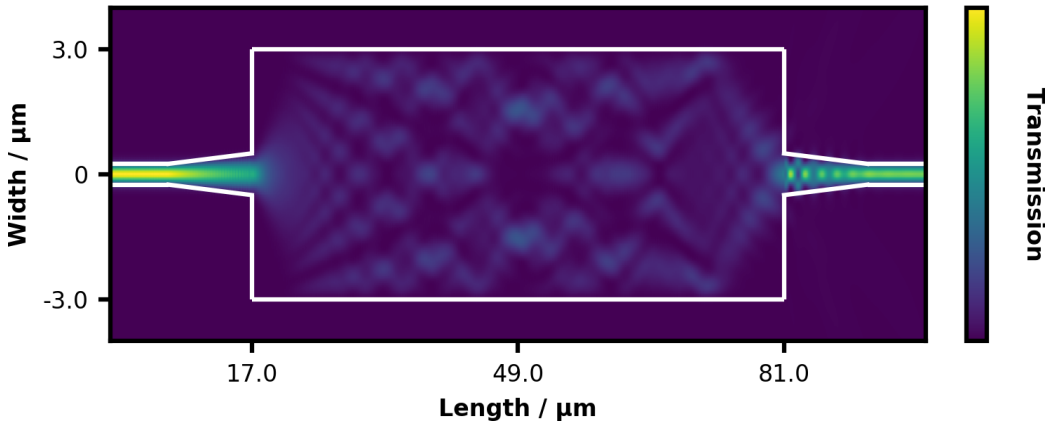

Figure 2.3: Intensity distribution for a 64 μm long MMI, showing a self-imaging point.

2.2 Chalcogenide phase change materials

The underlying mechanics of chalcogenide phase change materials have been the subject of intense research for several decades. Despite the large variety of commercial phase change technologies such as rewritable CD's, DVD's and RAM there is still no consensus on the exact structural changes that are responsible for the bistable phases of these materials. The basic principles

are well understood and this section briefly outline the most popular theories to explain the core mechanisms, however this quickly falls outside the scope of this work. Due to the lack of research into the transitions within Sb_2S_3 and Sb_2Se_3 I will only focus on GST and GeTe, as they have been extensively studied by Raman, XRD and EXAFS spectroscopy, as well as ab initio and X-ray Absorption Near Edge Structure (XANES) simulations.

The property which makes chalcogenide phase change materials so useful is the ability to exist in different stable states at the same temperatures for years at a time, and for each state to be thermally accessible from the others at achievable temperatures. At its most basic level this is due to the atomic rearrangement of the PCM being dependent on both time and quench rate during cooling from above its glass transition temperature (T_g). There are other factors that effect this ability, with the PCM thickness and adjacent interface materials being almost as important for reversible phase change as the material choice.

The common explanation given is that when a PCM is heated to above its T_g, it can cool via two different routes. Firstly, if the quenching rate is slower than the crystallization speed, the nucleation sites within the material can grow a crystalline structure with long range order, allowing the atoms to rearrange in an energetically favorable lattice. The crystal size is proportional to the number of nucleation sites and the cooling rate, with a slower rate or fewer nucleation sites causing larger crystals to grow. If the quench rate is faster than the crystallization speed, the material can be cooled fast enough to "trap" atoms in their melted disorganized state, or the amorphous state as shown in figure 2.4. If that is the case then there is no long range order, changing the properties of the material. So long as the T_g is not exceeded, the internal energy of the material is not sufficient to overcome the bonds in either case, and no further rearrangement is possible.

Chalcogenides are not the only materials in which this is possible. In fact any crystalline material is theoretically capable of this reversible phase change, with phase change silicon now being explored due to the potential benefits it would offer [176]. In contrast to the germanium implantation discussed in section 1.2.5, this is direct thermal access of the amorphous and crystalline silicon. So why are the chalcogens the only materials that have been considered PCMs until recently? The issue for many materials is the

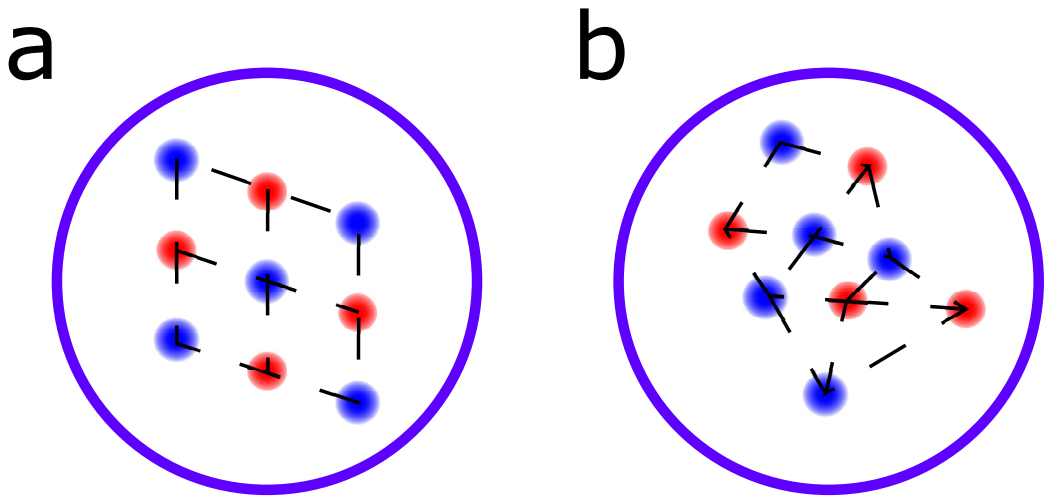

Figure 2.4: Illustration of the two phases of a hypothetical phase change material, (a) crystalline (b) amorphous.

quench rate required for amorphization is often unachievable, at least with current approaches. In the case of silicon, a rate of 950 Kelvin per 10 ns is required. This was achieved with a high power nanosecond laser, preventing this technique from being developed outside of a laboratory for now. In the case of the chalcogens, the quench rates (and T_g) are sufficiently low to be easily accessible through optical or thermal heating.

It is not well understood which property of chalcogenides separates them from and other glassy materials in terms of amorphous quench rates, however the most widely supported theories all center around the importance of vacancies within the crystal lattice [177–180]. Initial studies agreed that the crystalline structure of $Ge_2Sb_2Te_5$ consists of two different structures depending on the exact cooling profile and interface geometries. It was been reported to have a meta-stable rocksalt face centered cubic (FCC) structure or a stable hexagonal structure [181], confirmed by electron diffraction and X-ray diffraction. The conclusions were that the 20% vacancies within the lattice allowed for the easy transition between the crystalline phase and an amorphous phase due to the extra space enabling a higher degree of element migration at lower temperatures. More recently in 2004 this was disputed by Kolobov *et al.* [182]. In their work, it was found that there was no overall rocksalt structure, but well defined, rigid building blocks with random ori-

entations. In the crystalline phase, a model based on the rocksalt structure was used as a starting point for interpreting the results of X-ray absorption fine-structure spectroscopy (XAFS), and good agreement was found between the model and experimental results for the Te-Ge and Te-Sb bonds, with no Sb-Ge bonds detected. Additionally, the second-nearest neighbor Te-Te bond resulted in a predicted peak. However, their results differ from the basic model with an overall intensity decrease, suggesting that the rocksalt coordination number (the number of atoms that a the central atom holds as its nearest neighbor in a crystal structure) was under filled by a factor of 2 or more. Furthermore, the relative mean-squared displacement of the Te-Ge and Te-Sb bond lengths were lower than predicted, suggesting that the Ge and Sb atoms deviate from a rocksalt structure in a correlated manner with respect to the Te atoms, as is the case for ferroelectric GeTe, which exists as a distorted rocksalt-like structure. This is further supported by the similarities in bond length observed in both materials for the Te-Te bonds as a result of a buckled lattice. The shorter bonds are more rigid and provide anchoring points for the local structure, leading to the hypothesis of rigid building blocks arranged with random orientations, and explaining the under filled coordination number as many atoms would not be able to fill their valence shells. These missing electrons must be donated to the Ge/Sb from Te orbitals, creating vacancies. The authors acknowledged that this is a simplified view, but none the less it strongly suggests that the vacancies are an intrinsic part of the GST structure. Increasing the Ge/Sb atomic concentrations does not reduce these vacancies, but accumulate at grain boundaries, again pointing towards the vacancies being integral to the structure [183, 184].

To complete this picture, we must also consider the amorphous structure, which until this point has been referred to as a disorganized structure. This is not entirely true, again with the bond lengths telling an interesting picture. Unexpectedly the Te-Ge and Te-Sb bonds are shorter and stronger (as measured by the Fourier transform of k-space EXAFS data), while the Te second-order neighbor peak is much weaker, but not removed. It is expected that for a three dimensional covalently bonded solid the bond length would increase in the amorphous phase due to a worse packing fraction [185]. There is also an associated increase in the density of the GST [186]. This can be explained as, when heated above the T_g the inter-block bonds are broken, resulting in stronger intra-block bonds and an increased short range order compared with the crystalline phase. Raman spectroscopy provides evidence

for this as the modes are more rigid in the amorphous phase as compared with the crystalline phase. XANES simulations show that the closest agreement with experimental results can be found where the Ge atoms are able to fill its preferred tetrahedral surroundings, thus occupying octahedral and tetrahedral symmetric positions in the crystalline and amorphous phases respectively. The large thermal stimulation required for amorphisation, breaks the weaker bonds and allows the Ge atoms flip into the tetrahedral position. (Figure 2.5) This is only possible due to the vacancies within the crystalline structure and is the cause of the large shift in optical and electronic properties of GST in each phase, as a result of the change to hybridization from crystalline p-type bonding to the amorphous sp^3 hybridization.

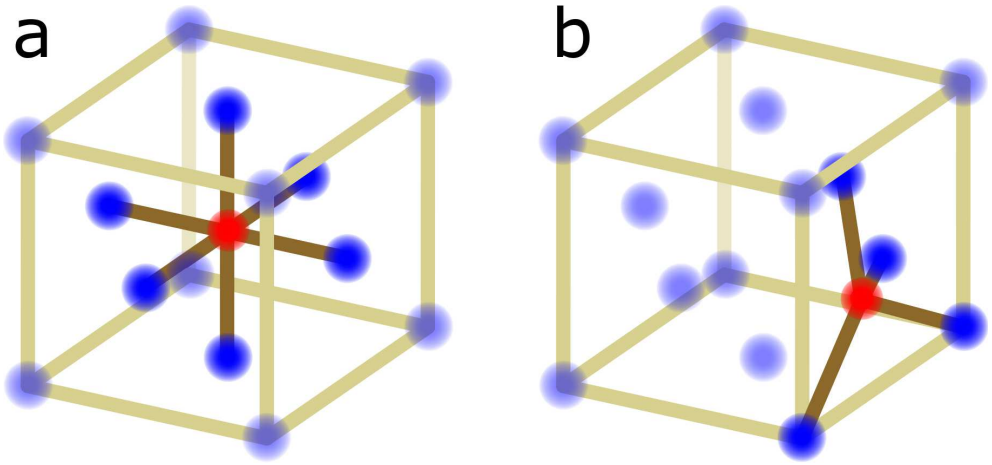

Figure 2.5: Local structure of the GST in the crystalline (a) and amorphous (b) phases with the red atom representing the Ge atom within a GST lattice. The Ge atom can be seen to transition between an octahedral and tetrahedral configuration for the crystalline and amorphous phases respectively.

,

As noted in the textbook "Chalcogenide Glasses" [187], the switching mechanics become more complex when the entire environment is considered. The crystallization is a two step process, initiated by crystal nucleation then propagated by crystal growth. For thin films, the nucleation can be homogeneous or heterogeneous if the volume under discussion is in contact with a preferential nucleation site, such as an impurity or boundary surface. Where an impurity or boundary surface is present, there is an associated (Gibbs)

free energy, reducing the barrier energy for nucleation. If a PCM film is only several times thicker than the internal lattice constant, then these interface effects can dominate the crystallization. High resolution TEM reveals nanocrystals of 1-2 nm in size in a thin (20 nm) amorphous GST film, so it is safe to assume the critical nuclei is smaller than this. Classical approaches to modeling a heterogeneous nucleation mechanisms reply on defining a volume bound by a substrate and a wetting angle. However where the critical nuclei size is similar to that of the lattice constant this method breaks down as a wetting angle is only valid for macroscopic approximations. Bërangére sets out a new approach, assuming the critical crystalline embryo is cubic, and is discussed in detail in Chalcogenide Glasses, Ch 18 [187]. He finds that the level of poly-crystallinity for an optically annealed spot is directly related to the substrate interface material and that the crystallization time increases exponentially for film thicknesses below 10 nm.

So far I have only discussed the theory of GST phase change, due to the wide range of research into the material. The use of Sb_2S_3 and Sb_2Se_3 as phase change materials has been limited up until now, with most of the work in the field focusing on the capabilities of the materials over the fundamental dynamics. It is likely that the same vacancy arguments hold true for these chalcogens as well however, given the uncertainty of the mechanisms for GST, a material that has been used for over 50 years in a wide range of devices, it seems unlikely that a complete understand is within reach. I will present a quick overview of the work towards an understanding of the dynamics of Sb_2S_3 and Sb_2Se_3 as a starting point for future investigations. I hope that as the potential of these materials is discovered, it will create the drive to theoretically understanding these new materials from a photonic perspective.

When Sb_2S_3 was first introduced as phase change material in 1995 [188], several different phases were presented as thermally accessible, with orthorhombic and tetragonal structures reported by x-ray diffraction. Beyond identifying the temperatures for each structure there was little focus on the atomic arrangement, with XPS being used to show antimony and sulfur loss during heating, which resulted in the WORM (write once, read many) description. More recently, the atomic structure of Sb_2S_3 was investigated using high pressure Raman spectroscopy and XRD [189], and both Sb_2S_3 and Sb_2Se_3 being studied by the same techniques [190]. These studies showed two consistent phase transitions at pressures of 5 and 15 Gpa, whilst a full return

to the amorphous phase was seen after full decompression. The conclusions were that these transitions are a result of strong phonon-phonon coupling resulting in a change to the electronic band gap. The strongest evidence for the presence of a semi-ordered amorphous phase with vacancies (or defects) resulting in the phase change properties comes from studies into $K_2Sb_8S_{13}$ (KSS) [191], where analogous to GST, an increasing degree of short range order was seen in the two identifiable amorphous phases. The large band-gap change between the amorphous and crystalline phases was compared to the shift seen for GST (where the authors attributed the shift to the change in coordination number and geometry as the germanium coordination transitions from octahedral to tetrahedral). The authors propose that unlike the GST, the shift seen in KSS is more dependent changes to orbital overlaps between the phases. As the exact structural changes that underpin the extraordinary band-gap change are not fully understood I expect there will be significant work in this direction as the capabilities of Sb_2S_3 and Sb_2Se_3 as photonic phase change materials becomes clear.

Chapter 3

Numerical Modeling

3.1 Introduction

Non-planar dielectric waveguides do not have analytical solutions for their mode structure, except for a few structures exhibiting radial symmetry, such as circular optical fibers. [192] Numerical methods however can be used to solve the modal propagation of electromagnetic radiation within a photonic structure. In this work, a finite difference time domain (FDTD) solver was used as part of the Lumerical software package, which I will outline below.

The most comprehensive, and resource heavy method is the full 3D FDTD solver. To use this solver, an accurate model of the structure is created in the simulation environment. This is a full representation of the device environment including the material properties and dimensions as well as the optical source configuration. The solver breaks the simulation into a 3D mesh, where each cell is significantly smaller than the wavelength of the light source. Using a predefined electromagnetic source as the initial condition, the time-dependent response is calculated by solving Maxwell's equations for light propagation in each cell and using the results of the first cells as the inputs to the adjacent cells. With a suitably small mesh cell size, this provides the best agreement between simulated and experimental results. However, the main drawback is the computational cost, with the memory requirements scaling with volume $(\lambda/dx)^3$ and the simulation time with volume $(\lambda/dx)^4$. This makes it impractical for optimizing devices, or testing broadband responses, as the run time for a single iteration can quickly reach multiple days. Reducing the mesh accuracy is not a viable approach beyond a certain point as there is an associated decrease in correlation with a real device, particularly if the mesh size is comparable to feature sizes.

Due to the high computational demands associated with full 3D simulations, often it is desirable to approximate the system. For planar waveguide geometry, where there is little coupling between different supported slab modes, it is a reasonably good approximation to assume a 2D effective model description. This is called the effective index method and works by solving the effective index of the device in the z-axis, reducing the model to a 2D model, where simulation time scales with volume $(\lambda/dx)^3$ as opposed to $(\lambda/dx)^4$ for the full FDTD simulation. For the purpose of the modeling in this thesis, the x-axis is always the direction of propagation through a planar device, the y-axis is the lateral dimension of the planar model and the z-axis is the vertical dimension from the substrate to the cladding, as seen in the introduction. Since a mode propagating through a 2D structure only experiences the effective index of the device, this method still provides a high degree of accuracy, but with a short enough run time to allow for parameter optimization. A full 3D simulation should however be used to confirm the final device's results response, as the assumptions of the 2D model may not be valid for some designs. To simulate the response of a larger optical circuits composed of many individual devices, the scattering matrix (S-matrix) for each device can be extracted from simulations, which maps the input modes with the output modes. The S-matrices can then be multiplied together to quickly calculate the circuits behavior. These S-matrices were not used in this work, but provide a route towards designing larger programmable circuits based on the results seen in chapter 7.

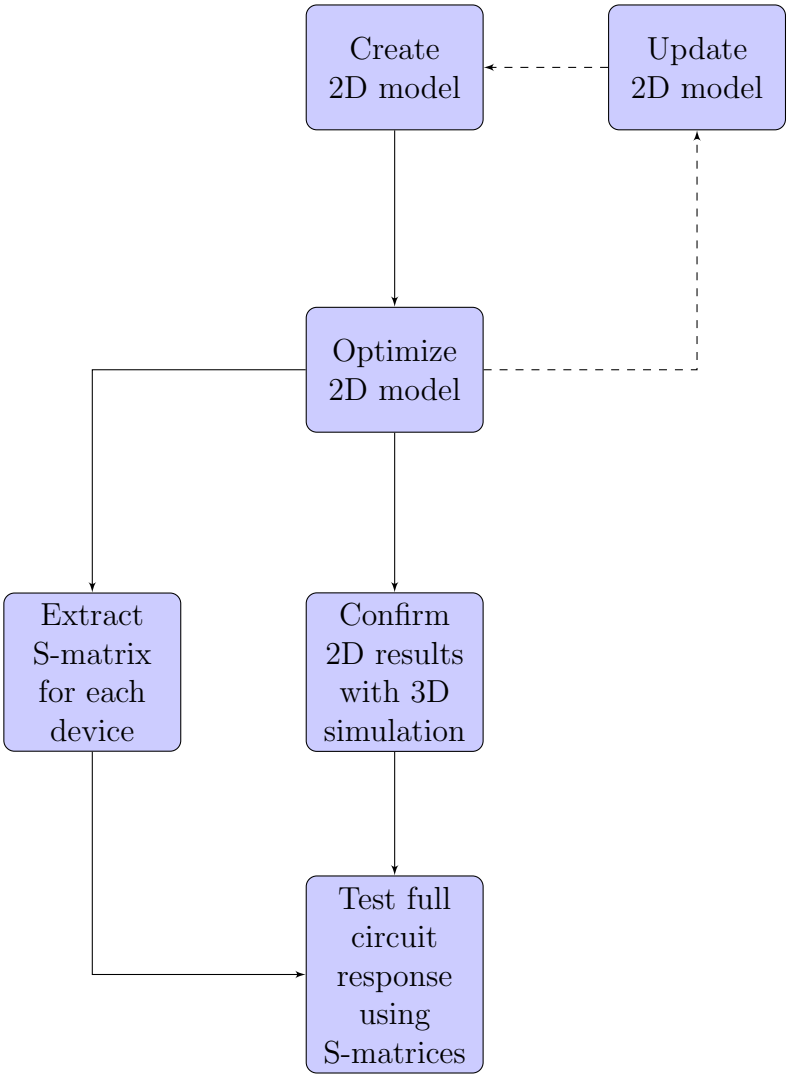

Figure 3.1: Work flow for silicon photonic design using the Lumerical software package.

In the following, a number of basic elements in the integrated photonics toolkit are described in more detail.

3.2 Planar optical waveguides

3.2.1 Finite difference eigenmode solver

The electric field intensities within straight rib waveguides were modeled using the 2D effective index approach. Initially the supported modes of a structure are calculated using a single slice through the structure, perpendicular to the direction of propagation. This approximation assumes translational invariance of the modes, which is valid only for structures with no variation in the propagation direction, however multiple slices could be used to model the coupling of the mode over adiabatic dimension changes. All the waveguides modeled in this section shared the same geometry, and were capped with a thick (250 nm) SiO_2 layer above any PCM layers unless otherwise stated. A 100 nm layer of silicon with a 500 nm wide, 120 nm high rib of silicon is built on top of an infinitely thick SiO_2 layer as seen in figure 3.2, a good approximation for a device with several microns of capping material. The mode is well confined to the center of the rib structure.

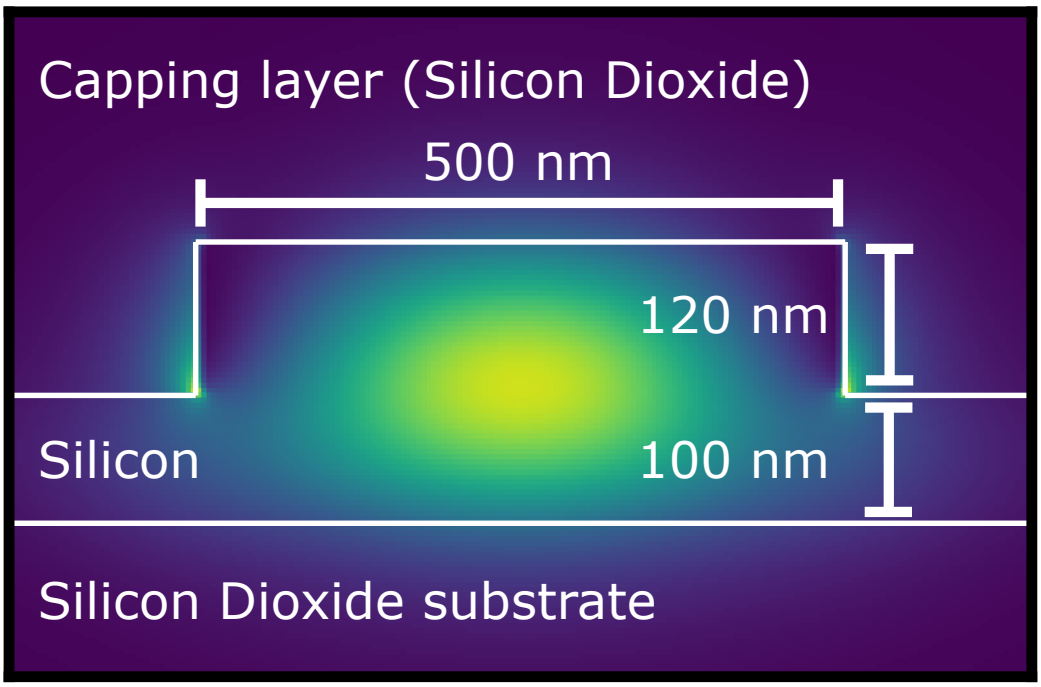

Figure 3.2: Geometry of a single-mode TE rib silicon-on-insulator waveguide.

Since the deposition techniques used to deposit a PCM would always leave some thin films to the side of the waveguides, whenever another material is simulated above the waveguide, it will also be simulated in the trenches on either side of the rib waveguide to better match the fabricated devices. This is included in all the models of rib waveguides. The materials deposited directly onto the waveguide can have a large effect on the modal confinement and propagation loss of the waveguide, although with precise e-beam lithography the size of the affected area can be minimized.

25 nm thick cladding layers were simulated above a straight TE waveguide with a thick (250 nm) SiO_2 capping layer as seen in Figure 3.3. The modal overlap with an unclad straight waveguide was calculated and used to compare how well the mode is confined to the silicon waveguide. The mesh cell sizes were the same in all cases, being 2×1 nm in the y and z directions respectively, providing enough data points throughout the thin PCM films. The amorphous films (Figures 3.3 a,c,e) all performed well as expected, with GST showing the lowest overlap, due to the high index cladding pulling power

out of the silicon. However, the film is not thick enough to support a new mode. The Sb_2S_3 gives the best overlap, as the index is lower than silicon so it acts in the same way as the silica capping. The Sb_2Se_3 has an index similar to that of silicon, so acts as an enlarged waveguide. This reduces the overlap with a silicon waveguide, however the difference is due to the light being able to propagate in both materials without any additional losses. The increased modal overlap with the PCM layer, as compared with the Sb_2S_3 clad waveguide, should increase the effective index change between the two phases of the Sb_2Se_3, leading to a stronger guiding effect in a device.

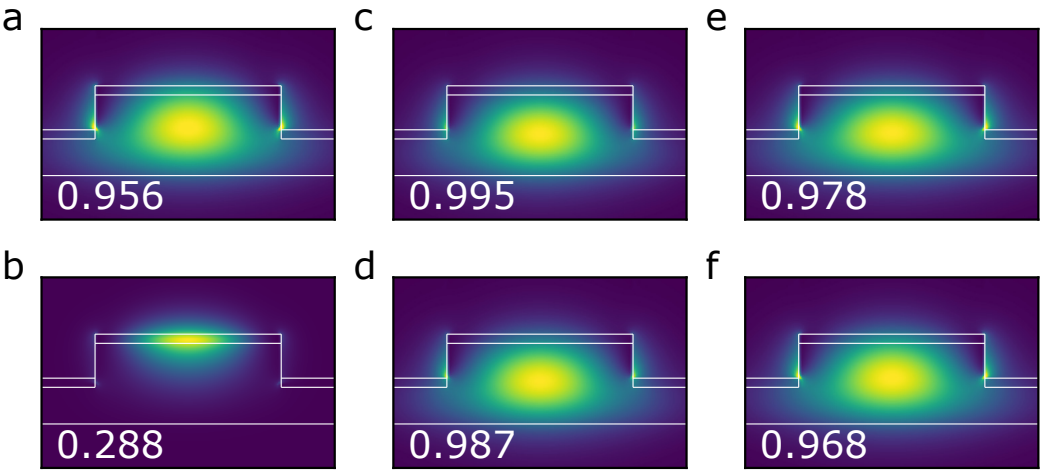

Figure 3.3: Normalised intensity distribution of the fundamental TE mode within silicon rib waveguides with different 25 nm thick cladding. The modal overlap between the different results and an unclad silicon waveguide is shown in the bottom left of each panel, with 1 being a perfect mode overlap. (a) Amorphous GST. (b) Crystalline GST (c) Amorphous Sb_2S_3 (d) Crystalline Sb_2S_3 (e) Amorphous Sb_2Se_3 (f) Crystalline Sb_2Se_3

A different story is seen for the crystalline films (3.3 b,d,f), with the GST clad waveguide having the lowest mode overlap of all the materials. Due to the high refractive index compared to silicon, the mode propagates inside the GST layer where the absorption losses are orders of magnitude higher than the other PCMs. The crystalline Sb_2S_3 and Sb_2Se_3 perform similarly to each other, due to both having an index slightly higher than the silicon, allowing a larger proportion of the power to propagate along the walls of the

waveguide and in the PCM layer as compared with a bare silicon waveguide.

If the thickness of GST is reduced to 10 nm or below, it is no longer thick enough to support a mode even in the crystalline phase, and the light once again propagates inside the waveguide. However this reduces any effective index change, and is still highly lossy, as a significant proportion of the intensity is pulled up into the highly lossy cladding. It is for this reason that all silicon photonic devices with GST films use a 10 nm thick layer.

3.2.2 Mesh accuracy

Having confirmed that the modified waveguides could support a fundamental mode in the silicon (except in the case of a thick GST layer), the waveguide losses were modeled using a 2D FDTD solver. Unlike the mode intensity modeling, where only a single slice was simulated at a high mesh setting, there were many parameters of interest such as the effects of PCM thickness or wavelength on the transmission losses that could be quickly calculated. As such it was necessary to test a range of mesh settings to find a reasonable convergence between result accuracy and run time. A 10 μm long SOI rib waveguide was modeled using the same geometries as figure 3.2, both with and without a PCM cladding above the waveguide and run with a range of mesh settings. The mesh accuracy setting is a constant from 1 to 6, with 1 being a coarse mesh, and 6 being a fine mesh (giving the best results). This setting increases or decreases the average number of mesh cells per wavelength in the simulation, however the software constructs an appropriate non-uniform mesh density based on the geometry and material index, with higher index materials or material interfaces having a higher mesh density. Because of this, the meshing will vary between different models, so it is rarely an exact comparison. It is possible to specify a uniform user-defined mesh with a well understood, linear change between each simulation, however this is not as trivial as it first seems, as decreasing the mesh cell size can result in mesh cells that contain a material interface. Since the average result for the whole cell is used this can lead to large losses being observed for the surfaces between different materials, or a divergent result prematurely ending the simulation as optical power is unaccounted for. The internal meshing function takes this into account to automatically generate a suitable mesh.

The automatic meshing was used in all cases to ensure the simulations ran without divergence errors.

The convergence testing was run on a bare silicon waveguide and a 25 nm thick amorphous GST clad waveguide to test the different loss regimes from very low loss (Si) to high loss (GST). As can be seen in figure 3.4, the silicon waveguide converges more quickly (due to the lower refractive indices present in the model), and after mesh setting four there is little improvement in terms of accuracy, with even the first 3 levels of accuracy providing a good result. A different story was seen for the GST clad waveguide, where due to the very large step-index change and tightly confined mode within the GST layer, increasing the density of mesh cells drastically changes the absorption losses measured. This is because the number of mesh cells within the thin GST layer corresponds to the fidelity of the electric field, and therefore calculated absorption. The first mesh cell accuracy provides a result with 12% transmission, a huge error from the converged result of 58%. As there is only a single mesh cell in the GST layer in the z-direction, the intensity calculated is the sum of the entire electric field. As more mesh cells are added, the model is better able to account for the power that propagates just outside the GST layer, or within the layer but at a lower intensity. By a mesh setting of 4, again the results are reasonably well converged, so this was chosen for all future waveguide models.

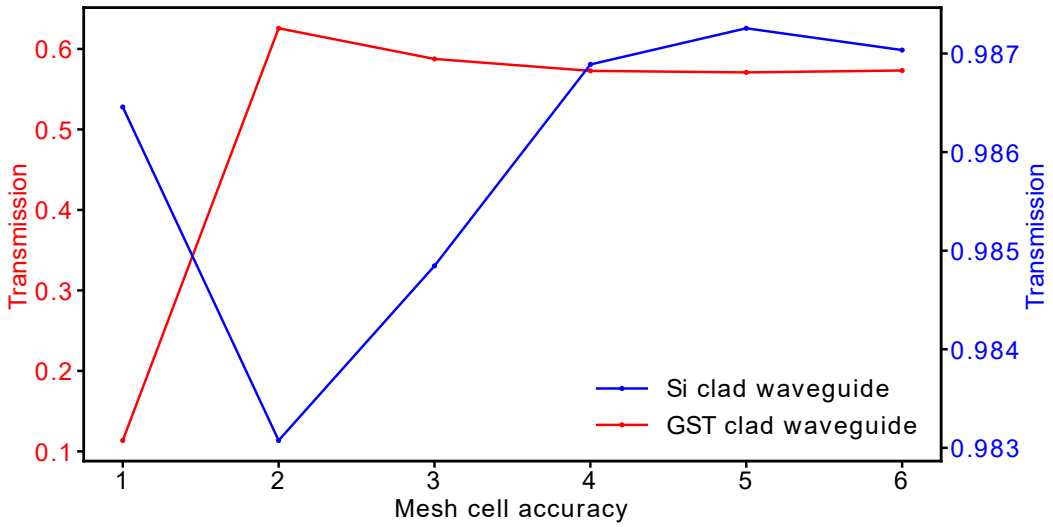

Figure 3.4: Transmission of a 10 μm long SOI rib waveguide for different mesh accuracy settings for unclad, and 25 nm clad amorphous GST.

3.2.3 Propagation losses

With a working model established and an accurate mesh setting found, the same model was run with varying thicknesses of PCM claddings to study the effects of film thickness on transmission. In all cases, the mesh accuracy setting was kept at four and the waveguide geometry unchanged, except for the increasing capping layer thicknesses. As mentioned this will change the meshing geometries to account for the moving interfaces, however whilst an individual result may be subject to some noise because of this, the overall trends are insensitive to this noise. Since the phase change materials of interest are not included in the standard library of materials (whereas silicon and silicon dioxide are) they were added manually using 3D sampled datasets. The exact data sets used were measured using ellipsometry and can be found in chapter 6 (Material Study). Lumerical then fits a polynomial function to both real and imaginary parts, which it can use for arbitrary discrete wavelength simulations. It is worth noting that the automatic fitting function does not always work well for c-band wavelength simulations as it attempts to fit the entire wavelength range with the default number of parameters (6), and using the sum of mean squared errors (MSE) for real and imaginary parts.

This means that for a model fitted over the whole wavelength range, there will be localized errors over a small range due to the polynomial changing more slowly than the real values of n and k. This error is small in absolute terms, however if the imaginary part is close to 0 over the wavelength range, it makes little attempt to fit this part well as the contribution to the overall MSE is often much smaller as compared with the real part. For materials with no losses, a small error from 0 can introduce a lot of incorrect absorption into a mode. For the low loss chalcogenides used in this work, the wavelength range fitted was reduced to 1500 nm to 1600 nm, and the number of coefficients increased to 10. Finally, the weighting of the MSE of the imaginary part was amplified by 100 to ensure it is fitted to the same relative accuracy as the real part. (Figure 3.5)

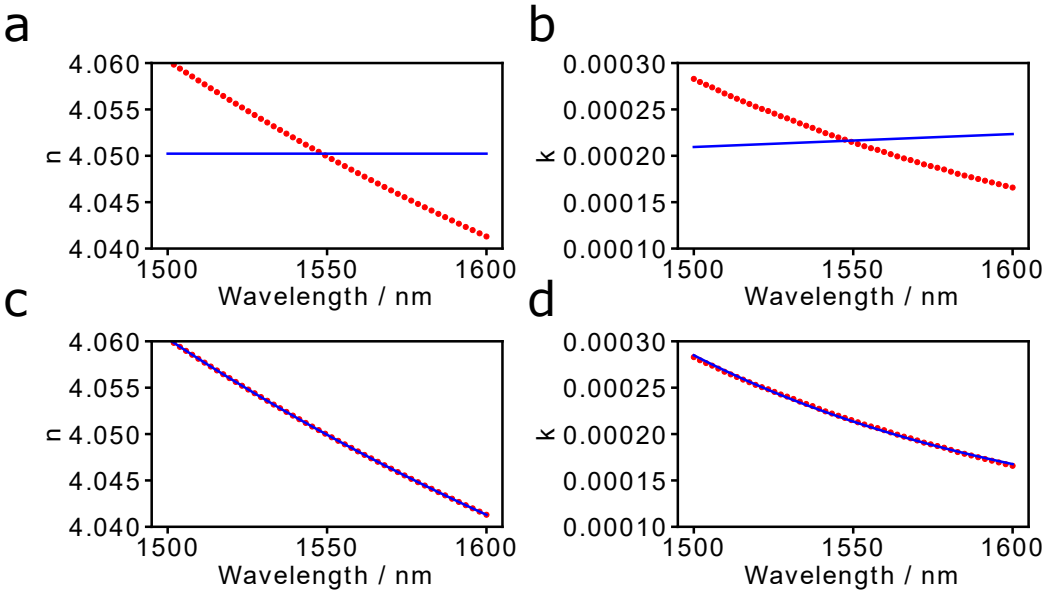

Figure 3.5: The material fits for the refractive index of Sb_2Se_3. Blue lines are Lumerical fits, red data is the measured material values. (a-b) The automatic fit for the real and imaginary parts of refractive index. (c-d) The best fit for user defined parameters for the real and imaginary parts of refractive index.

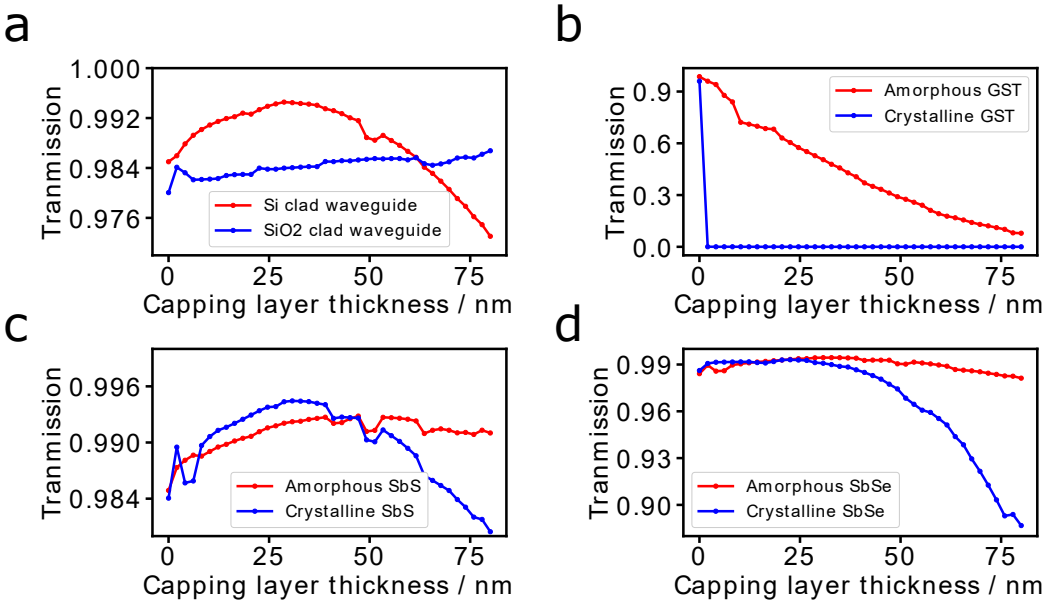

Figure 3.6: The transmission of a 10 μm long planar waveguide for different thickness of cladding layers normalized to the insertion power, using the 3D FDTD solver. (a) Silicon and silicon dioxide, (b) GST, (c) Sb_2S_3, (d) and Sb_2Se_3.

Figure 3.6a shows the transmission for a waveguide with both a conventional SiO_2 cladding, as well as if it were capped with additional silicon. Since the deposition would be on both the rib, and to the sides, this would have the effect of increasing the height of the waveguide whilst leaving the rib height unchanged. This provides a comparison for the "ideal" phase change material, which would be perfectly index matched to silicon in one phase. A further extension to this work would be to etch the silicon back further than the desired thickness in areas where a PCM would be deposited, then use the PCM to backfill the waveguide to the correct height, creating a PCM guiding section to enhance the mode overlap. This has not been considered due to the added complexity of this fabrication.

Increasing the SiO_2 cladding from 0 to 80 nm resulted in a slight increase in transmission from 98% to 98.5% as expected as the SiO_2 acts to index match the silicon with the air above whilst still maintaining a mode guided entirely in the silicon, reducing any losses from modal dispersion. In a true

single-mode waveguide these losses would not exist, however there is always a small component of the light propagating in modes besides the fundamental TE mode. For an increased thickness of silicon, a small transmission increase of 1% is seen for the first 30 nm of silicon deposited as there is a greater separation between the lossy surface and the mode power. After that, increasing the thickness reduces the transmission as the waveguide starts to support multiple modes, reducing the transmission in the fundamental mode.

In the case of GST, seen in Figure 3.6b, both phases show huge losses, with the transmission dropping from the initial 98% to 8% over the 80 nm of amorphous GST thickness. For the crystalline GST, the transmission drops immediately to $4e^{-2}$% with even 1 nm of cladding and continues to decline from there. It is for this reason that GST is limited in its use to phase sensitive applications where amplitude losses are not a consideration, or in applications where a very small volume can be used such as for nano-antennas.

Sb_2S_3 (Figure 3.6c) has a lower index than silicon in the amorphous phase, and a very similar index to that of silicon when in the crystalline phase. As such it performs very similarly to the silica/silicon claddings respectively seen in 3.6a, with the crystalline phase (n = 3.308) an almost perfect match to the silicon cladding. The amorphous phase has the same shape, although the transmission remains high for increasing thickness as due to its lower index of 2.712 it works well as a cladding layer, similar to the silica capping but less strongly guiding due to the lower index contrast. Amorphous Sb_2Se_3 (Figure 3.6d) has almost identical properties to crystalline Sb_2S_3 or silicon, so again the same response is seen. However in the crystalline phase, a drop in transmission is seen for films thicker than 25 nm compared to the amorphous film. As film thickness increases this loss increases exponentially. From this a film thickness of 25 nm was chosen as the best trade off between effective index and loss.

In reality, the largest cause of loss inside silicon planar waveguides is surface roughness caused by the etch, or fabrication tolerances. Neither the roughness or any tolerances are accounted for in these models as including surface roughness drastically increases the meshing density needed for an accurate result, however for well-designed and fabricated waveguides the losses from these imperfections are often far smaller than the losses introduced by

integrated devices such as MMI's. For larger circuits the propagation losses can play a significant role, but other waveguide designs or platforms such as silicon nitride are able to reduce the losses to 0.01 dB/cm and below.

negligible in comparison to the losses from integrated devices. Similarly, the crystalline material models are for a homogeneous material with the same n and k as the bulk crystalline samples. This is not a physical model and excludes any losses introduced by the crystal boundaries such as scattering losses, however a more accurate model of these mechanisms is beyond the scope of this work. For large PCM volumes, the total propagation loss of a device could be measured experimentally and compared with the homogeneous material models to validate the assumption that the simulated material is representative.

3.3 Grating couplers

To couple light in and out of planar photonic waveguides there are two popular techniques. The first is end coupling, where the edge of a photonic chip is polished, and light injected directly into the waveguide, using either a tapered waveguide to better match the mode size inside an optical fibre or using an objective to focus the light from a fibre down to the dimensions of the waveguide. Edge coupling typically provides the lowest insertion losses, however it requires more precise alignment (and therefor stability) as compared to grating coupling. In this work grating couplers were used for all devices due to the ease of fabrication (they can be written in the same photolithographic step as the waveguides) but also as there was a working design within the research group that was compatible with our fabrication limitations.

A grating coupler is an interference device, which works using an effective index array in the same plane as the waveguide to create constructive interference of the incoming light with the same wave-vector as the waveguide. Due to reciprocity they also function to couple light out of a waveguide back into a fibre. A grating width of 10 μm was used, and a 200 μm long adiabatic taper used to couple light between the grating and the 500 nm wide waveguide. The grating had a pitch of 670 nm, with a duty cycle of

0.5. For simulating this grating, the fibre was incident upon it at an angle of 8° to reduce back reflections and couple all the light directionally into the waveguide, and not split between two directions as shown in figure 3.7.

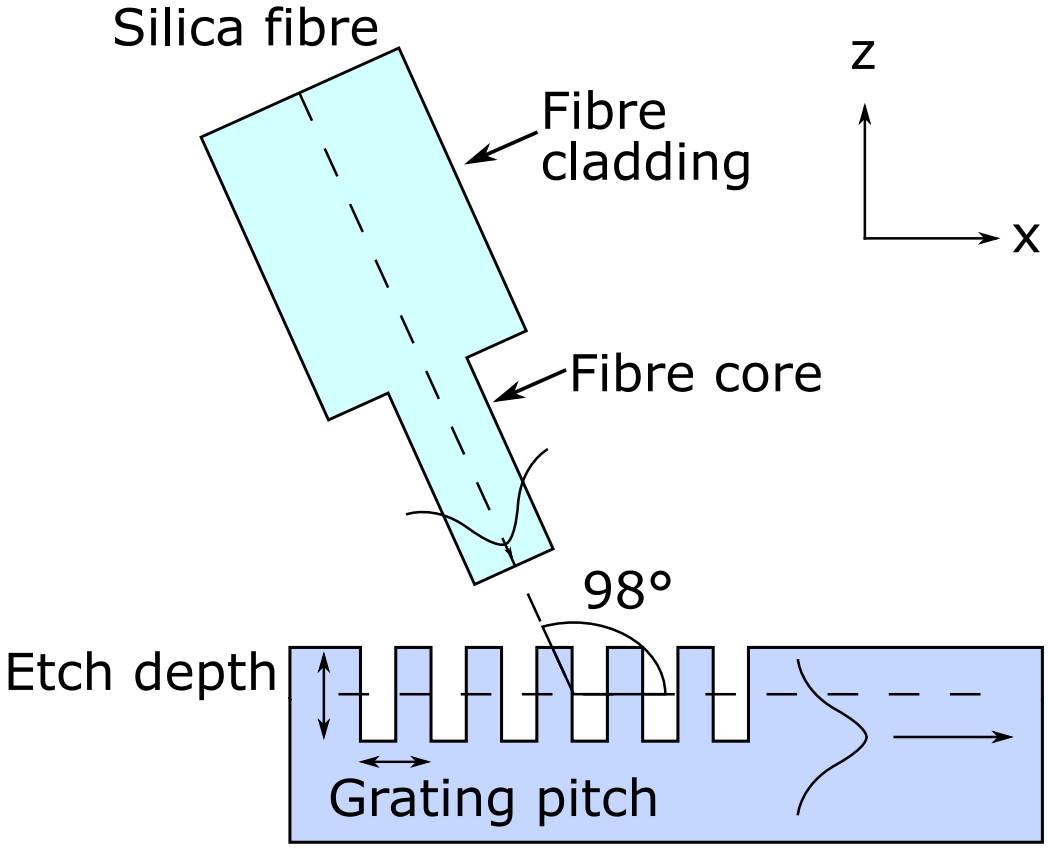

Figure 3.7: Schematic showing the arrangement of a silica fibre being incident upon a grating coupler.

This has been simulated in 2D (as the coupling can be assumed to be invariant with width), and the wavelength response shown in figure 3.8. Whilst not exactly centered around 1550 nm, the performance was very good, with 50% efficieny at the central wavelength, so no changes where made to this tested design to reduce the risk of failure, as a poorly performing grating design will adversely effect every device on the wafer.

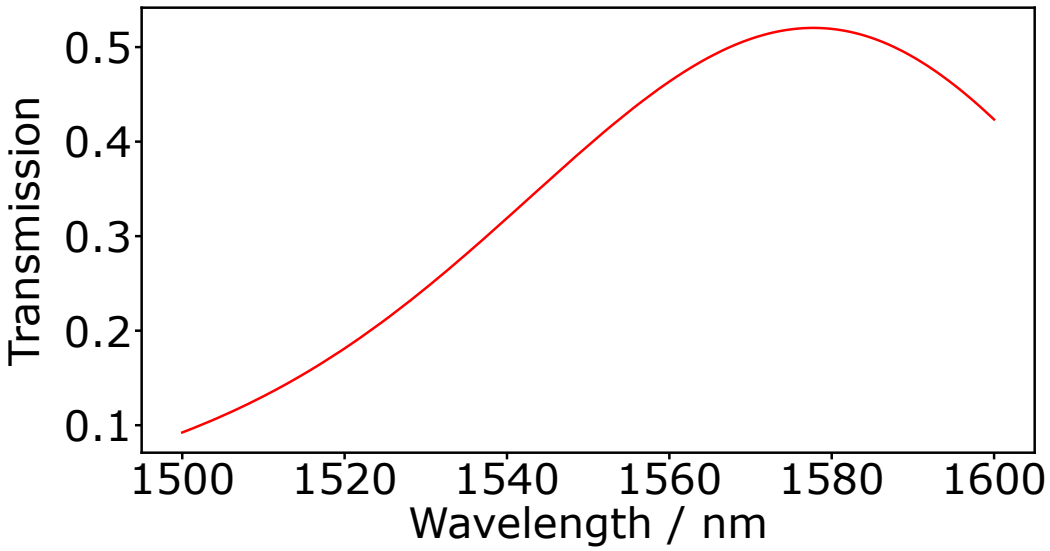

Figure 3.8: The coupling between a silica fibre and a simulated grating against wavelength from 1500 to 1600 nm, showing a maximum coupling efficiency of 50% at 1578 nm.

3.4 Multimodal interference regions

MMI devices were modeled in the same way as the straight waveguides, with a 2.5D simulation used to optimize the parameters or conduct sweeps, and a full 3D simulation only ran to confirm the accuracy of the 2.5D results. The input and output waveguides were modeled to be the same as in section 3.2, a 220 nm SOI waveguide with a width of 500 nm. This width was used as it only supports the fundamental TE mode, and had been previously used by the group to successfully fabricate waveguides. An adiabatic taper from the 500 nm up to a 1000 nm width was used to connect the waveguides to the MMI region to increase the coupling efficiency between the waveguide and MMI. The MMI region itself is similar to the waveguides, but with an increased width to allow for multimodal interference. As shown in equation 2.21, the length or width can be varied, but a self-imaging point will always be present in an infinitely long device, it is simply a case of optimizing one or both dimensions to ensure your output tapers are placed at a position of

high mode purity to ensure strong coupling.

3.4.1 Mesh accuracy

To wavefront shape within an MMI an accurate model of the response of an MMI to perturbations was needed. Initially an MMI with a single input and two output waveguides was chosen as the starting point. The dimensions of the MMI were predicted from theory, using the effective index of the material stack and equations previously described. For a 1×2 MMI it was predicted from MMI theory that arbitrarily fixing the width to 6 μm resulted in an MMI length of 33.8 μm for optimized coupling.

A convergence test was carried out, with the simulation run at each mesh setting from 1 to 6 as with the straight waveguides. A similar trend to the planar waveguides was seen (figure 3.9). The coarse setting showed a lower transmission of 41.5% in both outputs, which converged to 46.5%. Due to the changing cross section of the tapers in the propagation direction, the automatic meshing has a high density, even at low settings so as to accurately model the surface. By replacing the tapers with fixed width waveguide of either 500 nm or 1 μm it is possible to reduce the meshing density, and therefore simulation time. For the same computer resources the simulations could then be run at a higher setting, however it was seen that the tapers are important to maintaining a high transmission as they adiabatically taper the mode size in the MMI down to the size of the waveguides and could not be neglected. To include the tapers, but reduce the run time to a point where parameter sweeps could be run, a mesh setting of 2 was chosen. It is noted that the results from this setting are likely to be 1% higher on average as compared to a higher mesh setting, however this was a small price to pay for the reduced running time. A 1% error is also well below any experimental errors, where grating coupling errors and mechanical drift can have a magnitude of up to 1 dB.

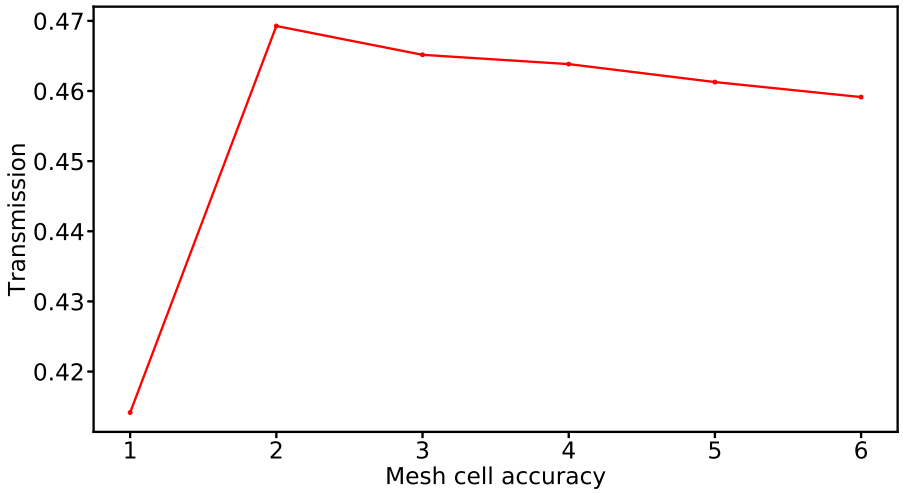

Figure 3.9: The transmission of each output of an unperturbed 1 × 2 MMI against the mesh cell accuracy.

3.4.2 MMI dimensions

A dimension sweep was run with a 1 × 2 MMI, where the width and length of the device were varied to identify the highest performing dimensions. The width was varied from 5 to 7 μm, and the length from 30 to 38 μm. The total transmission (i.e. the sum of both outputs) can be seen in figure 3.10. As predicted from theory (see equation 2.26) the transmission was more sensitive to a width change than a length change, due to the squared dependence of the self-imaging length on MMI width and the linear dependence on MMI length. A band of almost unity transmission was seen, showing that for any given width there was a suitable length, and the predicted dimensions of 6 μm × 33.8 μm were in the center of this high transmission region. Since the MMIs were to be capped with different PCMs, each with their own effective index it was important to choose a device that would perform well across the range of materials that were to be tested. Given that all the capping layers would increase the effective index, a device size of 6 μ m × 33 μm was chosen to be the standard MMI size used in the rest of this work. An MMI of this size would function as a 47% splitter when uncapped or capped with SiO_2,

and closer to a 49% splitter when capped with a thin layer of either Sb_2S_3 or Sb_2Se_3. GST was not considered here as an MMI clad with even 1 nm would reduce the transmission by more than an order of magnitude, making it useless for a low loss router.

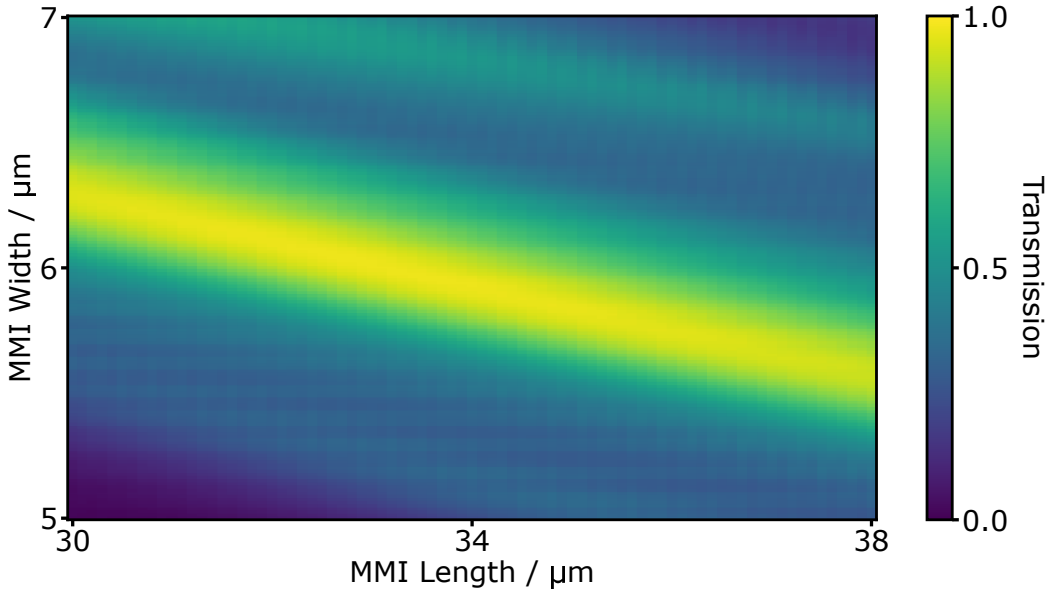

Figure 3.10: Total transmission of a 1 × 2 MMI as a function of varying device length and width.

3.4.3 Phase change capping layers

The MMI was then modeled with varying thicknesses of capping materials (figure 3.11) to show the effect of different materials on the transmission. Again as expected, an SiO_2 layer gave little change with increasing thickness (3.11a), while a slight increase in transmission was seen with a 50 nm silicon layer. As the MMI is designed for high index material claddings, the increase in effective index from additional silicon thickness moves the self-imaging points closer to the output tapers, increasing the transmission. As with the straight waveguides, the GST cladding shows a huge transmission loss for even very thin films in both phases, with the crystalline phase being the most lossy. (3.11b) There is no thickness of material where the losses are

acceptable for wavefront shaping, so from this point on, GST was discounted as a suitable material, and my efforts focused on Sb_2S_3 and Sb_2Se_3. The Sb_2S_3 and Sb_2Se_3 behave similarly, with the amorphous phases acting similarly to SiO_2 as their index is lower than that of silicon (Figures 3.11c-d). For the crystalline phases, the response is similar to the amorphous phase for films thinner than 25 nm. Above 25 nm of thickness, the transmission starts decreasing. For the Sb_2Se_3, this drop is faster with only 30% transmission in each arm for 70 nm thickness, due to the index being significantly higher than that of silicon (n = 4.05 compared with 3.48 for silicon), so for the same thickness, the effective index increase is larger.

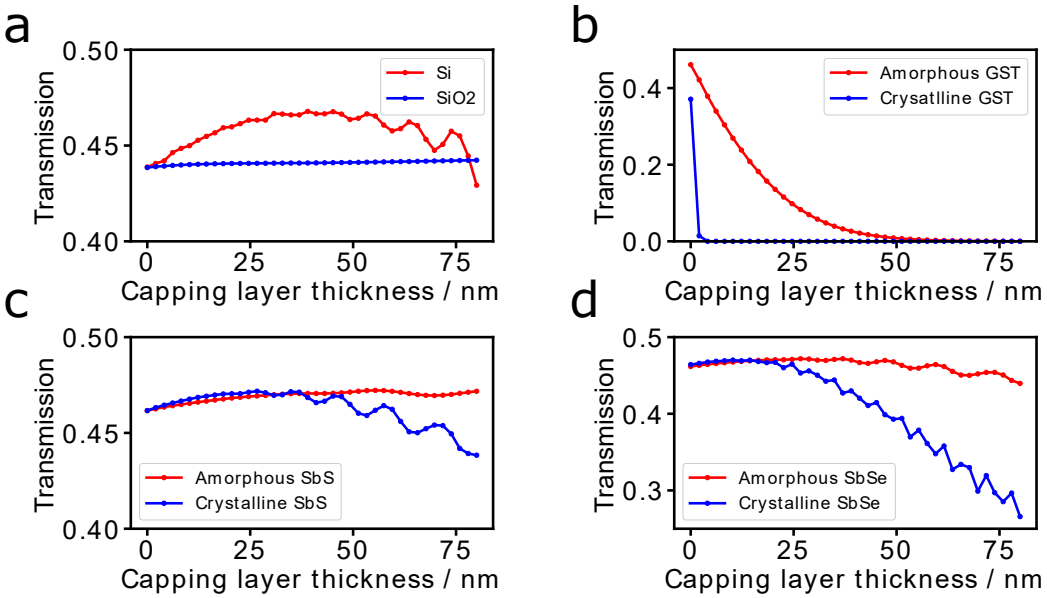

Figure 3.11: The transmission of a balanced MMI for different thickness of capping layers, (a) silicon and silicon dioxide, (b) GST, (c) Sb_2S_3, (d) and Sb_2Se_3.

Beyond 50 nm thickness of Si, an oscillation in the transmission is seen. This was repeated for the other high index claddings (crystalline Sb_2S_3 and Sb_2Se_3). From theory, there are local minimums in transmission with increasing device length. As the thickness of a capping layer is increased, the effective length of the device can be considered as increasing. As the effective length is swept over the local maxima and minima (Figure 3.10) the trans-

mission would be modulated accordingly. To confirm this, the simulation was run again, but instead of varying a film thickness, the index of the MMI region was directly increased from n = 3.45 (the index of silicon) to 3.85, to show the oscillation is a result of the effective index variation and not an interference effect (Figure 3.12). The same oscillation was seen, confirming it is the movement of the self-imaging point that effects the transmission and not an interference effect from the thin film claddings.

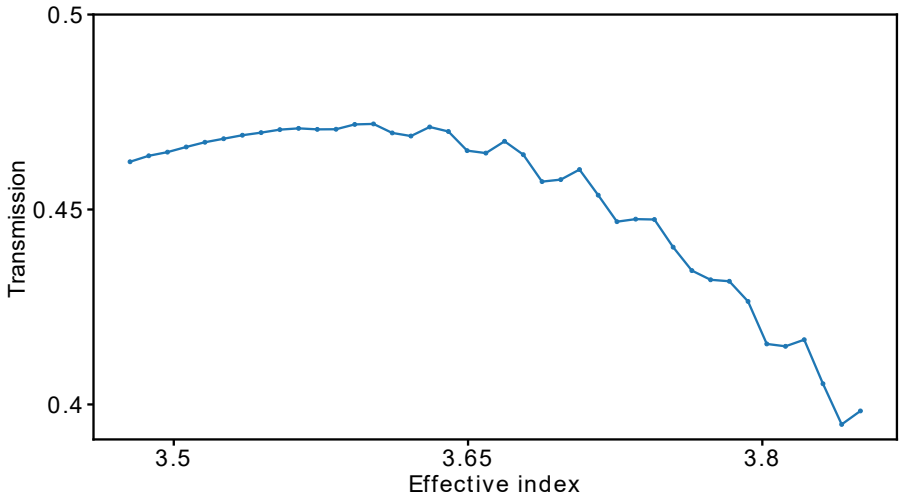

Figure 3.12: The transmission of a balanced MMI for varying index of the MMI region

Finally a full 3D model must be run to confirm that the 2D effective index models are representative. The same device was modeled using FDTD solutions, with a full 3D mesh solver. As discussed, this increases the run time significantly, in this case from a few minutes to 16 hours per simulation. An MMI with a 25 nm thick Sb_2Se_3 capping was chosen, as the material at this thickness had the largest Δn without significantly increased losses. The 2D effective index simulations gave a transmission of 46.5% in each output for this structure, and the full 3D model agreed very closely with a transmission of 45.3%, with the difference most likely due to a small amount of out of plane scattering that the 2D model does not account for. Figure 3.13 shows a slice of the electric field through the center of the MMI. The length of MMIs

which would result in strong coupling for three or more outputs are clearly visible, and the output tapers overlap with the two nodes as expected.

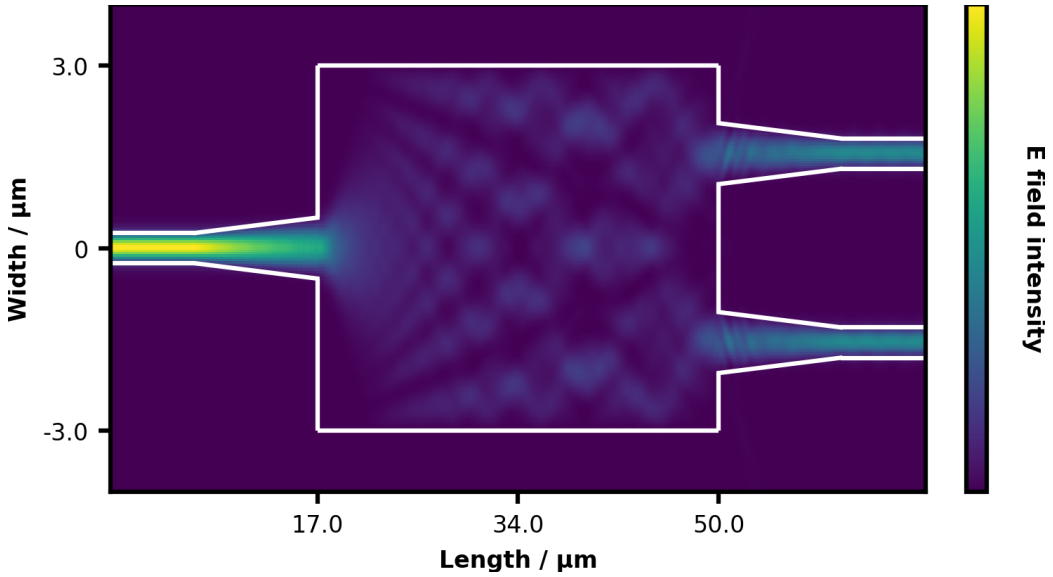

Figure 3.13: The intensity of the electric field within an MMI device, normalized to 1

Chapter 4

Perturbation Modeling

4.1 Perturbation modeling

4.1.1 Optical routing within a 1 × 2 MMI

Having established working models for an unperturbed MMI, the next step was to investigate the feasibility of optical routing using a perturbation pattern. There are some existing demonstrations of this technique [193–195] however they all reply on a permanent or ultra fast index perturbation within the MMI structure, neither being suitable for the majority of applications. Firstly, the feasibility of PCM perturbations needs to be tested, before moving onto optimizing patterns using the available parameter space.

There are several assumptions and restrictions that need to be incorporated into the simulations to enable phase change perturbations to be modeled. Firstly, the experimental constraints must be considered. The proposed technique of using a laser to crystallize or amorphize pixels into a film comes with two important limitations: the pixels that can be written this way are limited in both shape and size by the beam. The spot size of a focused laser is limited by the Abbe diffraction limit, whereby the minimum spot size achievable for a given wavelength is $\frac{\lambda}{2NA}$ where NA is the numerical aperture of the focusing objective. For a wavelength of 633 nm and an NA of one, a minimum spot size of 320 nm is seen. This places a lower limit on the pixel perturbation size, however it should be noted that the phase change area is not solely a function of the laser spot size but of the laser power as well as the thermal conductivity and glass transition temperature of the PCM and substrate. For now I will assume a reversible phase change area of 750 nm, an easily achievable experimental spot size using an NA of

0.5 that is available with long distance objectives.

The second limitation is the perturbation shape. Whilst it is possible to create non-Gaussian beams, they require additional beam shaping as diode lasers (the most common type of laser for this application) naturally emit a Gaussian beam profile. A Gaussian spot would result in a cylindrical phase change volume, assuming the film is thin compared to the Rayleigh length of the laser. However, modeling a cylindrical perturbation in an otherwise Cartesian structure presents a significant challenge, as the simulation creates a mesh over the entire region, where each surface interface should be along the boundary of two mesh cells. To do this with a reasonable degree of accuracy for a cylinder would require a very fine mesh in the perturbation regions, increasing the simulation run time. Whilst it would be possible to model the perturbations with a local polar mesh, the rectangular MMI body would then cause the same issues. I decided to model the perturbations as cuboid to approximate the cylinders, as the effective index change would be similar in both cases. The straight faces of the perturbation cuboids might cause the light propagating in the MMI to behave differently as compared with the cylindrical face, with the back reflections towards the source being increased. However, since the perturbations are only in the PCM above the MMI it was hoped that this difference in reflections would be minimized as the incoming mode would experience the effective index as opposed to the local index boundaries.

Following the results of the PCM thickness modeling, 25 nm of Sb_2Se_3 was chosen as the thickness and PCM of choice for the MMIs. This combination offered the greatest Δn, without compromising the losses of the device. The initial phase of the Sb_2Se_3 in all cases was set to be crystalline as amorphizing a spot into a crystalline film produces a clearer pixel, with only a single phase change area. Recrystallizing this single spot is also simple as the crystalline boundary on all sides of the spot provides many nucleation sites for crystal growth. If instead an amorphous film was chosen, then when a crystallizing pulse is used, a single spot is still formed, however re-amorphizing this spot to create a homogeneous amorphous film is very challenging. Any amorphizing pulse will produce a temperature higher than the crystallization threshold, so depending on the thermal conductivity of the film and substrate, it is possible that this thermal energy will diffuse into the surrounding areas sufficiently slowly as to crystallize a ring around the central amorphization, prevent a

full recovery of the initial phase. If care is taken with the exact pulse powers and positioning this is avoidable, enabling an amorphous background to be used, however using a crystalline background avoids this complication in this work.

Perturbation mapping

To verify that the refractive index shift of phase change within the crystalline film of Sb_2Se_3 is sufficient to affect the propagating modes, a perturbation map simulation was run. This consists of mapping a single perturbation of size 0.75 μm^2 (and the full depth of the Sb_2Se_3) through each position above the MMI, and recording the transmission in both outputs as a function of pixel position. This perturbation map shows the effect of a single perturbation in any location, with a positive $\Delta T/T$ (change in transmission at chose output due to a perturbation divided by initial transmission) showing a positive change to the transmission in the selected output. The stronger the $\Delta T/T$ signal, the larger the effect of the single pixel. As can be seen in figure 4.1, the effect of a single pixel was not larger than 5% for the most effective pixels, however with the number of available pixel positions it may be possible to achieve a pattern capable of guiding the light to a single output with a high extinction ratio. It is likely that due to the effective index shift being small, perturbations towards the end of the device are unable to significantly perturb the light away from an output, explaining the lower $\Delta T/T$ values in this region. The central region shows the largest (both positive and negative) perturbation response, due to the large area of electric field intensity combined with a sufficient propagation distance, to maximize the effect of a perturbation.

For all of this modeling work, only complete phase change was considered on a pixel by pixel basis, as while partial phase change is experimentally possible, the parameter space is already so large as to create significant challenges for optimization without an analytical solution. Using a 750nm perturbation, for a 33×6 μm MMI area there are 352 possible discrete pixel positions. It would also be possible to write an infinite number of different pixels if some overlap between pixels were used to reduce the effective size of a perturbation, but similar to partial phase change, this was not explored due to

computational restrictions. Optimizing a pattern for the highest extinction ratio between the two outputs is not trivial, as even with the simplifications made there are still 2^{352} possible perturbation patterns for pixel sizes of 0.75 μm^2. There are other options to explore for such a large parameter space, such as using a neural network as shown by Dinsdale *et al.* [196].

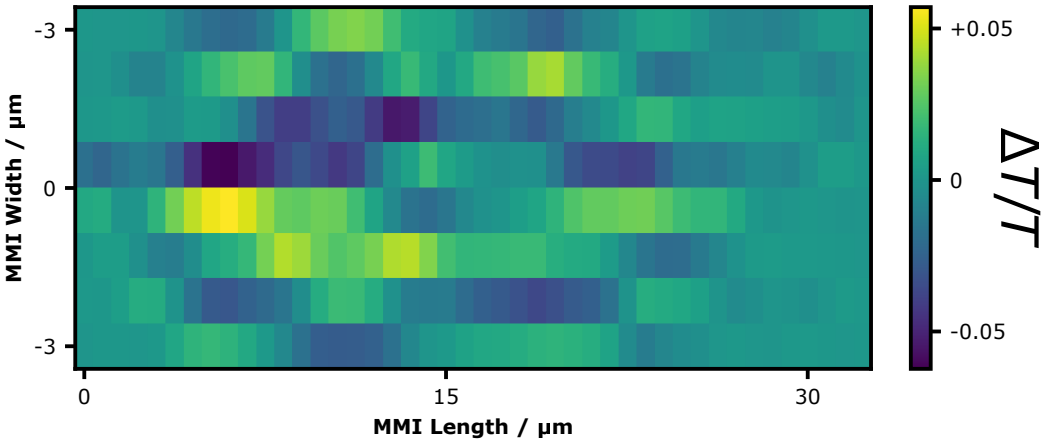

Figure 4.1: Perturbation mapping for a 1 × 2 MMI with a 25 nm thick Sb_2Se_3 cladding.

Random perturbation optimization

To approach a solution for the best pixel pattern for a single output, two methods were trialled. Firstly, a random approach was used before moving to a linear optimization approach. There are other types of optimization that may be suitable for this problem, such as a trained neural network or using the perturbation mapping for each simulation, however these are more involved and proved to be unnecessary for the relatively simple case of a single optimization target. The important characteristics for a device of this nature are the excess loss, i.e. how much the pattern increases the total optical losses within the system, and the extinction ratio, the ratio of power between the two outputs. These are not the only considerations for a full device where cost, footprint, power consumption and switching speed must also be balanced however, for this first exploration only the excess loss and extinction ratio were used to evaluate the different patterns.

Initially, a randomized optimization approach was used due to the simple implementation. A series of simulations were run where a pixel position was chosen at random from the design area, and the phase of this position switched. If a transmission increase was seen in the desired output, then this change was incorporated into the next simulation, and another position trialled. However, if the perturbation decreased the desired transmission then the phase was reset and another position tested. In this way, it was hoped that the simulation would converge on a solution with a good transmission in a single output port. Ideally the extinction ratio would be used as the figure of merit, however transmission in the desired output was used initially for optimization, to avoid the simulation converging on a solution with very low total transmission across both ports but a high extinction ratio. The excess loss should first be limited before the extinction ratio is optimized although it was noted that these went hand in hand in many cases.

The simulation was run for 1054 iterations (equal to testing each position three times on average) with the transmission optimized for the top output. The number of generations (testing each position on the MMI once) is arbitrary, however if too few were chosen, then the simulation would not converge to a solution, whilst continuing to test after convergence was a waste of computational time. Figure 4.2a shows the final pattern and electric field of the MMI after the complete optimization, with amorphous pixels highlighted with white patches. The electric field is mostly unchanged in the first half of the MMI, with few pixels placed here and the electric field bearing a strong resemblance to the field within an unperturbed MMI. However, at the output side, it is obvious that the top taper contains a greater fraction of the electric field, and therefore power as compared with the bottom taper. The extinction ratio between the two ports is a good figure of merit for a router, although does not encompass all important elements, such as total transmission. For this reason, the total transmission in conjunction with the extinction ratio was used to discuss the relative performance of the different approaches. As can be seen in figure 4.2b, this pattern creates a routing effect with the top output transmission increases quickly to a splitting ratio of 70%:21%, with the remaining 9% of the light being lost to the surroundings. After 200 simulations the simulation reaches a local maximum and cannot improve further. Whilst this is a positive result and shows proof of concept, the extinction ratio is poor and the additional losses are higher than expected, although still far superior to other competing phase change routers.

It is likely that a random optimization will never progress to a highly efficient solution due to the directionality of the device. A set of pixels initially placed that showed an improvement may be detrimental to the final pattern, as when future pixels are added closer to the input side, the electric field at the initial set of pixels has changed, changing their effect. However as the simulation can only test a single pixel change, if every pixel in the current pattern provides a small benefit then a solution is found where any single pixel change is detrimental to the result, however the overall efficiency is still low.

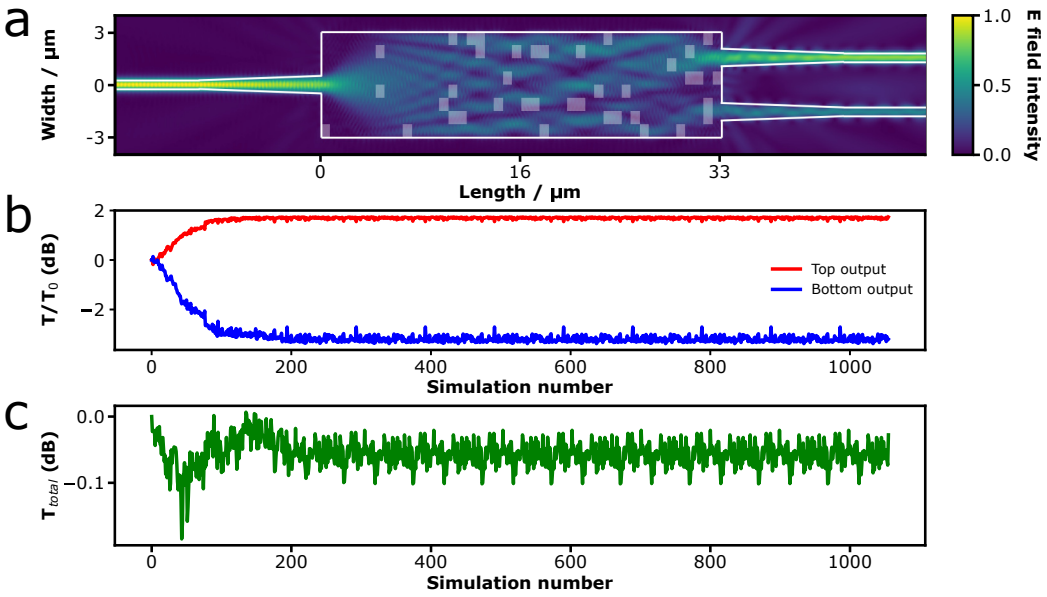

Figure 4.2: (a) Electric field of the MMI with the final randomly optimized pixel pattern, obtained using the 2D approach, with amorphous pixels of 750 nm size shown in white. (b) The extinction ratio (T/T_0 - current transmission divided by initial transmission) between the top (red) and bottom (blue) outputs as a function of simulation number. (c) The total transmission T_{total} of the device at each simulation.

Figure 4.2c shows the additional loss in the device with the final pattern showing only a 0.05 dB increased total loss, as compared with the unperturbed device. This is a promising result as there is likely room for improvement using a more suitable optimizing scheme. It is interesting to note that

at the 160^{th} simulation the additional loss was negligible, whilst the splitting ratio was 70:22, with the final 8% of light being lost in the both the unperturbed and perturbed devices. This suggests that there may be a trade-off between a high total transmission and higher extinction ratio, so depending on the application there will be different solutions for the pixel pattern. However the difference between these two patterns is marginal, and close to the numerical errors of the 2D effective index simulation so this trade-off should be explored separately.

A full 3D simulation was run of the unperturbed device, and with the final pixel pattern to compare with the 2D effective index simulations. This should give a more complete view as it was run at a higher mesh setting and will include out of plane scattering. Whilst the 2D simulations complete in 87 seconds (taking 25 hours for a 1054 simulation optimization), a single 3D simulation is completed in 11 hours, making it impossible for optimization use and instead used only to verify the accuracy of the final result. This 3D simulation of the final pattern produced a splitting ratio of 66:23, similar to the 70:21 obtained for the 2D method, with the difference likely due to out of plane scattering that is not accounted for accurately in the 2D model. This close agreement confirms that the 2D effective index method is suitable for fast pattern optimizations and produces results with a similar degree of accuracy to the full 3D FDTD simulation, but in a fraction of the time. Ideally a full 3D optimization sweep would be run to compare the differences in the patterns found, however this was not feasible given the computer resources available.

It was suspected that in this random approach the pattern is susceptible to local minima's, and that a high performing pattern could be found. Traditionally to avoid a local maxima (as was suspected in this case) a larger perturbation would be introduced into the system. In the context of this simulation it would take the form of switching multiple pixels in a single simulation, in an effort to break out from the current pattern. However, with the size of the parameter space this could increase the total simulation time beyond what was possible. A more intuitive and simple approach is simply to test each pixel position in order from input to output, due to the inherent directionality of the device, to avoid the problem of reducing the effect of a pixel by placing a different pixel closer to the input side of the device.

Linear perturbation optimization

To improve upon the results of the random optimization, a linear approach was tested, whereby every pixel position was tested in order. Starting with the first position in the grid, the phase of the top left-most pixel above the MMI was switched. If the transmission in the desired port increased, then this change was kept, and the next pixel in the column tested. If the transmission decreased or stayed the same, then the phase of this pixel was reset to its initial phase, and the next pixel in the column tested. Once all pixels in a column were tested this way, the simulation would start testing the next column from the top position. (See figure 4.3.) This approach ensures that each pixel placed is done so with the electric field it is likely to experience in the final pattern. It is still susceptible to local maxima's and has the additional drawback of creating the same pattern for each device, given the same parameters. However, during a single optimization pass, if the excess loss is low then in theory the set of solutions generated by this approach contains a pattern for each discrete splitting ratio between the initial and final states.

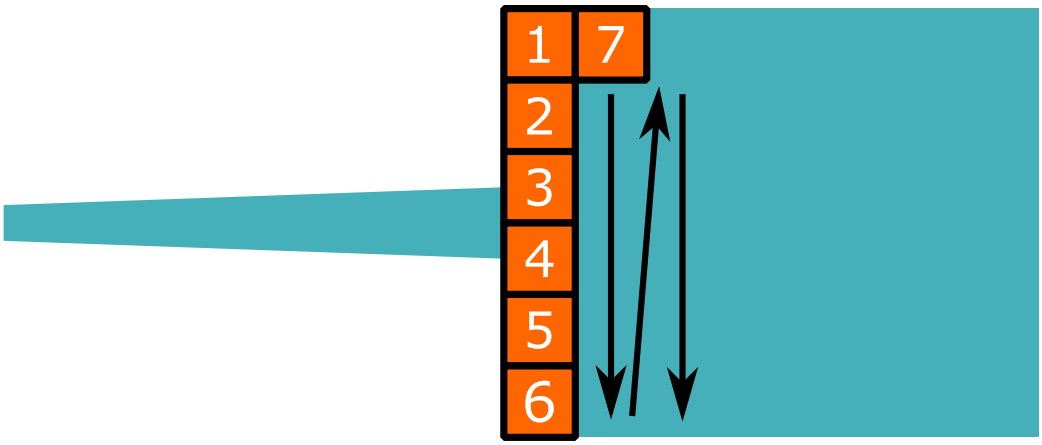

Figure 4.3: Schematic of the pixel writing approach, showing the order in which pixel positions were tested for as $1\mu m^2$ pixel.

This approach yielded an impressive result, with a final splitting ratio of 99:0 between the top and bottom output as can be seen in figure 4.4b. At the largest difference there was a 30 dB extinction ratio between the

two outputs (at simulation 869), approaching or exceeding the performance of other published on-chip switches. If this could be realized it would be a significant achievement for the first demonstration of this approach, and represent the best reconfigurable on-chip routing. Furthermore, the pixel pattern that achieved this result was quite sparse as seen in figure 4.4a, with only 42 pixels being used spread across the whole device, lowering the total switching energy cost as compared to a pattern with many more pixels. The first pass of each position on the device (the first 352 simulations) showed a fast improvement to a result comparable to that achieved by the final pattern, at least in terms of extinction ration. The second and third sweeps of the MMI made few changes to the pattern, and no overall change to the extinction ratio, although there was some benefit to the total transmission.

Interestingly the total transmission was increased significantly during the optimization as compared to the unperturbed device. Initially the device was only about 90% effective at capturing all the input light in both outputs, whereas with the perturbation pattern applied it was able to capture in excess of 99%. Again most of this improvement was shown in the first pass. From this improvement in total transmission it can be concluded that the pixel writing technique could be used to trim prefabricated devices, whereby a poorly fabricated device could be improved with a perturbation pattern. Post-fabrication trimming is of particular interest for large circuits that have few points of failure, where a minimal amount of trimming could provide a large yield improvement. Furthermore this method would be possible post-fabrication for most standard devices in the silicon photonic toolkit, besides MMIs, with the phase change material being sputtered through a mask onto the components in question.

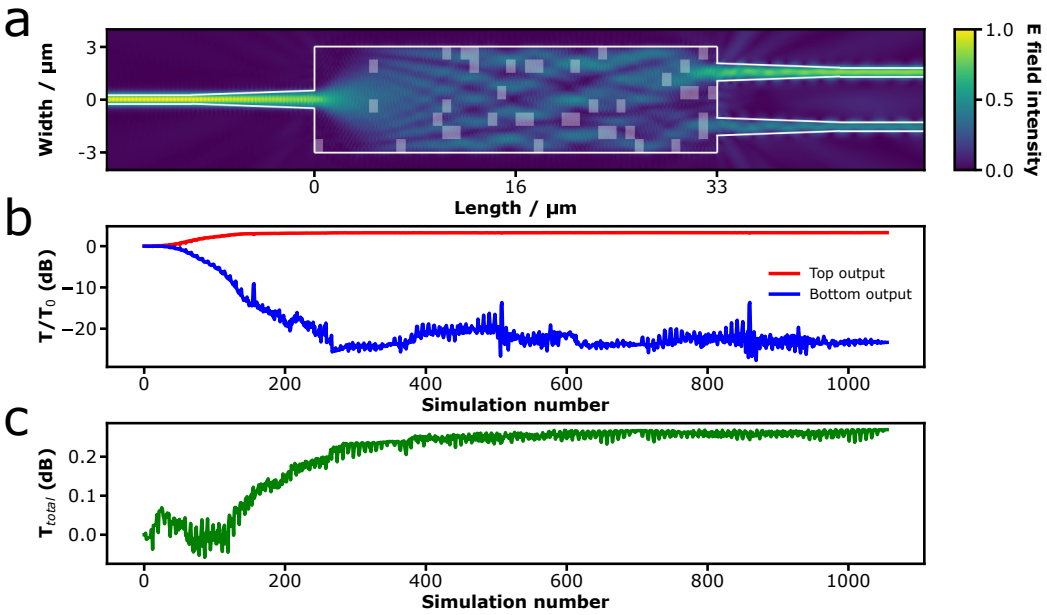

Figure 4.4: (a) Electric field of the MMI with the final lineal optimized pixel pattern, with amorphous pixels of 750 nm size shown in white. (b) The extinction ratio between the top (red) and bottom (blue) outputs as a function of simulation number. (c) The total transmission of the device at each simulation.

4.1.2 Pixel size

The effects of different sized perturbations were investigated, as whilst the final pixel size is limited by experimental factors, it is possible to reduce the spot size (via higher NA objectives or using oil immersion) if there is a significant performance increase. Using a photomask to physically limit the size of each pixel of PCM may be another route to achieving smaller perturbations. Reducing the perturbation size results in a larger parameter space to test, likely increasing the possible extinction ratio. Similarly increasing the perturbation size should have the opposite effect. The linear optimization scheme was used as before, with simulated square perturbations of 500 nm^2, 750 nm^2 and 1000 nm^2. These sizes were chosen as there were all factors of the length and width of the previously used MMI, to ensure complete coverage of the MMI without any perturbation overlap to keep consistency with

the previous models. The MMI dimensions could be changed to accommodate an arbitrary size, or use perturbations that only partially overlap the MMI at the edges if a specific perturbation size was necessary.

Figure 4.5 shows the different final patterns and extinction ratios as a function of simulation number for each pixel size. As before, three complete sweeps of the device were run, resulting in longer simulation times for the smaller pixels. As expected with reduced pixel size, the extinction ratio and total device transmission increased, at the cost of a slower convergence due to the reduced impact of each pixel. The results are summarized in table 4.1, where it can be seen that in all cases there was a significant improvement in total transmission compared to an unperturbed device (initially 90% total transmission), however the smaller perturbations were able to guide almost all light with an impressive 99% total transmission, all in the desired output. The only significant difference between the 750 nm^2 and 500 nm^2 perturbations was seen in the extinction ratio (33 dB compared to 26.5 db), which is more sensitive to very small absolute changes in transmission. The 1000 nm^2 perturbations were still effective at optical routing, with a 22.5 dB extinction ratio, and an improved total transmission. Given the experimental difficulty of producing and detecting smaller phase change pixels, 750nm^2 perturbations were chosen as the preferred perturbation size to balance these challenges with performance.

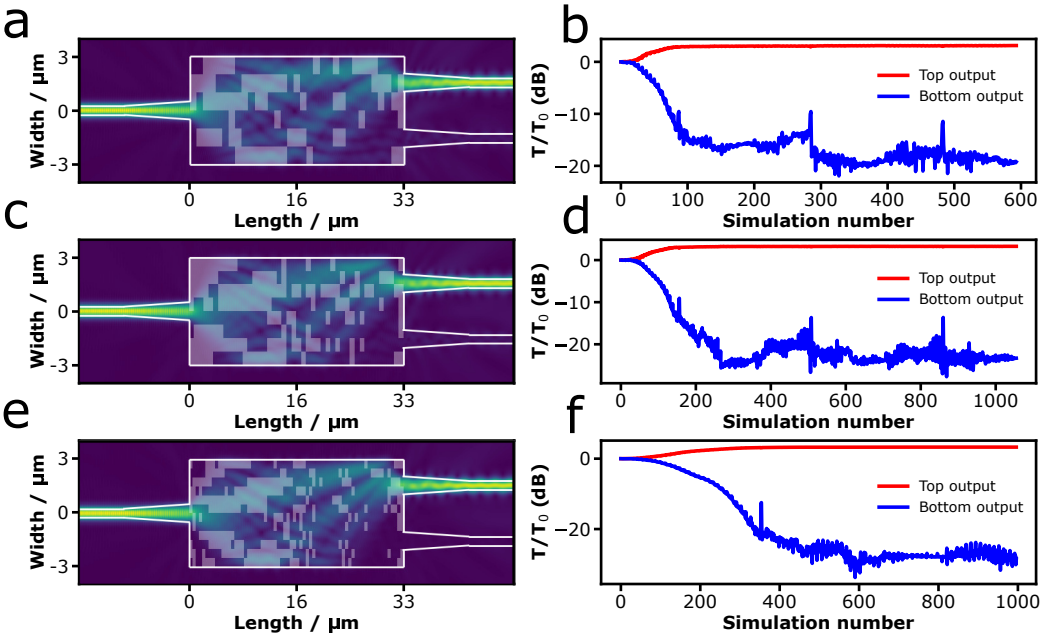

Figure 4.5: The electric field distribution (a,c,e) and extinction ratio (b,d,f) for an MMI with perturbations of size 1000 nm^2 (a,b), 750 nm^2 (c,d) and 500 nm^2 (e,f).

It is interesting to note the similarities in the patterns found for varying pixel sizes. If an infinitely small perturbation could be used, then a continuous pattern would be seen. As the pixel sizes are increased it seems obvious that this continuous pattern becomes pixelated, at the scale of the pixel sizes, creating the similarities seen between the three sizes tested here. In the first half of the device, a branch like structure emerges as the pixel sizes are reduced, supporting this theory of a continuous pattern. When considering the wave like propagation of the light this is an obvious conclusion as if a sufficiently strong perturbation were used, the result would be analogous to an etched waveguide between the input and output.

Table 4.1: The best extinction ratio, total transmission and transmission ratio for an optimization of a 1 × 2 MMI using pixels of size 500 nm, 750 nm and 1000 nm.

Perturbation size (nm)	1000	750	500
Extinction ratio (dB)	22.5	26.5	33.0
Total transmission (%)	97.0	99.0	99.0
Transmission ratio	96.5 : 0.5	99.0 : 0.0	99.0 : 0.0

4.1.3 Reduced pixel count patterns

Reducing the number of pixels in a pattern was briefly tested using a thresholding approach. Patterns formed this way would have consequences for the switching energy cost of the device, where switching many pixels that have negligible effects would be undesirable. Also for experimental testing, a simplified pattern is desired that would reduce the writing time and show the greatest improvement for the least number of pixels. To this end, a pattern was optimized with 1000 nm^2 perturbations, to reduce the pixel count, as well as introducing a threshold value of improvement for a pixel to be accepted. This value was a flat percentage increase in the transmission in the desired port that must be observed for any single pixel change for it to be accepted into the final pattern and serves to remove pixels of limited impact. Moving to the larger pixels and reducing the number of them will have a performance cost, however this trade-off may suit some applications provided the performance loss does not move this technique below other competing routing options.

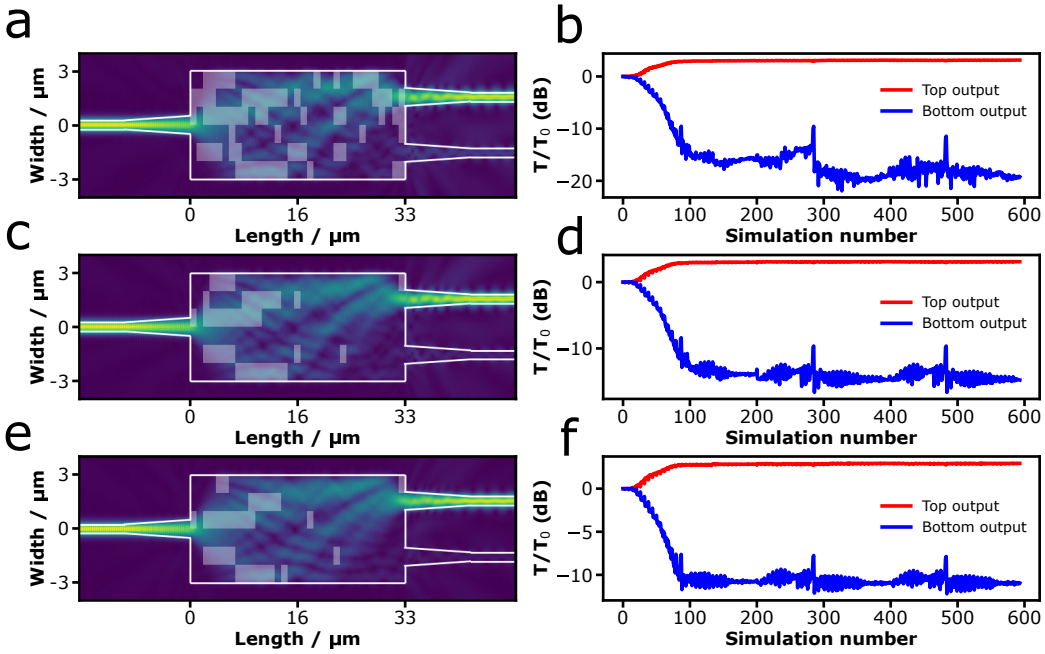

Figure 4.6: The electric field distribution (a,c,e) and extinction ratio (b,d,f) for an MMI with a perturbation size of 1000 nm^2, and a threshold value of 0% (a,b), 0.5% (c,d) and 1% (e,f).

Next we investigate the effect of the threshold value. Three thresholds were chosen to illustrate the trend and provide a framework for future studies. Figure 4.6 shows the patterns and extinction ratios that were optimized for threshold values of 0% (top), 0.5% (middle) and 1% (bottom). In general, a higher threshold had the effect of removing pixels from the same pattern that would be generated with a lower threshold, however there were rare cases where an additional pixel was added, as a result of the changing electric field due to previous pixels being removed. There were very few pixels in the second half of the device when a threshold level was introduced, even if the threshold was low. This was due to the implementation of the threshold as a flat improvement value. Accepting a pixel that improves the transmission by 1% is significantly easier at the start of the device where the initial ratio is 50:50 between both outputs. However, towards the middle of the device where the ratio is already approaching 95:5, finding a pixel that will offer a 1% improvement is almost impossible. The solution to this would be to use a

Table 4.2: The best extinction ratio, total transmission and transmission ratio for an optimization of a 1 × 2 MMI using a transmission increase threshold of 0%, 0.5% and 1%.

Threshold value (%)	0	0.5	1
Extinction ratio (dB)	22.5	17.9	14.1
Total transmission (%)	97.0	95.7	94.7
Transmission ratio	96.5 : 0.5	94.3 : 1.5	91.0 : 3.7

threshold value that scales with the magnitude of unguided light, however this idea could be taken forward in additional work where a reduced pixel count is important. The important result here is that even very sparse patterns were capable of extinction ratios in the region of 10-20 dB.

Finally, to reduce the pixel count it was tested if using a full depth perturbation (120 nm depth to limit the fabrication to the same step as the device etch) would be of interest. This would involve etching the MMI body away (in the same etch that defines the rest of the device), then backfilling the MMI region with the PCM of choice. This fabrication would involve precise alignment between the first etch and PCM deposition, but with modern lithography tools this is possible using alignment markers. In this way, a perturbation of 120 nm depth or more would be possible. The larger volume of the perturbation will lead to a larger effective index change per pixel, potentially reducing the number required. This result is of general interest as a full depth perturbation may provide superior guiding when compared with the cladding perturbations previously discussed, due to the increase in wavefront shaping per pixel.

Figure 4.7 shows the results, which initially look very positive. The perturbation map features very few pixels, with 28 being used in total for a 750 nm^2 (the standard size used in this work) perturbation size. Better than 20 dB extinction ratio was reached in the first pass with the losses look promising as well, with a total gain of 1 dB, however these results are less impressive when compared with the optimized 750 nm^2 partial perturbations. The real part of refractive index of the crystalline Sb_2Se_3 (4 at 1550 nm) is significantly higher than that of the silicon (3.5 at 1550 nm). Changing the effective index of the MMI changes the self-imaging points such that the unperturbed device only shows a splitting ratio of 28:28, with the remaining

44% of the light being scattered outside of the outputs. This might not be a problem as the patterns are capable of correcting for this as previously shown. However, using the full depth perturbation, at least over a single pass, this was not fully corrected for, with a final ratio of 79:0 being found. The reason for this is that with such a large perturbation, the model has far less fine control for wavefront shaping. As can be seen from the total transmission plots, single pixel changes can have a huge effect (>2dB change), and is the cause of the strong oscillations seen between consecutive simulations. Such large changes prevent the model from reaching a high-efficiency solution, as it becomes increasingly hard to introduce a perturbation to correct for a small amount of light that is not guided towards the desired output, without also affecting light that is currently being guided as intended. If one extrapolates to using pixels of very large index, it becomes obvious that there must exist an optimum effective index perturbation that would balance the ability to strongly interact with the light (useful for the initial guiding), with the fine control needed to achieve a very high extinction ratio. This could be achieved with a combination of different perturbation strengths in the same device, possible through varying the size of the perturbations, of the depth of the amorphization, however this has not been explored at this stage. It is worth noting that starting with a device of different dimensions, such that the initial performance is closer to a lossless splitter, may improve upon the results shown here, however the technique will still be the same.

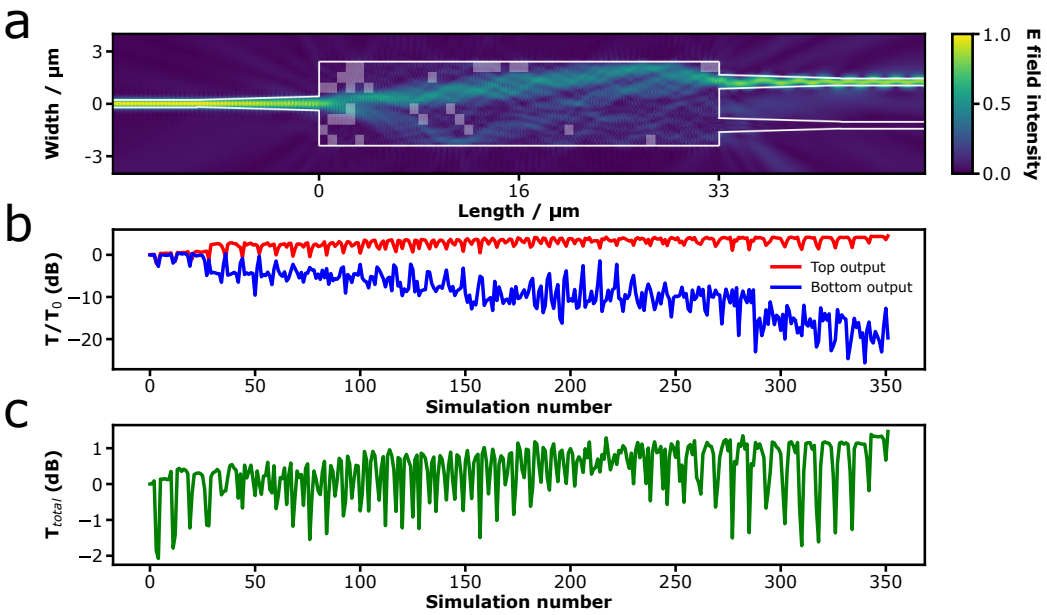

Figure 4.7: (a) The electric field distribution, (b) extinction ratio (c) and total transmission for an MMI with a full depth Sb_2Se_3 perturbation.

4.2 Arbitrary optical routing

Having shown that the technique of using a phase change film above an MMI with a pixel pattern creates a powerful reconfigurable wavefront shaper, and that it was possible to optimize highly efficient patterns using a linear approach, a wide range of devices beyond the 1 × 2 MMIs should be possible. Here I will explore a larger MMI device, with multiple input and output waveguides. This device would be far more useful for optical routing compared to the limited 1 × 2 devices previously presented, although moving beyond optical routers there are likely applications for wavelength or mode (de)multiplexing, mode conversion and polarization dependent planar photonics all based on this approach.

Moving to an MMI with three inputs and outputs, if arbitrary routing can be shown between any input and output combination, then a truly reconfigurable on-chip optical router can be demonstrated. The same 25 nm

thick film of Sb_2Se_3 was again modeled above an SOI MMI. The MMI width needs to be increased to accommodate the extra tapers without causing interference between the different outputs, but as was shown with the 1 $\times$2 MMI devices, there is a large range of design freedom so long as the MMI area provides a large enough parameter space to find an acceptable solution. The MMI dimensions were arbitrarily chosen to be 9 $\times$ 33 μm, however a larger device may improve the possible results due to the increased parameter space that it would provide. Using the same linear technique as before, all the unique port combinations of a 3 $\times$ 3 MMI were optimized. Due to the symmetry of the device, only four optimization sweeps are needed.

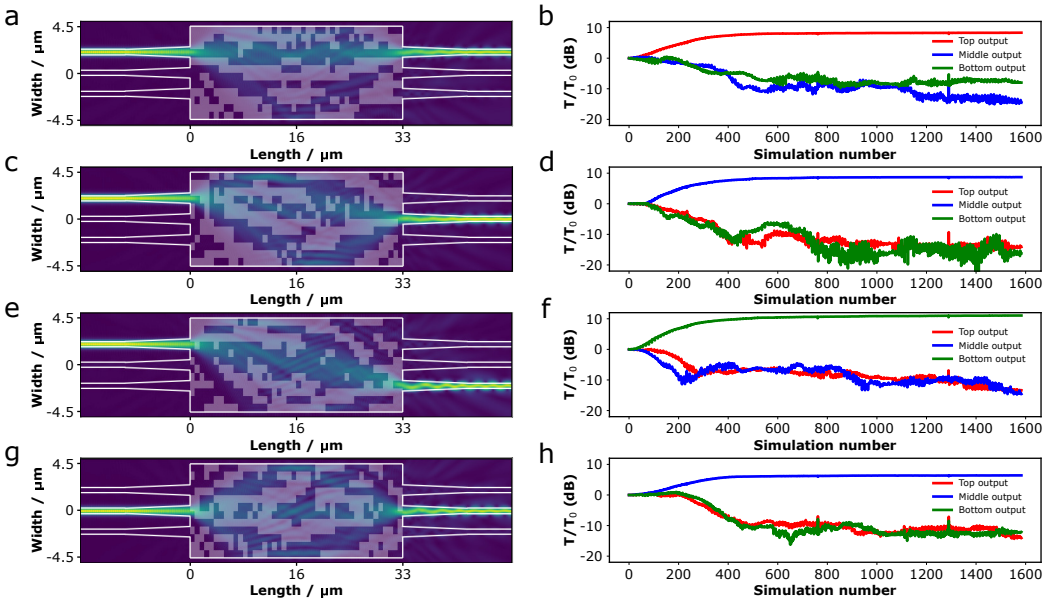

Figure 4.8: The electric field distribution (a,c,e,g) and output transmissions (b,d,f,h) for a perturbed MMI optimized for the four unique port configurations of top-to-top (a,b), top-to-middle (c,d), top-to-bottom (e,f) and middle-to-middle (g,h).

Figure 4.8 shows the results of these optimizations. In all cases, a high extinction ratio was seen between the target port and the additional ports, with a crosstalk of -19 dB or better seen for all port configurations. Unlike the 1 $\times$ 2 MMI optimizations, this device does not function as an efficient splitter when unperturbed, with a total transmission of 34.2% across all

Table 4.3: The transmission in all three ports of a 3 × 3 MMI after optimization for all 4 unique port combinations.

Final output	Top / dB	Middle / dB	Bottom / dB
Top-Top port coupling	-0.254	-23.4	-19.3
Top-Middle port coupling	-22.7	-0.134	-27.6
Top-Bottom port coupling	-21.9	-23.4	-0.286
Middle-Middle port coupling	-21.2	-0.272	-19.2

three outputs for an input in the top port. This shows that this technique can scale to larger port numbers, paving the way towards an arbitrary optical router, as well as confirming the device trimming that was earlier discussed. The individual port transmissions for each pattern can be seen in table 4.3. Coupling from the top input to bottom output showed the highest crosstalk, likely due to the light traversing the longest distance on average.

Chapter 5

Methods

5.1 Cleanroom Fabrication

5.1.1 AJA Orion RF-sputtering

An AJA Orion sputterer was used for all the material depositions due to the versatility and high throughput it offers. The load locked vacuum chamber allows for fast sample changes whilst maintaining a high vacuum in the main chamber, of reduced contamination of the main chamber vacuum. Variable gas flow rates, main chamber pressure and RF power on each of the six guns during the deposition enables the user to explore a large parameter space for the deposition conditions. This proved to be very important for thin-film depositions where the power and pressure affect the film's crystallinity, stoichiometry and optical absorption edge.

The AJA operates by using an RF-induced plasma to bombard a target to create a spray of molecules from the target. It can hold up to 6 unique targets, allowing for co-sputtering of elemental targets to create doped films, or for more complicated multilayer stacks. The targets are mounted with the RF source beneath them, causing vertical sputtering of the target molecules onto a spinning substrate. This combined with large diameter targets gives a good film uniformity across the sample chuck. Another benefit to using sputtering over other deposition techniques is the low substrate temperature, compatible with materials of a low crystallization temperature or temperature sensitive photoresists. The AJA also has the option of plasma etching the surface of a sample, before sputtering to clean it of contaminating particulates or native oxide layers. This was used to improved adhesion between the substrate and sputtered materials, as well as to remove the native silica layer from silicon

substrates.

5.1.2 KLA Tencor Stylus Profiler

A stylus profiler was the quickest way to determine the thickness of a thin film. After each deposition it was used to record the thickness of sputtered material, to monitor the degradation of the target, and the sputtering rate. A ceramic stylus tip is run over a region of interest whilst a constant pressure is maintained, and a force feedback loop reconstructs the surface profile. The tool is calibrated using samples that are certified to an accuracy of ± 1 nm of the quoted thickness. In all cases, a 200 Hz sampling rate was used with a 2mg force applied. This measurement could be used in tandem with a fitted ellipsometry model to verify the integrity of the fitted model. SEM measurements of a cross-section of sputtered films were also used to confirm the film thickness.

5.1.3 Energy dispersive X-ray

Energy dispersive X-ray (EDX or EDS) is a common technique for probing the chemical composition of a sample. An X-ray detector, mounted inside an existing SEM tool, makes use of the X-rays produced by the tightly focused electron beam. When an incoming electron excites a bound electron inside an atom, there is a unique X-ray released as the electron relaxes back to the ground state. As every excitation requires a unique amount of energy, this information is conserved during the X-ray release. Using a standard cobalt target to calibrate the tool, it is possible to identify the composition and stoichiometry of a sample by analyzing these emitted X-rays.

5.1.4 Photolithography

Standard photolithographic processes were used to create both the silicon devices, as well as the windows for PCM sputtering. A light-sensitive photo-induced cross-linking resist is deposited on top of a sample by a resist spinner.

Using a recipe, the thickness of the resist can be precisely controlled via the speed and duration of the spinning. The resist is then exposed to a patterned UV source (usually through a photo-mask), cross-linking the polymer chains in the exposed regions, creating an insoluble surface. A chemical bath can be used to remove the unlinked polymer, creating the desired patterning. Several different photolithographic approaches were used (depending on cost, speed and volume) which are briefly outlined below along with the other fabrication steps.

Sample preparation

A nitrogen gun was used to remove any large particles from samples, before proceeding to wash the sample in acetone, IPA and finally water to remove any polar or non-polar contamination. An ultrasonic bath at 40 kHz was used with each solvent, making use of cavitation forces for thorough cleaning. Finally, the samples were dried on a hot plate at 110°C for 60 seconds.

Photoresist deposition

Centering the sample using a vacuum chuck, a liquid photoresist (SA1813 in this case) would be dropped onto the surface using a syringe to avoid leaving bubbles in the viscous fluid. By spinning the sample at a known speed, a uniform film of a known thickness of photoresist is left behind. A soft bake on a hotplate removes any solvents left in the resist, to improve the adhesion to the substrate, and prevent any photomask contamination in further steps.

Photoresist Exposure

The method used to expose the resist differed between samples, depending on what was most suitable. UV-lithography, laser lithography and E-beam lithography all being used. UV lithography is the most common method, where a UV lamp is used to expose the whole sample, with a partially opaque mask between the UV source and sample (typically a chromium-plated glass sheet). The opaque sections create a pattern of stable and unstable resist,

where the unstable resist can be removed to leave an imprint of the design. This approach has the benefit of being a fast batch process, with exposure times being on the order of a few seconds, and being scalable up to any size of sample. However it requires a custom photomask, which is expensive for small sample numbers and can have a long lead time. It is also not a flexible approach with no allowances for changing the design once a mask is made.

Laser lithography is similar, in that an optical exposure is used to selectively cure the photoresist. However due to the size of the laser spot, it has to be raster scanned over the desired area, which can be slow for larger devices, and becomes impractical for large sample numbers such as an entire wafer. However, by modulating the laser power in real-time, it is possible to create any design by leaving some areas un-exposed, without the need for a photomask. This is a fast and cheap approach for prototyping, however the resolution is limited by the diffraction limit of the laser, which is usually larger than then minimum feature size achievable with a photomask.

Finally, E-beam lithography can be used to achieve critical dimensions that are be impossible to achieve with the other approaches. Similar to the laser lithography, a collimated beam is used to scan over the sample and create the pattern. By using electrons instead of photons, the diffraction limit is greatly reduced, allowing for very small features to be written. Due to the demand for large E-beam patterns, the queue times for E-beam lithography can be long.

Chemical processing

Once a photoresist has been patterned and baked to sure it, a chemical process is needed to remove the soluble resist, leaving the hardened areas. For the resist SA1813, NMP (1-methly-2-pyrrolidone) was used to strip the soluble resist. A simple heated chemical bath is all that is needed, followed by a standard washing procedure (excluding acetone as it will dissolve the insoluble resist as well). Careful handling of the NNP is essential due to its high toxicity.

5.1.5 Raman spectroscopy

I used a 633 nm Raman laser was used to analyze the Raman modes of samples. The majority of the incident light from the Raman laser undergoes Rayleigh scattering, which provides no information, however a small percentage of the beam undergoes inelastic Raman scattering. Light is scattered at different wavelengths and is caused by the photon gaining or losing energy to the vibrational or rotational energies of the chemical bonds in the material. Importantly for this work, it allows the degree of crystallinity of a sample to be characterized as the long range order creates a stronger scattering signal, with a narrower full width half maximum (FWHM) compared with an amorphous sample. Raman spectroscopy only requires a sample area of the same order as the Raman laser spot size, in contrast to ellipsometry, which can only measure the crystallinity at a macroscopic scale. A 10 mW 633 nm laser was used for the Raman spectroscopy in this work.

5.1.6 Ellipsometry

Ellipsometry provides a powerful non-invasive technique for analyzing the optical properties of thin films, specifically the refractive index of thin films and thickness, which can otherwise be difficult to characterize. Ellipsometry works by comparing the changes in a polarized light source after a reflection from the sample. Changes in the amplitude, Ψ and phase difference, Δ are used to construct a model that fits the experimental data with film thicknesses and indices. It is also possible to extract more information such as composition, crystallinity or doping concentrations. Due to being an all-optical measurement, it provides fast results as the sample is not required to be kept under vacuum for the measurement such as in EDX. This also makes it suitable for many different types of thin film samples.

However due to the complexity of the models used to fit the data, it cannot be used in isolation. The Mean Squared Error (MSE) between the experimental data and the model is used as a measure of the quality of a models fit, but it should be used with caution. With so many parameters available to the fitting software, it is always possible to get a near-perfect fit between any model and a data set, at the expense of it being a physical

model. By restricting the parameter space, such as by using estimated values for the index and thickness if they are known, it is possible to build a working model and to have a high degree of confidence in it. Another approach is to only fit part of the model in a fully transparent or absorbing part of the spectrum, then slowly extend the model across the whole range. An M-2000 J. A. Woollam's ellipsometer was used for all the ellipsometry in this work with a wavelength range of 190-1700 nm.

5.2 Experimental setups

5.2.1 High throughput static tester

To analyze the optical response of thin films custom characterization tools were needed. The as-sputtered amorphous films could be characterized using conventional tools such as ellipsometry and Raman, the conditions for successful phase change required a probing station for different optical powers and durations. A high throughput static tester was built to probe a film with laser pulses of different lengths and powers and record the reflection change from each site. A Vortran Stradius 639 nm diode laser was used both to locally heat the film to induce phase change, as well as monitor the reflection from the same area. This choice of laser/wavelength is explained in detail in section 6.3 Figure 5.1 shows the schematic for the setup. Diode lasers were chosen over other types of lasers in part due to the low cost and high power (needed for amorphization), as well as the wide range of available wavelengths which could be easily integrated into the setup due to the identical diode housings. 633 nm was chosen as the diode wavelength as it provided the highest single mode laser power and it takes advantage of the range of optical components designed for this wavelength range, such as the focusing objective. Polarizing beam splitters (PBS) were used to combine multiple optical paths, such as the imaging system and white light source, without any power loss in the incident laser power. The second PBS was used to couple back reflected light from the sample towards a CCD camera or amplified photodetector depending on the need. It also acts like an isolator preventing back reflections from entering the diode laser which can cause instability and damage. To achieve this, a quarter waveplate was placed in the beam path

before the objective. The waveplate rotates the incoming beam's polarization from vertical to circular, then back from circular to horizontal on the return pass after being reflected off the sample. This ensures that the entire beam is reflected by the PBS's instead of being transmitted back into the diode. A removable narrowband filter was placed in front of the CCD camera to prevent saturation by the high power laser. Finally, a high NA (0.5), x50 objective was used to focus onto the sample. The high NA ensured a small spot size (diffraction limited to 450 nm for a 633 nm wavelength), however this comes with the drawback of a short Rayleigh distance of 1.1 μm so precise focus control was needed. This was achieved by mounting the objective to a 3D NanoMax Thorlabs stage. This stage provides 20 μm of closed-loop travel in each axis allowing for fine adjustment to the objective position.

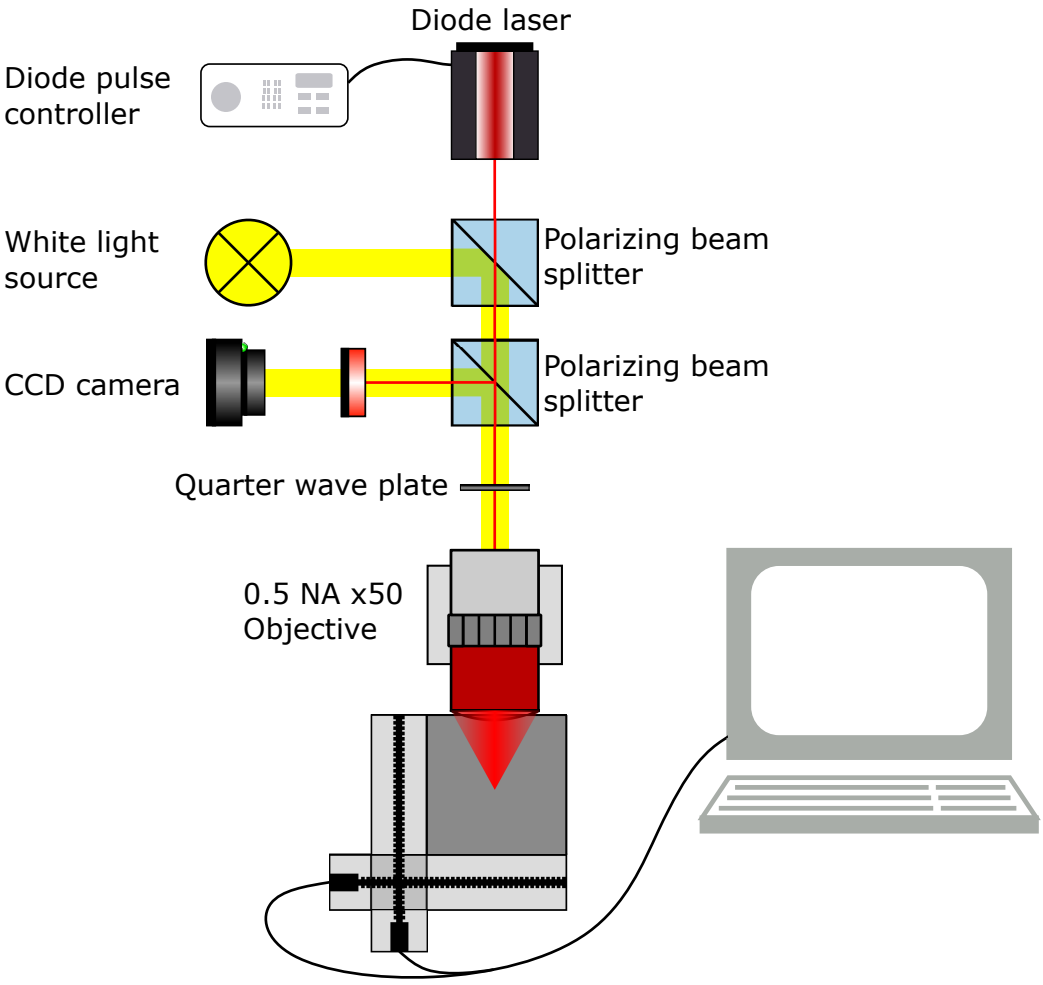

Figure 5.1: Custom built static tester schematic.

The samples were placed on a holder mounted to two 50 mm linear stages, at right angles to each other, each with a minimum step size of 100 nm. In this way, a single sample could be scanned under the objective over a large area, and probed any point in this area. The diode laser was modulated directly by a short pulse generator (Berkeley Nucleonics model 588-OEM) to produce varying pulse lengths and powers, with the camera and stage all triggered through a custom LabVIEW program. Using this custom software, arbitrary control over the pulses allowed for tests of the phase change conditions, as well as the durability of these phase changes on a single position.

5.2.2 Photonic integrated device testing

Phase changing a thin film above a fibre coupled photonic integrated circuit presented several additional challenges which were addressed using a modified version of the static testing setup. An additional linear stage was added to the objective mounting, increasing the travel distance from 20 μm to 50 mm. The 20 μm movement limit of the original stage is the extent of the software-controlled piezo crystals and was not sufficient for scanning over an entire MMI or MZI region. A 2 axis tilt stage was also added to the assembly to give precise tilt corrections to maintain the laser focus over the increased travel distance. Finally, two fiber arms were mounted to 3D stages, either side of the sample holder such that the fibers could be aligned over the grating coupler on either side or a photonic device. A fibre paddle polarizer controller was used to maximize the coupling between a C-band laser and the photonic gratings. Care was taken to ensure that the fiber arms did not interfere with the objective, as the high NA results in a short working distance of 13 mm, limiting the space between the sample and objective.

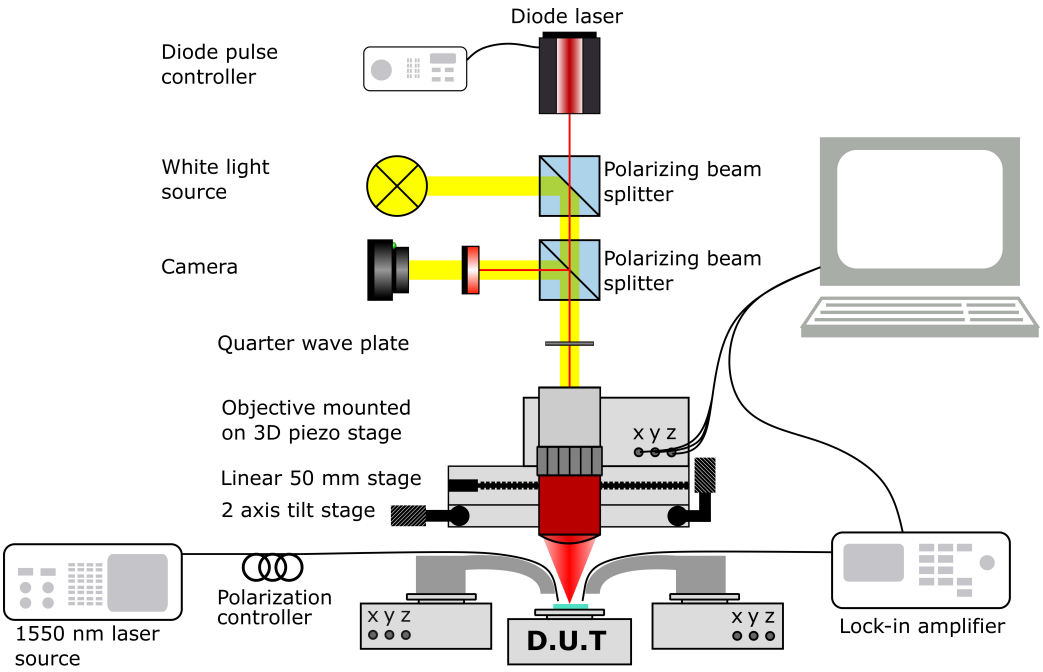

Figure 5.2: Custom setup for phase changing photonic chips whilst simultaneously probing the device's performance.

5.2.3 Fiber coupling

For devices where there were two outputs such as the 1×2 MMIs it was necessary to couple to both outputs simultaneously. Originally a fiber array had been planned for this purpose where single-mode telecom fibers are mounted into a plastic case with a fixed pitch that matches the output grating spacing. Both end facets of the fibers are then polished to be the same height. Unfortunately, whilst it was possible to fit a fiber array beneath the objective, the plastic housing for the array partially obscures the objectives field of view of the device limiting laser power, degrading spot quality and making it impossible to accurately alight the laser spot to the device. Furthermore, any movement of the objective disturbs the fibers as the fiber array is in contact with the objective, causing large measurement error for any transmission tests. To alleviate this problem, I made a custom fiber holder with a lower profile, and no material on one side of the fiber that could obscure the

objectives field of view. This fiber holder was an aluminum arm with two v-grooves micro-machined parallel to each other, at a 250 μm spacing and 125 μm depth. (See figure 5.3a.) This matches the spacing between grating couplers for two outputs of a two port MMI. The arm could be mounted at a range of angles, with 8 degrees being used to minimize back-reflections from the gratings. Mounting the fibers into these grooves was relatively simple, using tape to temporarily hold them in the grooves whilst an epoxy glue sets them in place.

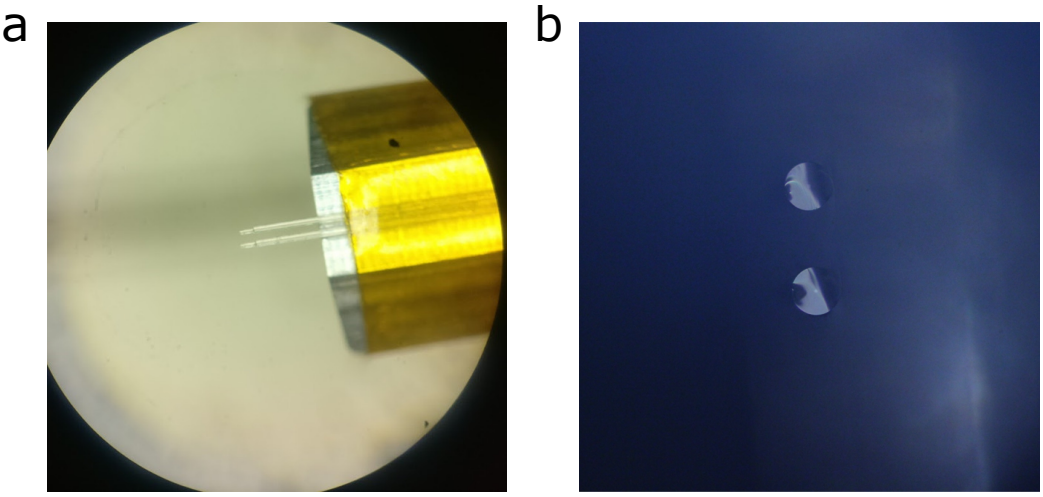

Figure 5.3: (a) Microscope image of the custom fiber holder with two 250 μm single-mode fibers glued in place. The bare silica fiber is visible at the end where the polyurethane cladding has been stripped away. (b) Microscope image of the dual fiber holder face on. The dark region on the left side of each fibre tip is shadowing caused by an off-axis light source.

Usually cleaving fiber tips for photonic coupling is a simple process where the protective polyurethane cladding is stripped away using acetone and the fiber is then held in tension while a lateral force is applied to create a crack in the glass using a ceramic or ruby tip. Finally the fiber is bent with this crack on the outer radius, propagating the crack across the fiber leaving a clean, flat face with high optical transmission. However using the dual fiber holder, if the fibers were cleaved before mounting, then the tips would be at different heights above the photonic chip causing a mismatch in coupling efficiency, and cleaving in situ after being glued up was not possible in the

same way as for a single fibre. Instead a powerful CO_2 laser was used for fiber cleaving the custom array. Using a cylindrical lens, the laser beam profile is converted to a narrow strip which can cut a fiber using a series of high power pulses. Each pulse melts the surface of the fiber before blowing away the liquid silica. This could be used to simultaneously cleave the two fibers with a single laser pulse train, ensuring the cleaved faces are at the same height, enabling coupling into a planar chip. Figure 5.3 b shows the result of this cleave on two fibers using a microscope image perpendicular to the fibers. It can be seen that the two fibers share the same focus, meaning the cleave was successful. On the left side some deformation is visible as a darker region, where the fiber facet is not in focus due to being rough. This is expected at the edges and does not effect the guided light as the mode field diameter is of the order of 10μm at the center.

5.2.4 Laser diode characterization

The laser diode pulses were characterized to ensure the power and duration were consistent and accurate. A high speed silicon detector with a rise and fall time of 1 ns was placed directly in the beam path and used in conjunction with a 5 GHz sampling rate oscilloscope to validate the optical pulse length. The laser diode was driven with a 40 ns electrical pulse using a pulse generator, again with a 1 ns rise and fall time. Using the same definition for rise time as the equipment specifications (the time taken to rise from 10% to 90% of the steady state value) the rise time of the laser diode (a convolution of the diode rise time and electronic driver rise time) was measured to be 4 ns (figure 5.4), with the laser power falling sharply after 40 ns, with a fall time again of 4 ns. This rise time was consistent with the lasers 250 MHz maximum driving frequency and well below the minimum pulse length used for phase change switching, ensuring the same optical pulses were applied for the same given settings.

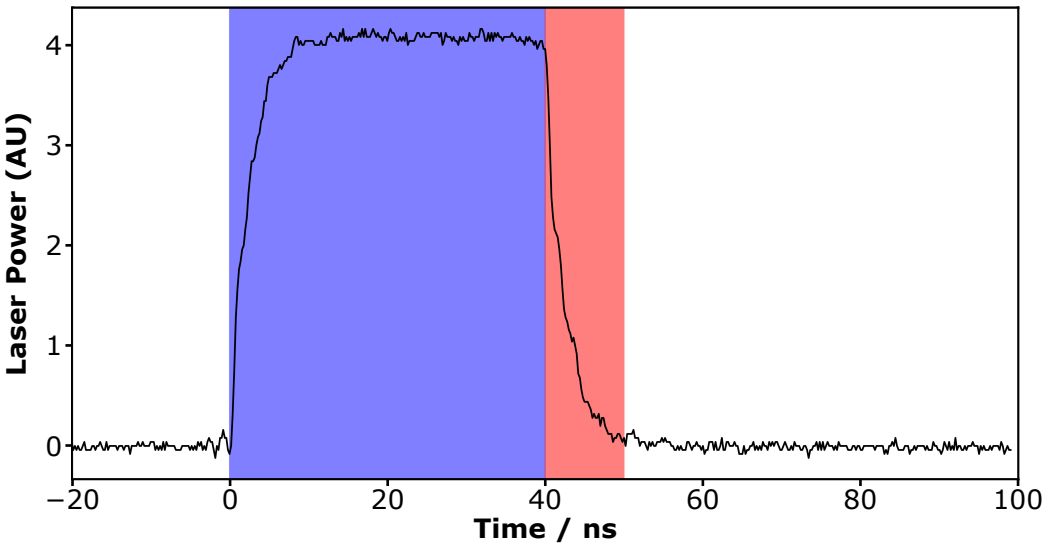

Figure 5.4: Optical power of the diode laser vs time for a 40 ns applied electrical pulse. The 40 ns since the first power increase is shown in blue, with the following 10 ns highlighted in red beyond which a steady state is recovered.

The diode pulse power was controlled separately to the modulation, which only controlled the state of the laser. Analog inputs from 0 to 1 V controlled the power at which the diode lased. A characteristic diode laser curve was seen for the voltage response with a threshold voltage of 0.06 V for lasing and a linear relationship up to 1 V where the maximum optical power of 170 mW was achieved. The losses through the optical system changed depending on the exact experiment configuration and objective alignment so the pulse power should be calibrated separately, however the laser diode power was consistent over time for a given voltage.

Chapter 6

Material Study

6.1 Material Study

6.1.1 Introduction

It became apparent from computer simulations and early experimental results that the most popular phase change material of GST would be unsuitable for this work. As such it was decided that a new low loss alternative chalcogen would be needed. After some useful discussions with a collaborator, Nathan Youngblood, our efforts become focused on Sb_2S_3 due to recent work by Dong *et al.* [166] showing it may have been initially misunderstood when it was described as a write once, read many times material. In their work they were able to demonstrated impressive optical losses for a phase change material in the infrared spectrum, although integration into a planar device and multiple switches of the same volume of material were not shown. Fortunately, due to its wide scale use in photovoltaics, commercially available high purity sputtering targets can be bought. This proved to be cheaper and more convenient than making targets in-house.

For this work there is a range of important material properties that should be balanced to give the best possible performance.

Phase change First and foremost the material must exhibit at least two distinct self-holding phases of contrasting optical properties, which are accessible through a cooling/heating scheme that is feasibly achieved on-chip.

Absorption losses The optical absorption should be minimized in both

phases of the materials at the working wavelengths of the devices to reduce transmission losses.

Index change The difference in the real part of refractive index (Δn) should be maximized to provide the largest effective index perturbation within a device.

Visible absorption The optical absorption in the visible wavelength range should be sufficient to allow for optical switching.

Stability The glass transition temperature, T_g should be high enough that the material is stable at operating temperatures, but low enough for optical switching.

Durability The phase change must be repeatable for many thousands of cycles to make a truly reconfigurable device.

This set of properties represents a significant challenge as when attempting to modify one material property, others are likely to be affected since they are not mutually exclusive.

6.1.2 Design of Experiment

A design of experiment (DoE) is a statistical approach, aiming to minimize the data points needed to adequately sample a parameter space. By choosing a specific pattern of sample sites within a parameter space, the dependence of each variable on the final outcome can be quantified. Once the parameter dependencies are known, it is possible to identify global maxima or minima. To optimize a phase change material, the deposition power and chamber pressure were chosen as the parameters to vary, whilst all others were fixed. The number of samples needed to test more than 2 parameters grows exponentially and from previous material explorations it was known that they were the most important parameters for the absorption of thin films. In this study the power was varied from 1 W to 60 W, to cover the range over which non-damaging depositions could occur. The guns are capable of generating up to 600 W however the targets would start to melt above 60 W. The pressure was varied 1 mTorr up to 20 mTorr, the range in which it was possible to maintain a plasma.

In a true DoE study, there needs to be a single quantifiable result, however the requirements placed on a PCM for wavefront shaping are multi-dimensional. As absorption was the most limiting factor, this was the focus of our first study. Other qualities such as whether a film was capable of phase change would be used to exclude results at a later stage. The run to run variation is also considered by the DoE study, with repeat runs of the same characteristics which would reveal any changes in sputter rate due to target degradation or other factors.

In total 18 samples were sputtered onto silicon substrates, all for a 20 minute duration with the thickness measured by stylus profiling. This gives the sputter rate for each sample, as well as a reference thickness to be used for ellipsometry fitting. To measure the film thickness, Kapton tape was used to partially cover the substrate. After the deposition this was then removed to leave a step height change between the covered and uncovered areas, which could be easily measured as seen in figure 6.1. The heights of the first and last 150 μm were then averaged (red and blue sections respectively) and the difference gives the film height. This approach was taken as there would often be debris at the interface left from the tape which could cause inaccurate measurements, alternatively the stylus tip could "bounce" off the sharp interface and record a non-physical large instantaneous change. As can be seen in figure 6.1 it was common for a the interface to show an instanteous height far in excess of the actual film thickness. The gradients of both averaged sections could then be compared to ensure that the profiling had been leveled and normalized correctly.

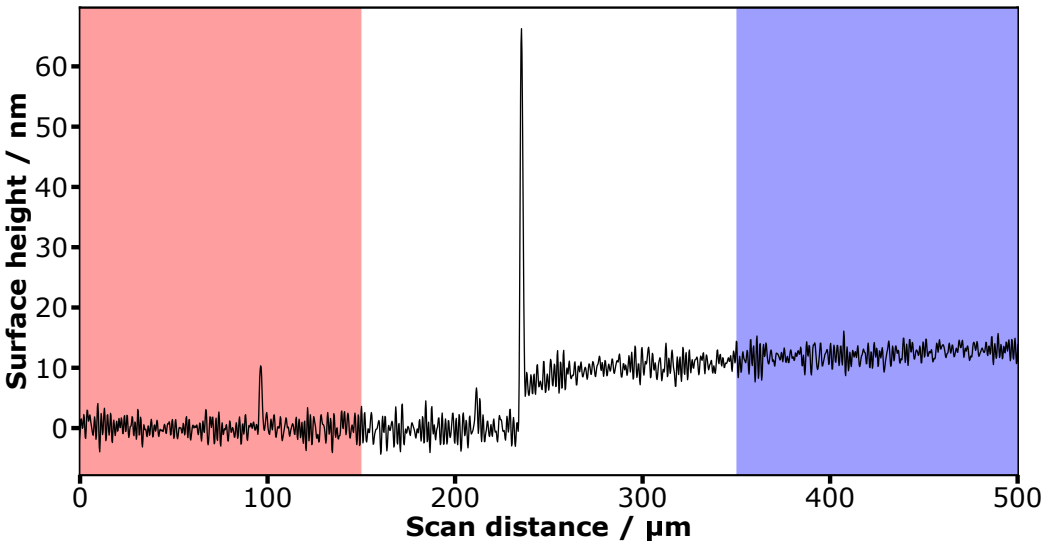

Figure 6.1: Stylus profile scan for the interface between a substrate and sputtered film. The first and last (red and blue respectively) 150 μm were averaged and the difference taken as the film thickness.

The optical properties of the films were then characterized using ellipsometry. A Cauchy model was fitted below the bandgap, as the films are transparent to UV-VIS measurements. Converting this to a B-spline, with the Kramers-Kronig relationship forced to be observed, provides a physical fit that can then be extended down through the absorption edge. Finally a Tauc-Lorentz oscillator can be fitted to this B-spline and extended to the IR wavelengths, as this includes terms for the bandgap. For each samples a meaningful model was generated that satisfied all physical restraints and was in good agreement with the stylus profile thickness results. Many thanks to Ioannis Zeimpekis for his help in generating and fitting these models.

Plotting a heat map of the absorption (figure 6.2) at 1550 nm (as measured using the ellipsometry model described above) shows that it was only for high powers and low pressures where a significant absorption was seen, outside of this the absorption was negligible. A basic interpolation was used to generate the heat maps from the point data, so is only used to help illustrate trends, not calculate absolute values. Figure 6.3a shows the fitted ellipsometry thicknesses for the same films. The film deposited at 2 mTorr

and 60 W has been omitted as the thickness was 1892 nm, and obscured the other data point. The sputtering rate is related to both the pressure and power, with high power and low pressure resulting in the thickest films, and conversely the thinnest films being deposited at the lowest power and highest pressure. The accuracy of the ellipsometry fitting was very good, with an MSE of between 2 and 10 achieved for all models. However as previously discussed, MSE is not always the best indicator of the validity of your model. Here I compared the fitted thickness from ellipsometry with the thicknesses measured by stylus profiler and plotted the difference between the two. (Figure 6.3b) In all cases there was strong agreement, with the largest error being 12% over a 20 nm thick film. This is an absolute difference of 2.4 nm. As all the samples were deposited for the same time period (20 minutes) figure 6.3a also gives the sputtering rate for the various parameters, with 1-2 nm/minute being typical for all samples outside of the 60 W, 2 mTorr sample, where the rate was closer to 90 nm/minute.

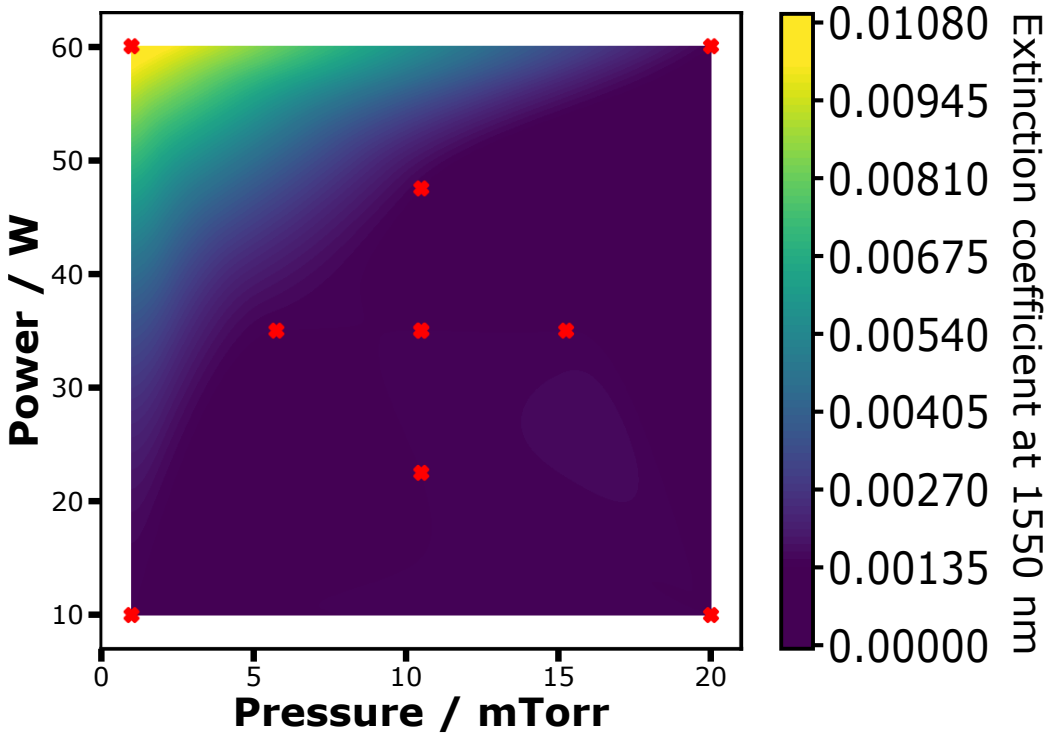

Figure 6.2: Absorption heat map for Sb_2S_3 DoE films at 1550 nm, showing the extinction coefficient against the deposition power and pressure.

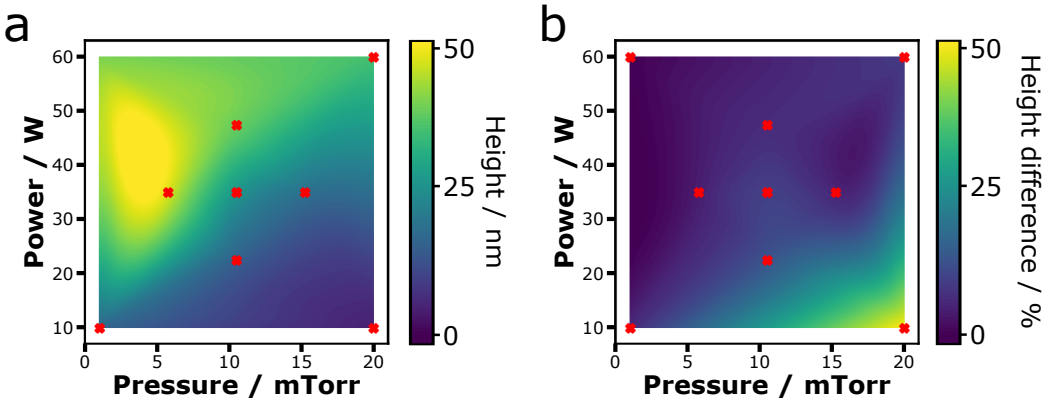

Figure 6.3: (a) Thickness heat map for fitted ellipsometry Sb_2S_3 DoE. (b) Difference between the ellipsometry and stylus profiling results for film thickness.

Having established that the majority of the parameter space is suitable in terms of the amorphous losses and that there was a good agreement between the two thickness measurements, the next parameter to consider was the optical absorption at visible wavelengths. A fully broadband transparent material would be almost impossible to switch optically without designing the substrate or patterning the surface, so a high absorption in the visible wavelength range was desired. Again the DoE could be used to narrow down the parameters for this, with the heatmap of absorption at 633 nm (figure 6.4) showing a higher absorption for lower pressures and moderate powers. For this reason, a recipe using 35 W of RF power with 2 mTorr of argon gas flow was tested as having a suitable absorption edge between the visible and IR wavelengths. However the absorption of Sb_2S_3 in the visible spectrum was still low, which could make it difficult to achieve optical switching. As such, we decided to substitute the sulfur with selenium and deposit thin Sb_2Se_3 films as well. It is well known that selenium can be used in place of other group 16 elements, as evidenced by the research into GeSbSeTe (GSST), where the selenium dopant is used to partially replace the tellurium, which is metallic and highly lossy. The aim in that work was to shift the bandgap towards the IR end of the spectrum, in contrast to this work where by replacing the sulfur we aimed to lower the bandgap and increase the visible absorption, without compromising the transparency of the films at 1550 nm.

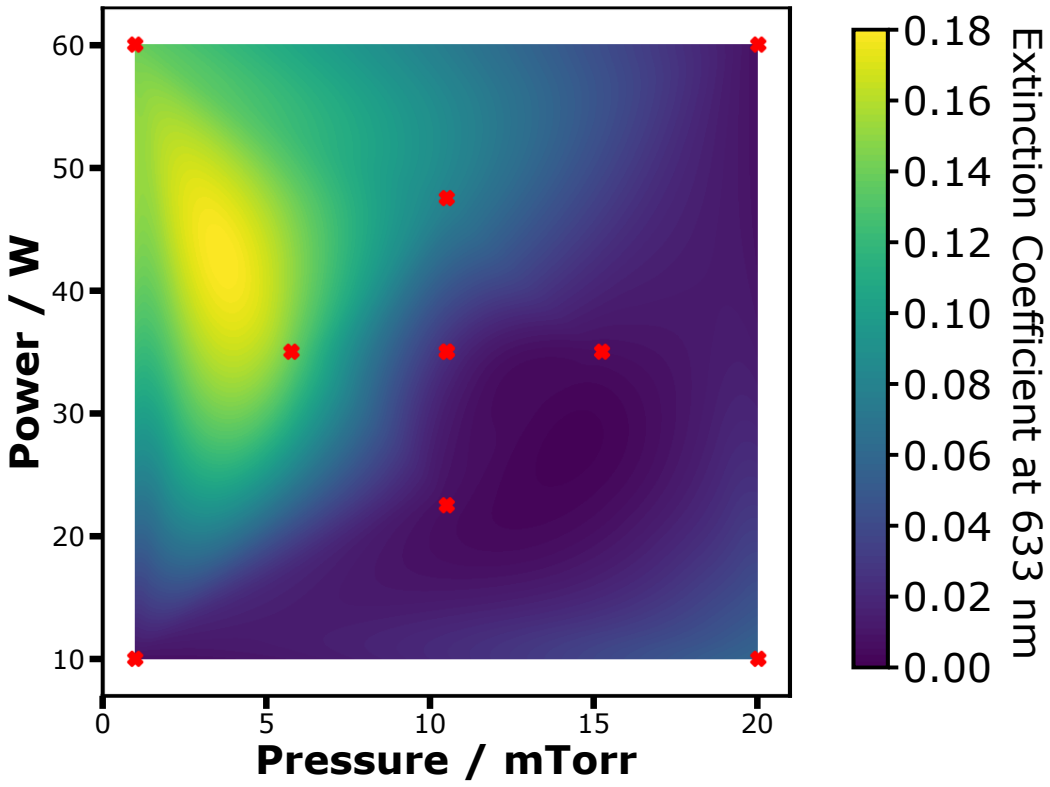

Figure 6.4: Absorption heat map for Sb_2S_3 DoE at 633 nm, showing the extinction coefficient against deposition power and pressure.

6.2 Thin film characterization

6.2.1 Thermal crystallization

Thin films (40 nm) of Sb_2S_3 and Sb_2Se_3 were sputtered under the same conditions (2 mTorr at 35 W), onto crystalline silicon substrates, and capped with a thick (200 nm) ZnS:SiO_2 layer. A thicker film of 40 nm was used here (compared to the 25 nm used in devices) to improve the signal to noise ratio for the ellipsometry measurements. The ZnS:SiO_2 capping layer is an established layer for high-index chalcogenides in rewritable optical media [197],

and provided better protection to oxidization compared to a pure SiO_2 layer. This capping layer was to prevent the films from oxidizing when exposed to high laser powers during phase change. A standard recipe was used for the capping process, 2 mTorr of argon gas at 100 W for 2 hours. The transparent capping layer is to prevent oxidization of the chalcogenide films and form a protective barrier to water and other containments. The film thickness was to increase the The next step was to thermally crystallize the samples and compare the amorphous and crystalline properties, before moving onto laser controlled phase change.

A set of these samples were annealed at a range of temperatures inside of a purged furnace at a variety of temperatures from 100°C up to 300°C. They were all held at temperature for 20 minutes before being cooled to room temperature. The phase of the film was then confirmed using ellipsometry, to find the temperature range over which phase change was possible, and where film degradation was likely to occur. As well as a clear visual color change, there would be a change in the absorption spectrum between the two films. There are more direct ways to probe the crystallinity of a film such as Raman spectroscopy, however for the number of samples tested ellipsometry provided a fast and convenient method that avoided moving samples in and out of cleanroom areas, as well as characterizing the absorption in the crystalline phase, something that up until this point was unknown. Figure 6.5 shows wavelength dependent real part of refractive index for these samples, with a clear two-level system visible in both cases, corresponding to the two different phases. Samples that were heated past their crystallization temperature (T_g) were able to propagate crystal growth as they cooled down, for the Sb_2S_3 this temperature was found to be between 260°C and 270°C, and for Sb_2Se_3 a lower transition temperature between 175°C and 200°C was found. It was observed that the Sb_2Se_3 films started to break down at higher temperatures, and were completely destroyed above 240°C. By contrast the Sb_2S_3 was thermally stable to a much higher temperature of at least 300°C, which may be advantageous for certain applications, particularly in the aeronautical field. However the lower glass transition temperature of the Sb_2Se_3 is desirable for planar photonic applications, where the operating temperature would never exceed the damage threshold, and instead the lower temperatures needed would offer significant power savings for thermal or optical switching, whilst still remaining stable in the environment unlike VO_2. Only a range of T_g are given as the exact values depend heavily on

the cooling scheme, with very a slow controlled cooling rate able to yield a crystalline film at lower temperatures than demonstrated here.

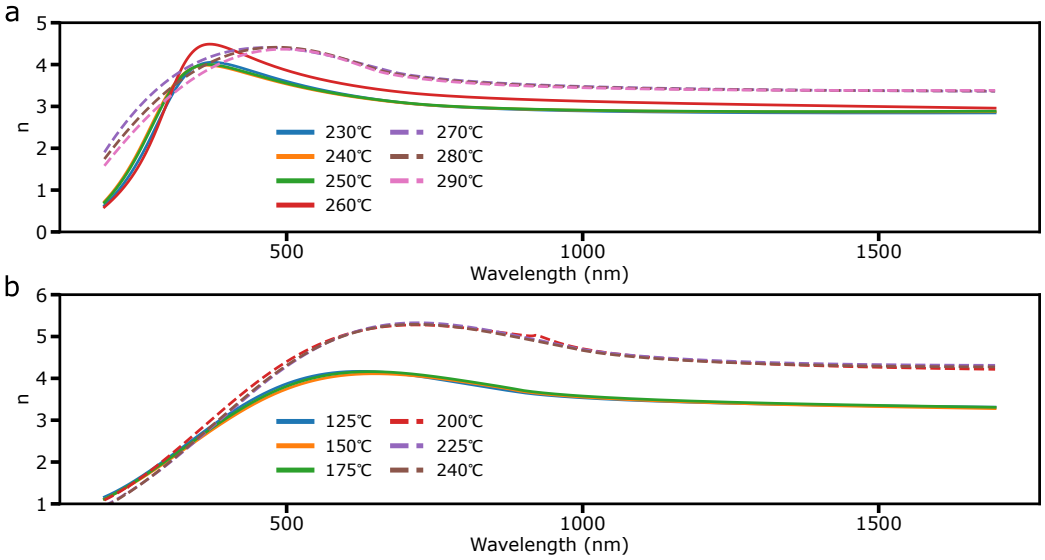

Figure 6.5: Ellipsometry results for thin films of Sb_2S_3 (a) and Sb_2Se_3 (b) annealed over a range of different temperatures, from 230°C to 290°C for the Sb_2S_3 and 125°C to 240°C for the Sb_2S_3. In both cases the films annealed below the T_g are solid lines, with the films annealed above T_g dashed.

The phase and stoichiometry of the films were characterized using Raman spectroscopy and XPS, both before and after thermal crystallization to confirm this was a phase change, and not photo darkening or some other effect. The analysis and XPS spectroscopy were performed by Ioannis Zeimpekis and can be found in the appendix. The Raman showed a clear shift from an amorphous to crystalline film after thermal annealing. The XPS confirmed the films stoichometry, and showed a thin surface oxide as expected. Both the Sb_2S_3 and Sb_2Se_3 were slightly chalcogen deficient, with a 45:55 atomic ratio between the antimony and chalcogen. This was due to the preferential sputtering of the antimony over the chalcogen.

6.2.2 Ellipsometry

As mentioned, ellipsometry has been used to compare the thin films of Sb_2S_3 and Sb_2Se_3 and characterize their optical properties. The fitted models were in very good agreement with the experimental data, with a mean squared error (MSE) of between 5 and 10 reported for all samples with an example shown in figure 6.6. From the ellipsometry it was possible to extract the refractive index values as well as the film thickness for a given sample.

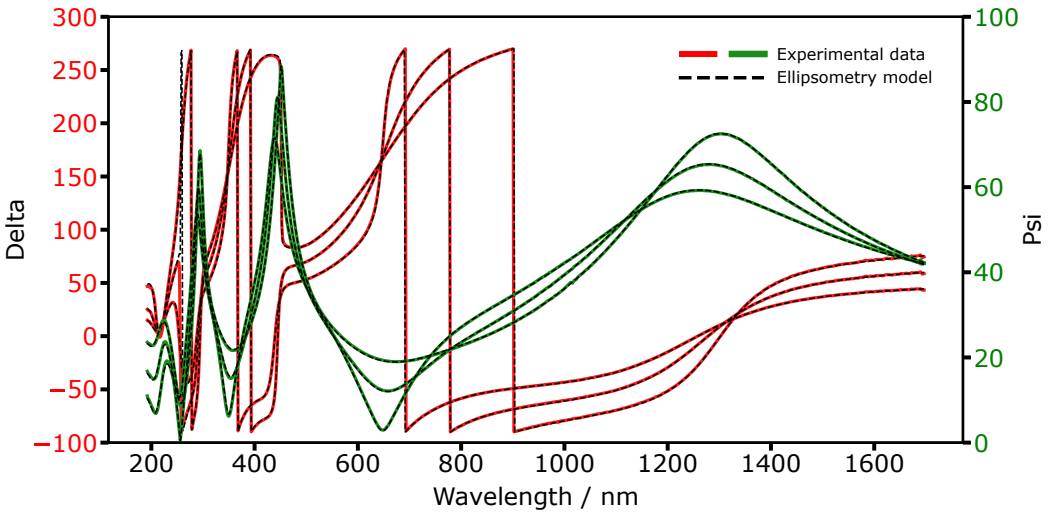

Figure 6.6: The fitted Psi and Delta data from a 40 nm thick Sb_2Se_3 at 60, 65 and 70 degree incident angles. The dashed lines shows the fitting of the model.

In this work the spectra of the films that showed the most promise are compared with GST, the most common PCM, to evaluate their performance as PCMs for photonics. Figure 6.7a and b show the optical constants in both phases for Sb_2S_3 and Sb_2Se_3 respectively. Importantly for this work, there was no measured absorption below the bandgap for either the Sb_2S_3 or Sb_2Se_3 in either phases, with the band edge being well below the telecom wavelengths in all cases. This was the main improvement we had set out to make over GST, which shows strong absorption in both phases at 1550 nm, and constituted a significant contribution to the field of PCM photonics. Figure 6.7c shows the difference in the refractive index between the two

phases of each material. At 1550 nm, both Sb_2S_3 and Sb_2Se_3 show a usable ΔN that could be exploited in a similar way to how GST is currently used, however the ΔN falls short when compared to GST, and so may not be suited to applications where the size of the PCM is critical. The lack of absorption should make it possible to increase the volume of PCM used to compensate for this. For applications that are sensitive to optical losses (most photonic components), the reduced ΔN is more than compensated for by the lack of absorption as evidenced in figure 6.7d. Here the traditional figure of merit (FoM) of $\Delta n/\Delta k$ has been plotted for the three materials.

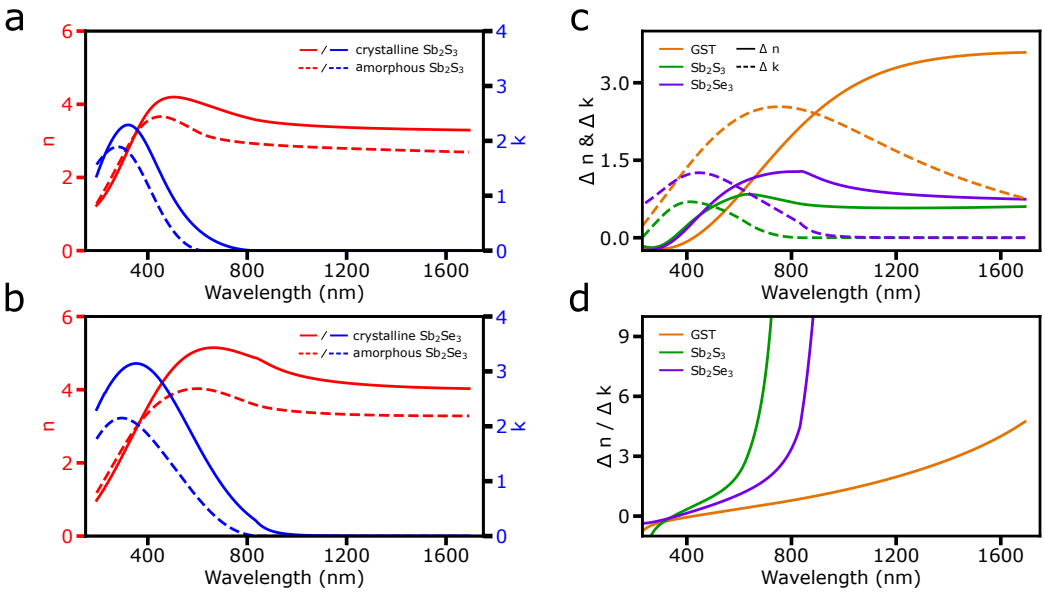

Figure 6.7: Fitted ellipsometry results for Sb_2S_3 and Sb_2Se_3 (a and b respectively). Both amorphous (dashed) and crystalline (solid) phases are shown. (c) The difference in n and k between the two phases for Sb_2S_3, Sb_2Se_3 and GST. (d) The traditional figure of merit, $\Delta n/\Delta k$ for the same materials

For materials with no inherent absorption in either phase, and therefore no Δk this FoM tends to infinity below the bandgap, and becomes a meaningless quantity. Furthermore it was a FoM designed to showcase GST in the best possible light, as for many years this was the leader in PCM photonics. By using only the difference in absorption, a large fraction of the absorption, which is present in both phases could be partially ignored. I believe that a

figure of merit for photonic devices must incorporate a dependence on the absolute absorption losses as an ideal phase change material would exhibit no optical losses. To this end we put forward a new figure of merit [198] (equation 6.1), that includes both the absolute absorption as well as magnitude of the real index shift.

$$FoM = \frac{2\pi}{\lambda}\frac{\Delta n_{\text{eff}}}{\alpha} \tag{6.1}$$

Importantly this FOM also includes the performance of a real world device, as α is the propagation loss inside a straight waveguide in dB μm^{-1}, clad with a PCM. The optical constants alone are not sufficient to describe all the losses induced from the PCM layer. Changes to surface roughness can play a significant role in propagation losses, and if the PCM is in the crystalline phase the different crystal boundaries can act like interfaces above the waveguide contributing to the losses as well. These properties are a function of both the material, and the fabrication process so is less fundamental One drawback to this FOM, is that the strength of the coupling between the waveguide mode and the PCM is a function of the geometry as well as the refractive index so can only be used to compare materials if they are using the same geometry. It also uses α, however this is a phase dependent variable but the FOM in both phases can be compared for completeness, or the higher loss phase (typically the crystalline phase) can be used as this will be limiting factor in most cases.

Due to the lack of wavelength dependent propagation losses I am only able to compare GST, Sb_2S_3 and Sb_2Se_3 at 1550 nm using this new FOM. Specifically, for a 500 nm wide, 220 rib waveguide with 10 nm of GST, or 25 mn of Sb_2S_3 and Sb_2Se_3 the values are 5.15 rad dB^{-1} and 29.0 rad dB^{-1} respectively, compared to 0.282 rad dB^{-1} for GST, an improvement of two orders of magnitude in the case of Sb_2Se_3. The propagation loss values for a GST clad waveguide are taken from citation [199]. A more complete study using this new FOM with different thicknesses and over a large wavelength range would be of significant value to the photonics community.

6.2.3 Propagation losses

To measure the propagation losses of these new PCMs, a range of straight waveguides with different lengths of PCM were used. Using an industrial UV scanner, a wafer was fabricated containing chips with arrays of straight waveguides. These waveguides were 500 nm wide silicon rib waveguides on a 220 nm SOI platform, with grating couplers optimized for 1550 nm. All measurements were normalized to the average insertion losses of unclad waveguides (10 dB $\pm$ 0.9 dB) of the same length. This was to remove the additional losses of the grating couplers and the transmission losses, allowing a direct measurement of the transmission losses of the PCM clad waveguides. As the waveguides are the same length in all devices this is valid, although a measurement of propagation loss within the unclad waveguides using a range of different length waveguides would be ideal. By varying the lengths of the PCM layers it is possible to extract the loss as a function of propagation distance. Laser lithography was used to open windows in a photoresist layer of lengths varying from 100 μm to 800 μm in 100 μm steps. As the sputtering is a low temperature process it is compatible with resist layers, with Sb_2S_3 and Sb_2Se_3 directly sputtered into these windows. A thickness of 22 nm was used in each case as the earlier simulations showed this was a good balance of additional loss and effective index change between the two material phases. After the PCM deposition, the samples were removed from the vacuum chamber and the resist layer removed. This is not ideal as it allows some surface oxide to form on the PCM, which may negatively affect the losses or inhibit phase change in the film. However, if the samples were capped without breaking vacuum, then the sides of the PCM are left exposed which, when attempting to crystallize the samples caused significant damage to the films with void formation and in some cases delamination. This damage is able to propagate inwards from the edges and compromise the waveguides performance. The simple solution would be to partially cap the samples under vacuum, preventing the surface from oxidizing when removing the resist layer, then finishing the capping layer in a second round of depositions that would fully encapsulate them. However, whilst this prevents the surface from oxidizing, it prevents a direct measurement of the thickness of the PCM layer. For a thin film of 22 nm, the error in sputtering rate can results in a thickness difference of several nanometers. Multiple calibration runs, or an internal thickness sensor could be used to measure the film thickness whilst fully en-

capsulating the PCM. Ellipsometry conducted on samples prepared this way had no measurable differences compared to the previously shown results for fully vacuum encapsulated samples.

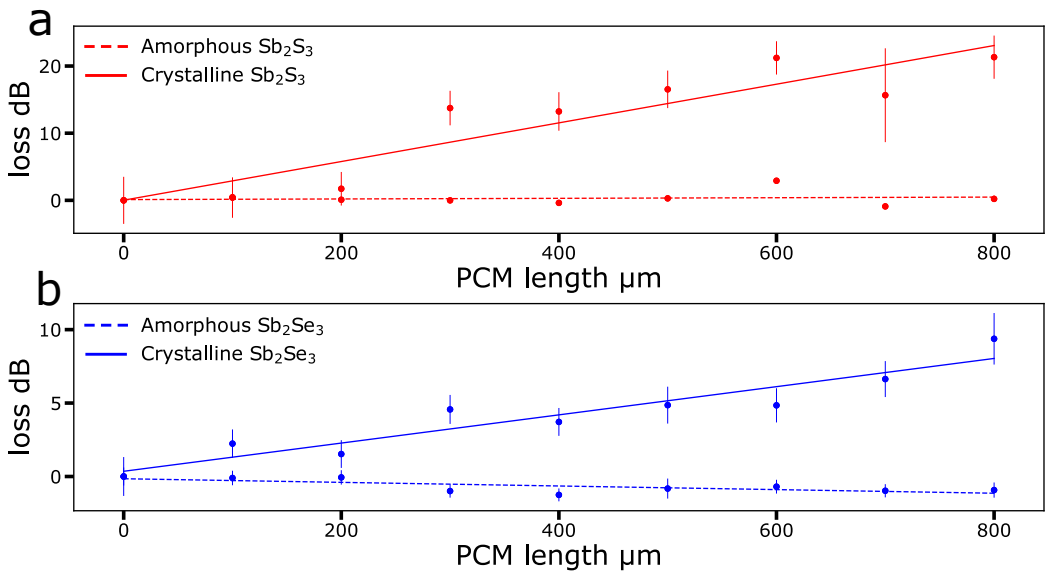

Figure 6.8: Transmission losses for straight waveguides capped with 22 nm of Sb_2S_3 (a) and Sb_2Se_3 (b) in both crystalline and amorphous phase, with fitted straight lines of best fit.

The results of the transmission measurements for these waveguides shows the potential of these materials in integrated photonics. In figure 6.8, a 10 mW, 1550 nm telecom laser was used to record the average insertion loss for each device. The transmission is normalized to the average insertion loss of straight waveguides with no PCM cladding on the same chip, to eliminate the grating coupling loss as well as any losses in the adiabatic taper between the gratings and the 500 nm wide straight waveguides. Multiple measurements at each length were required due to the uncertainly from grating coupling, with the standard deviation shows. The results for Sb_2S_3 are shown in figure 6.8a, and Sb_2Se_3 in figure 6.8b. In both cases the crystalline phase is more lossy than the amorphous phase as expected, despite the negligible absorption losses predicted from ellipsometry where the extinction coefficient was 0. The crystalline Sb_2S_3 had a higher propagation loss of 280 dB/cm compared to the Sb_2Se_3 with a propagation loss of 100 dB/cm. This was

unexpected as the ellipsometry results showed the Sb_2Se_3 having a higher bandgap, so a longer Urbach absorption tail should result in higher intrinsic losses. It was suspected that the different crystal structures and sizes were responsible for additional losses in the crystalline Sb_2S_3 as compared to the Sb_2Se_3 due to the multiple interfaces causing scattering of the guided mode from the macroscopic grain boundaries, however this is unproven.

6.3 Optical phase change

To realize the perturbation patterns used for the modeling, precise optical phase control was needed to amorphize or crystallize the phase change layer. Having established that thermal phase change was possible, the high throughput static testing setup was used to probe the conditions for laser induced phase change. The actual phase change mechanism is a purely thermal process, so a suitable cooling regime should exist using optical pulses. A 638 nm laser diode was used for this experiment. A lower wavelength would provide more absorption into the thin films due to a higher wavelength dependent absorption, as well as having the option of a smaller spot size. 633 nm was chosen due to the abundance of diode lasers and optical components at this wavelength. A multimode laser would provide a higher power, again useful for phase change, but at the expense of the beam quality, and therefore spot size hence a single mode laser was used. The laser diode used could be directly modulated by a signal generator to produce any length pulse from 2.5 ns up to continuous wave (CW) lasing. The optical power could be modulated either directly through the laser, or using a combination of a liquid crystal to rotate the beam's polarization with polarization sensitive optics to partially reject the beam. A white light source was coupled into the beam path to provide illumination, and a CCD camera used to measure the reflection from the sample, as well as image the area of interest. The quarter waveplate in front of the objective acted as an optical isolator to prevented back reflections into the laser. Finally, the sample was mounted to a 3D stage, so it could be placed at the focus of the objective, then scanned in different directions. In this way a map of different pulse powers and durations could be tested. Changing the focus also changed the fluence to give an added degree of flexibility. All the active components were integrated into a

Labview program.

Sb_2S_3 films in both amorphous (figure 6.9a,b) and crystalline (c,d) phases were irradiated with pulse powers from 3 mW up to 90 mW, and for durations ranging from 10 ns up to 300 ms. A picture of each site was taken before and after irradiation, and the change in reflection was recorded (figure 6.9a,c). For the amorphous film there was no positive reflection change at any power below pulse lengths of 100 ms. There was however a slight darkening (resulting in a lower reflection for most pulses below the crystallization threshold, with a slight diffraction pattern visible at high magnification. The most likely cause for this is sulfur sublimation causing void formation in the film, responsible for the diffraction pattern due to the thickness variations, however further investigations are needed to determine the exact cause. At higher powers, visible crystallization was present, and an associated positive reflection change. As the pulse length increases, the power requirements are lower, as expected due to the increased total optical power. Unfortunately the parameter space over which phase change was seen was not consistent as can been seen in figure 6.9b. Pulses of similar energy did not always result in the same crystallization. There are a few possible explanations for this, an inhomogeneous film could result in local variations to the crystallization temperature or the local absorption. The thermally crystallized Sb_2S_3 film showed very strong variations in crystal size and color, possibly due to different polarization sensitivities or crystal orientations. Similar to the results of the amorphous films, there was a clear region of pulses where phase change was seen (figure 6.9c), but again there were problems with the consistency. It is highly likely that the different visual appearances of the film shown in figure 6.9b play a role in this, with a different proportion of power being reflected and absorbed in adjacent crystals.

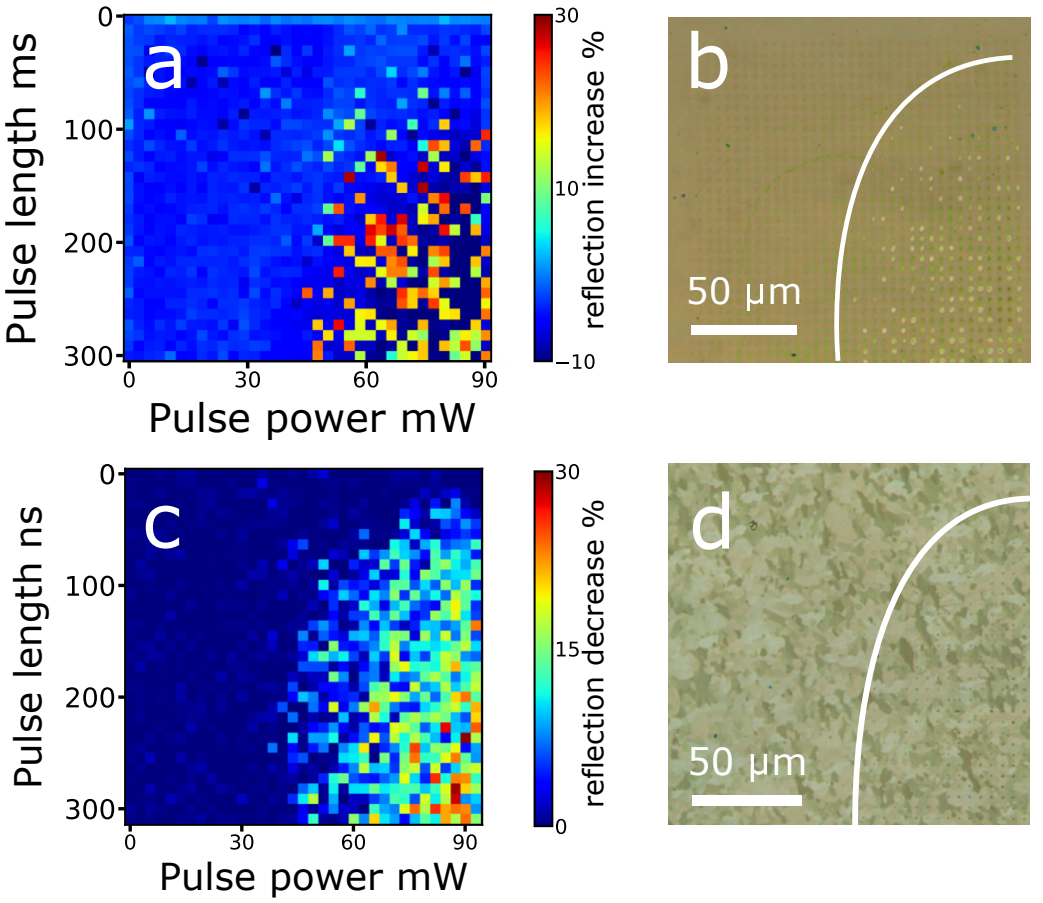

Figure 6.9: Pulse mapping of optical phase change of Sb_2S_3. The reflection change (a) and optical image of the same site (b) for an amorphous Sb_2S_3 film under different optical powers and pulse lengths. (c,d) As in (a,b) but for a thermally crystallized Sb_2S_3 film.

The results of this static testing for Sb_2Se_3 showed a different picture. (Figure 6.10) A far more consistent pulse region was defined for both amorphization and crystallization. For crystallization (figure 6.10a,b) there was some variation along the boundary of pulses, however this is most likely due to experimental noise from temperature changes in the room affecting the fluence. Despite the lower T_g and damage threshold compared to Sb_2S_3, no ablation or void formation was seen as the laser spot size had been reduced to lower the fluence. This was only possible because of the higher absorption

of the film as compared with Sb_2S_3. The larger spot size lowers the peak pulse intensity, and increases the uniformity of the pulse. If a larger spot size was used for the Sb_2S_3 films, no change was seen due to the combination of higher transition temperatures and lower film absorption. There are numerous approaches to mitigate this such as incorporating back-reflecting mirrors to increase the effective path length or using a meta-surface patterning to artificially enhancing the surface absorption, however these are less compatible with integrated photonics, so the unchanged Sb_2Se_3 performance was preferred. In the case of amorphization it was a similar story, with a well defined parameter space for re-amorphization as shown by the first boundary in figure 6.10d). The spot size had been reduced to the original size, due to the higher power requirements for amorphizing. At higher powers and longer pulses there were signs of ablation to the spots that were not easily identifiable in the reflection map (figure 6.10c) as the ablation and amorphization had similar reflectivities. These are shown by the second smaller boundary in 6.10d).

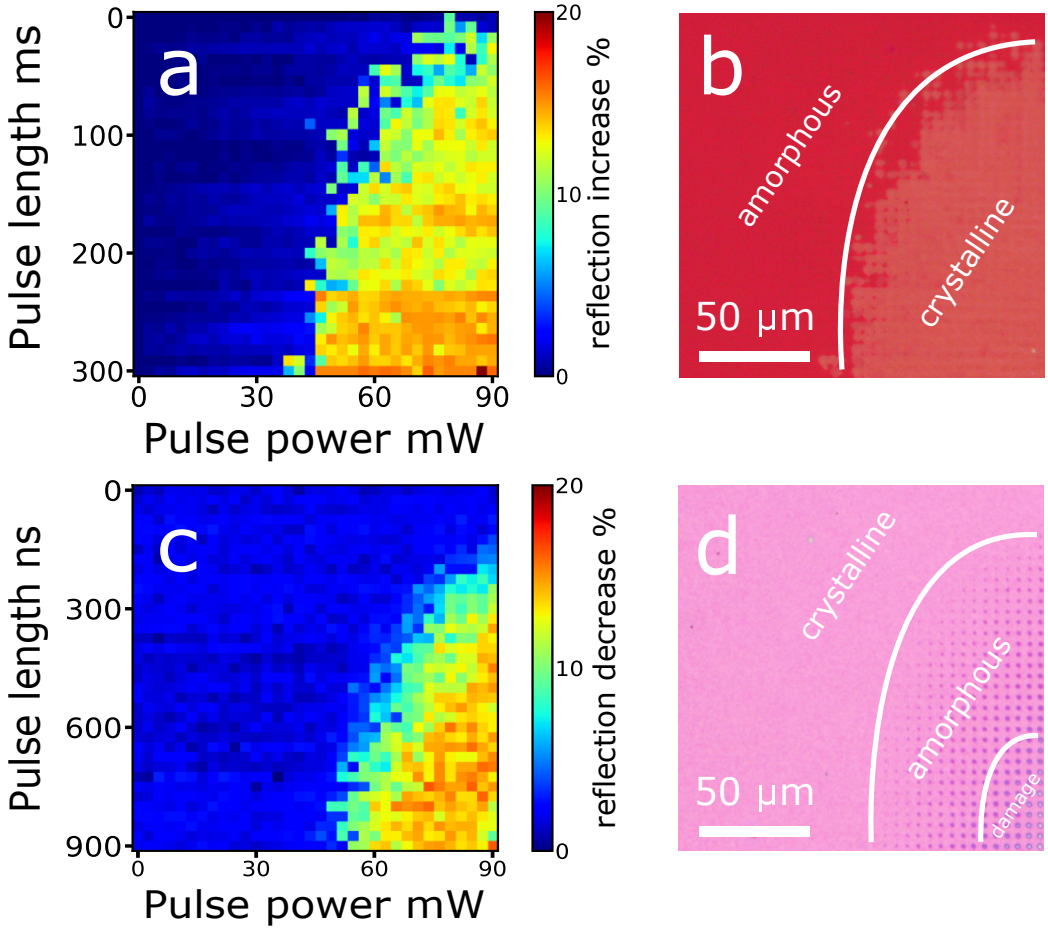

Figure 6.10: Pulse mapping of optical phase change of Sb_2Se_3. (a-b) The reflection change and optical image for an amorphous Sb_2Se_3 film under different optical powers and pulse lengths. (c-d) As in (a-b) but for a thermally crystallized Sb_2Se_3 film.

It was also noted that the crystalline Sb_2Se_3 substrate was more homogeneous than the Sb_2S_3 samples, with the crystal size being sufficiently small so as not to play a significant role in determining the local film properties on the scale of the optical pulses. This difference in the crystalline structure is highlighted in figure 6.11. DIC spectroscopy clearly highlights crystal boundaries, thickness variations or changes in local refractive index over standard microscopy by interfering two otherwise identical beams of polarized light

that have taken different paths through the sample. The images seen are the recombination of these two beams, which amplifies the differences of small variations in thickness, index and polarizability of the sample. Thin films of as-deposited amorphous (a-b) and thermally annealed (c-d) Sb_2S_3 and Sb_2Se_3 were imaged, as well as a large area laser annealed sample (e-f). Using crystallization parameters derived from the pulse maps, a large area could be crystallized by raster scanning a laser pulse over the region. The amorphous films were highly uniform as expected from the sputtering process. A large difference was seen for the thermally annealed samples. The Sb_2S_3 showed large crystals with a grain size of 20-30 μm, compared to the much smaller gain size of 1 μm for Sb_2Se_3. Both samples were annealed for 20 minutes at the respective glass transition temperatures (270°C for Sb_2S_3 and 200°C for Sb_2Se_3). In both cases the crystal growth is nucleation dominated, resulting in the range of orientations seen. It is important to note that the crystal size is as much a function of the precise annealing conditions as it is the materials. The relative densities of nucleation sites play a large role in determining the final crystal size, but with finely controlled cooling gradients it is possible to vary the crystal sizes. However for this work thermal crystallization was not a priority due to the optical switching used for device level work. A full study of annealing conditions might improve the uniformity of the Sb_2S_3 crystallization.

The laser annealed samples show a very different structure to the thermally annealed samples. Unlike the nucleation dominated grown seen for thermal annealing, these samples were growth dominated, with the previous crystallization site acting as the nucleation site for the next laser spot. As such there is an associated directionality of the crystallization in line with the laser scanning.

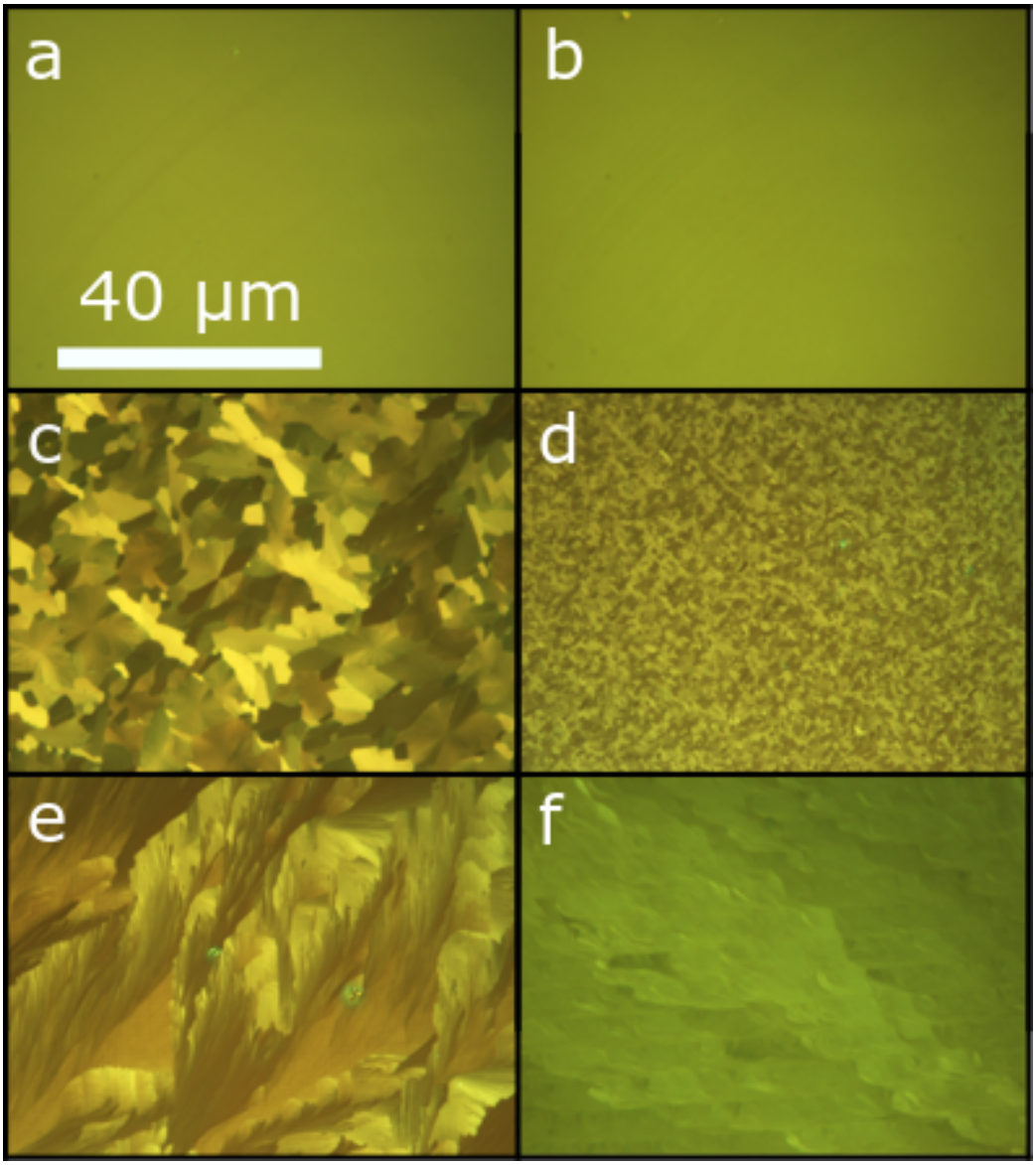

Figure 6.11: Differential interface contrast optical microscopy (DIC) of Sb_2S_3 (a,c,e) and Sb_2Se_3 (b,d,f). The as sputtered amorphous films (a-b), after thermal annealing at 270°C (c) and 200°C (d) and after large area laser annealing using a 90 mW, 300 ms crystallization pulse raster scanned over a large area. (e-f)

One of the most difficult aspects to this work was maintaining a constance fluence for each pulse as the sample was moved beneath the laser. If the substrate was not perfectly perpendicular to the laser then as the substrate was scanned below the laser, there would be a change in focal length (and therefor fluence). Figure 6.12 shows the result of this, where the bottom left corner failed to fully crystallize due to the tilt of the substrate. Other issues are also evident, namely damage caused by some surface dirt enhancing the local absorption of the film in the bottom right.

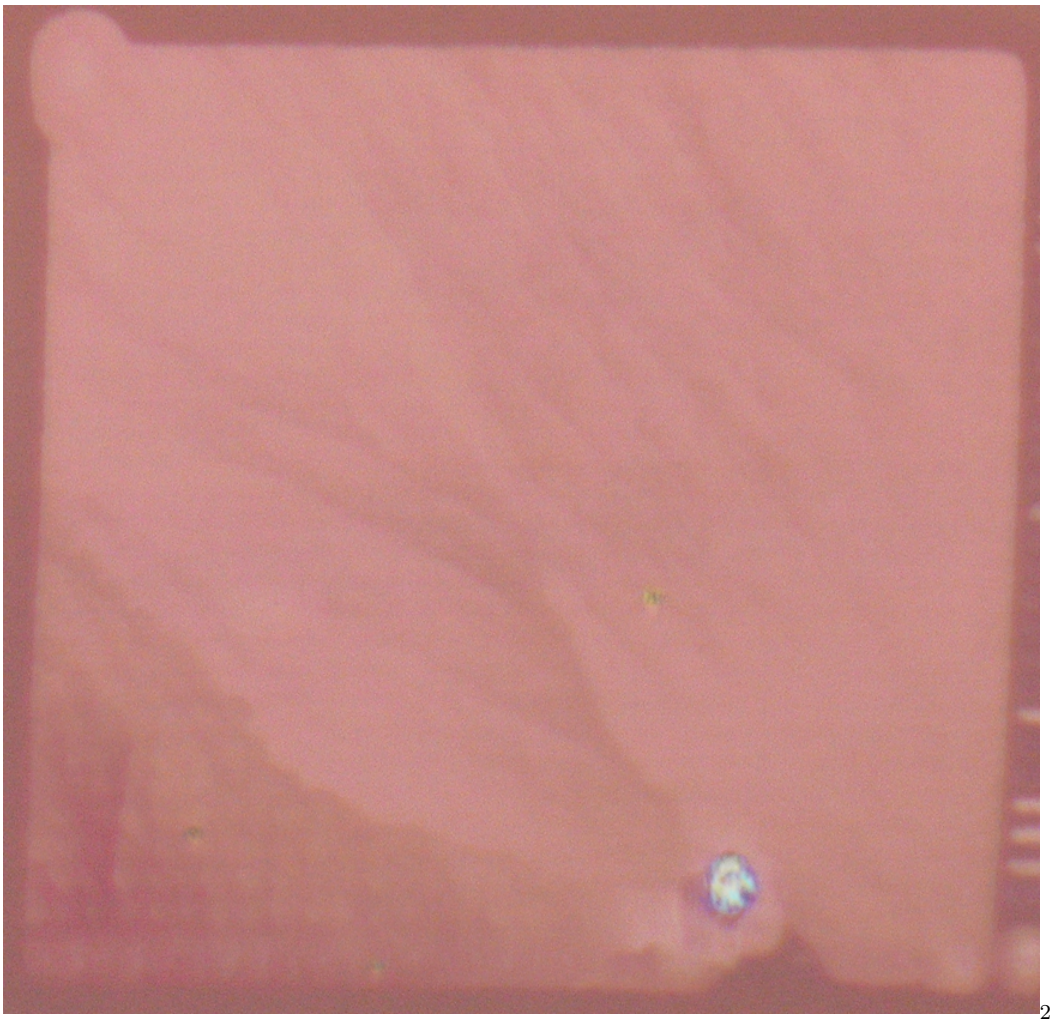

Figure 6.12: Optical microscope image of an attempted large area ($80\mu m^2$) laser crystallization.

6.3.1 Phase change durability

Conventional phase change memories are cycled many thousands of times before they reach a stable switching regime. As such it was decided to test the durability of the phase change, i.e. how many cycles could be achieved before material degradation, as well as if a stable regime could be found with indefinite switching. Using the same experimental setup as before, a single spot in a crystalline Sb_2Se_3 was cycled between the amorphization and crystallization phases until the transmission change was reduced to half the initial value.

The laser power was chosen to be 90 mW in both cases, with the liquid crystal used to modulate between 45 and 90 mW for the crystallization and amorphization pulses respectively. The pulse lengths of 100 ms and 400 ns were selected for the crystallizing and amorphizing pulses from the static tests. Fixing the laser power, and using a liquid crystal to modulate the optical power helped improve laser stability. After each pulse, a brightfield camera image was taken to measure the change in reflection. Figure 6.13a illustrates the switching scheme with the transmission change over time shown in 6.13b. This reflection measurement is made up of the averaged intensity of 25 pixels centered at the site of laser incidence. Each pixel corresponds to a separate intensity measurement, provided the camera response is linear over the range of values recorded and not saturated. This was easily tested using the laser at low powers to verify a linear response over the range used. Figure 6.13c shows the individual measurements for 10 cycles in the middle of the run. Initially stable switching was seen for 4000 cycles, before the reflection change dropped by 50%. There were also step changes recorded in the data at irregular intervals which are likely caused by environmental changes. A climate controlled lab was used for all the experimental work, but the results were very sensitive to temperature changes, due to changes in the objective position affecting the spot size. The objective used has a depth of field of 1.1 μm, so even a 500 nm change in height dramatically affected the spot size, and therefore fluence. A box was built around the experiment out of insulating foam to help regulate the temperature and remove any air currents, however the problem was never fully corrected, with the changes in the time of day or external temperature having a non-negligible effect on the focal position. The noise in the pump and probe lasers was measured as

$> 0.05\%$ in separate stability tests so were not the cause of the drift seen here. A future improvement would be a sample with a clear marker that could be used for real time edge detection and focusing to mitigate this problem.

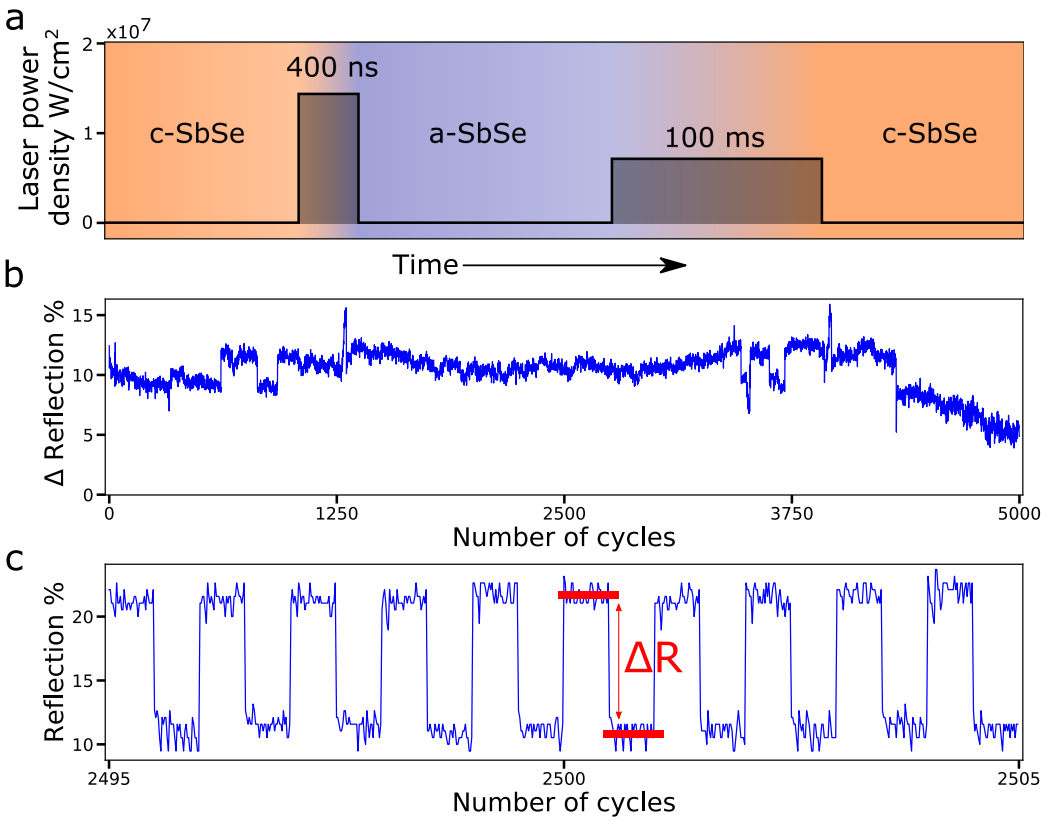

Figure 6.13: (a) Illustration of the pulse scheme used to conduct a durability test of the phase changing. (b) Change in reflection as a function of phase change cycle for a single Sb_2Se_3 spot. (c) The individual reflection measurements which made up the reflection change shown in (b).

The sudden change to the phase change durability at around 4000 cycles is not well understood, but likely due to previously mentioned focal drift. If the fluence was increased above a critical power density, then damage might have occurred at the spot center that then propagated across the whole phase change area. Another explanation is that the change was the accumulated effect of element migration within the film leaving an inert spot.

GST underwent many years of research to achieve the switching stability ($> 10^7$ cycles in commercial phase change memory) that is now associated with it, so the limits demonstrated here may not fundamental limits of the material, but rather a product of the pulses and environment used. An improvement of the lifetime that could be made would be to test a graded pulse scheme that change in power or duration over time to better match the changing material, however with either an amorphizing and crystallizing pulse, each with two parameters at each point in time, the parameter space is huge, and a faster high throughput testing setup would be required compared with what was available.

The same experiment was run with Sb_2S_3. The results were less conclusive (figure 6.14), with some pulse settings resulting in a higher initial contrast, but a much shorter lived phase change. If the pulse powers were lowered then a more durable scheme was found, however with a much smaller reflection change. This suggests that in the case of Sb_2S_3 there was no stable switching of a thin film, with full crystallization and amorphization. If a spot was fully phase changed, there was a decrease in the lifetime of that area and after many cycles, a dark ring was visible around the site. This is likely due to elemental migration of the sulfur from the phase change area to the surroundings. The best compromise between switching lifetime and reflection change only resulted in around 400 switches before the reflection change was reduced by 50%. However, there was no stable switching, and a consistent reduction in reflection was seen at all points. Furthermore, the switching was very varied with a large standard deviation from a 20 point running mean. It was decided that Sb_2Se_3 was a more promising PCM for photonic integration in almost every aspect - it exhibited a higher Δn at 1550 nm, lower switching temperatures and therefore powers as well as lower propagation losses for a straight waveguide, and a longer lifetime of phase switching. Because of these factors, future work focuses primarily on Sb_2Se_3 as the material of choice.

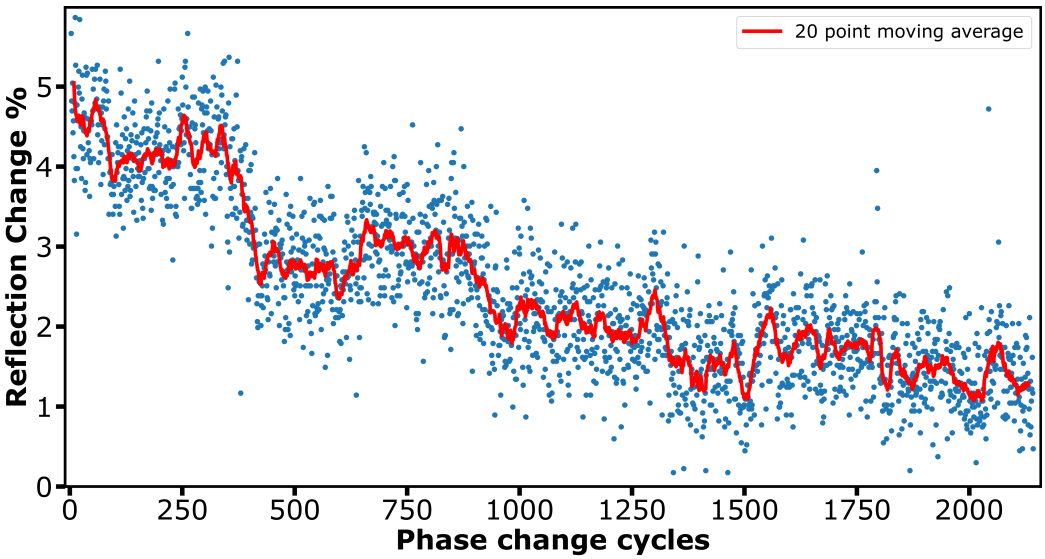

Figure 6.14: Scatter plot for the change in reflection as a function of phase change cycles for a single Sb_2S_3 spot. The red line shows a 20 point moving average.

Chapter 7

Device Characterization

7.1 Mach Zehnder Interferometry

The first step towards demonstrating a PCM based reconfigurable optical router was to characterize the effect of phase change on the effective index of a device. A phase sensitive Mach Zehnder Interferometer device was chosen for this as showing passive phase tuning within an MZI would both validate the material for photonic applications in a planar platform, as well as provide a useful device in its own right if compact low loss phase tuning was realized. A passive tunable MZI would be of great interest to replace the high power consuming thermo-optical tuners commonly found in integrated circuits. The same platform was used as for characterize the waveguide losses; a 220 nm SOI chip with a 120 nm etch was used to fabricate a series of imbalanced MZI's using stepper lithography.

A second lithographic step was used to open windows of varying lengths above one arm of the MZI, and a 23 nm Sb_2Se_3 layer was sputtered onto the sample, before the whole chip was capped with 200 nm of ZnS:SiO_2. After sputtering the Sb_2Se_3 was crystallized using a hotplate at 180°C. The different lengths of PCM would allow for a comparison of the change in extinction ratio, free spectral range (FSR) and insertion loss. One oversight was that no devices were fabricated with PCM patches in both arms. Usually this approach would be used to normalize the reflection losses from the interfaces of the PCM at either end, as well as provide a balanced MZI with a high extinction ratio for any length of PCM. The spectral response of the MZI's was measured using a grating coupled swept source and detector. The modified static tester experimental setup was used to both phase change the films and simultaneously measure the device response.

7.1.1 MZI insertion loss

The Mach Zehnder interferometers were first characterized using a swept source over the wavelength range of 1530 nm to 1600 nm. Figure 7.1 shows the transmission for a range of MZI with and without different lengths of phase change cladding and a straight waveguide to normalize the insertion losses of the grating couplers. The transmission of the shorter MZI's (a-d) showed a better insertion loss than the reference straight waveguide, possibly due to the lower propagation losses in the tapers and MMI's of the MZI's compared to the 500 nm wide waveguide. The additional insertion loss of the MZI were calculated separately using the maxima of each spectrum compared to the straight waveguide as seen in figure 7.2. For the MZI with no PCM (figure 7.1a) the spectrum was as expected with a series of sharp minima. For devices with PCM patch lengths (b-f) the same pattern was present, however as the patch length increased, the extinction ratio decreases. This was due to the lack of a PCM patch in both arms, so the minimal losses of the crystalline Sb_2Se_3 in one arm create an intensity imbalance between the two arms that results in the lack of strong destructive interference. In future devices should be fabricated with patches in both arms to normalize this loss, however it is worth pointing out that the losses are only significant for devices with a patch length of 500 μm or longer. Compared with the 1 μm patch length seen in other work using phase change materials in phase sensitive devices the very low loss of the Sb_2Se_3 allows for very long patch lengths. When this patch length is combined with the reasonable high Δn, these MZI's may act as very compact phase tuners if phase change is achieved without damaging the devices.

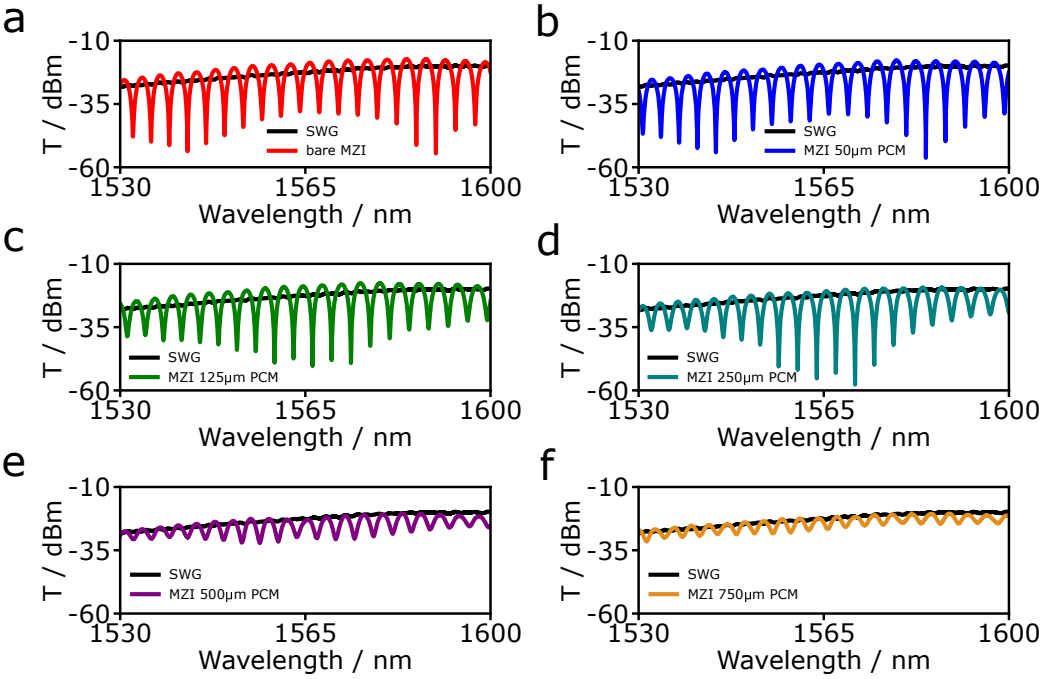

Figure 7.1: The wavelength dependent response of MZI's with different PCM cladding lengths from no cladding (a) and 50 μm (b), 125 μm (c), 250 μm (d), 500 μm (e), 750 μm of Sb_2Se_3 (f), with the transmission of a straight waveguide of the same length for comparison.

There appeared to be a modulation in the extinction ratios between the maxima and minima which was present in all tested samples. The cause of this is unexplained but was not present in spectra taken of other similar devices using a different swept source, so may be an artifact of the source laser. Unfortunately, the source that showed no such modulation was only temporarily available and so we were not able to use across all the samples. This modulation effect had also been observed by a separate research group using the same swept source with a different photonic chip so it was assumed to be an issue with the source, and since a high extinction ratio was not necessary for the first demonstration of this approach to phase tuning, the effect was ignored.

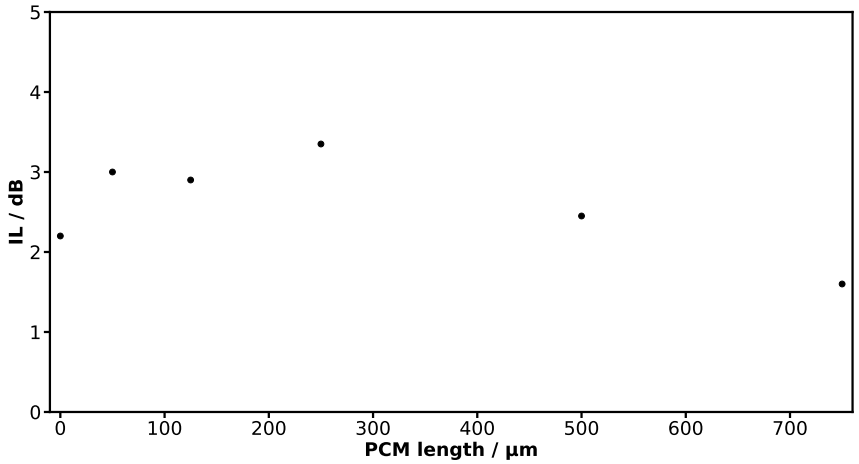

Figure 7.2: The additional insertion losses for a length of MZI clad with Sb_2Se_3 as compared with a straight waveguide with no PCM cladding.

The insertion losses of the MZI's showed no correlation with the patch length (figure 7.2, with the highest additional seen for a patch length of 250 μm, however only a single set of devices were fabricated so further work is needed to add confidence intervals to these results. All of the devices performed better than the reference straight waveguide by $\sim$3 dB. It was suggested that similar to the waveguide transmission losses, the PCM cladding might be acting to reduce the scattering losses of the waveguides, however there was little difference in the insertion loss for the MZI with and without a PCM cladding. Without a range of different lengths of reference waveguides, it was not possible to investigate this discrepancy further, however it is fair to say that the MZI devices were performing well, with no additional transmission losses due to these structures.

7.1.2 MZI single pixel phase tuning

The next step was to phase change the Sb_2Se_3 film above one arm of the MZI's, and record the transmission. If the phase change was successful, the refractive index of the film will change, and the optical path length of

that arm will be decreased (for a crystalline to amorphous transition) and the minima will shift accordingly. Using a single wavelength source, this effect would present as an increase or decrease in transmission depending on which side of a minimum the source is set to. Using a swept source, a transmission peak wavelength was found (1553 nm) for a device with a 125 μm patch of crystallized Sb_2Se_3. A diode laser was used to write 95 amorphous spots into the crystalline film with a spacing between them of 750 nm. This was achieved by mounting the objective to a linear stage and stepping the motor in equal increments. Care was taken to ensure that the objective was mounted perpendicularly to the sample to minimize the focus drift over the range of motion. As the waveguides are only 500 nm wide, and the laser spot is of the order of 750 nm, the alignment in all three axes is critical to maintaining the same fluence at the film about the waveguide.

Each successive laser pulse on a new area amorphized the film, decreasing the transmission to a low of -17 dB as seen in figure 7.3, normalized to the initial transmission. Following this, the phase change was reversed with 35 larger crystallizing pulses over the previous phase change sites, recovering the initial transmission, with an additional loss of 2 dB. The additional loss is likely from the backlash in the stage, resulting in a different positioning in the reverse direction as opposed to the initial amorphization pulses. It is also possible that the laser focus has drifted due to thermal effects in the room or an incomplete recrystallization. The phase change durability should be tested by phase changing a single spot above an MZI for many cycles to observe any degradation to the effect. Other techniques such as SEM or microscopy were not viable due to the thick $ZnS:SiO_2$ cladding and size of the features, however it would be possible to cycle the phase in vacuum then inspect the surface with AFM or SEM to see if there is any significant damage.

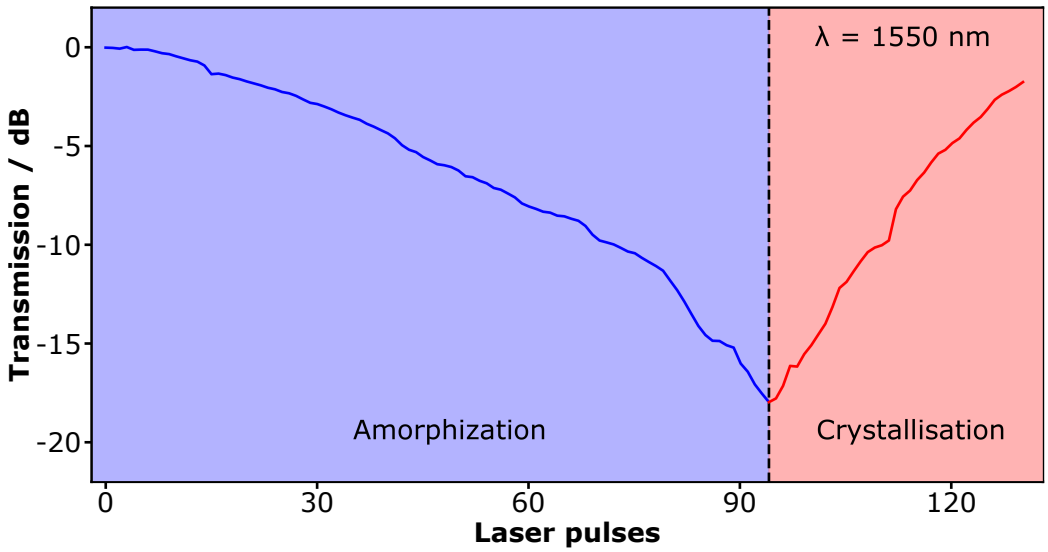

Figure 7.3: The additional insertion losses for each length of MZI as compared with a straight waveguide with no PCM cladding.

If the film was degrading with each optical pulse, then it is expected that the transmission change between each set of pulses during a durability test would decrease until the film was damaged beyond exhibiting any phase chance. To increase the measurement sensitivity, the MZI was first tuned to a minimum so that any transmission change as a result of the phase change was seen as a large transmission change. Figure 7.4a shows the first 400 cycles (including an amorphizing and crystallizing pulse per cycle) of a durability test using a 400 ns, 60 mW amorphization pulse, and a 100 ms 15 mW crystallization pulse. Initially there was a large transmission change between the crystalline (blue) and amorphous (red) states, however after 400 cycles this difference had been reduced to nothing. It suggested that there was a change in the material, either damage or element migration that adversely affected the phase change ability of the film. 7.4b shows the same data, but with a moving average used to normalize away the drift in measurements, showing the clear continuous degradation.

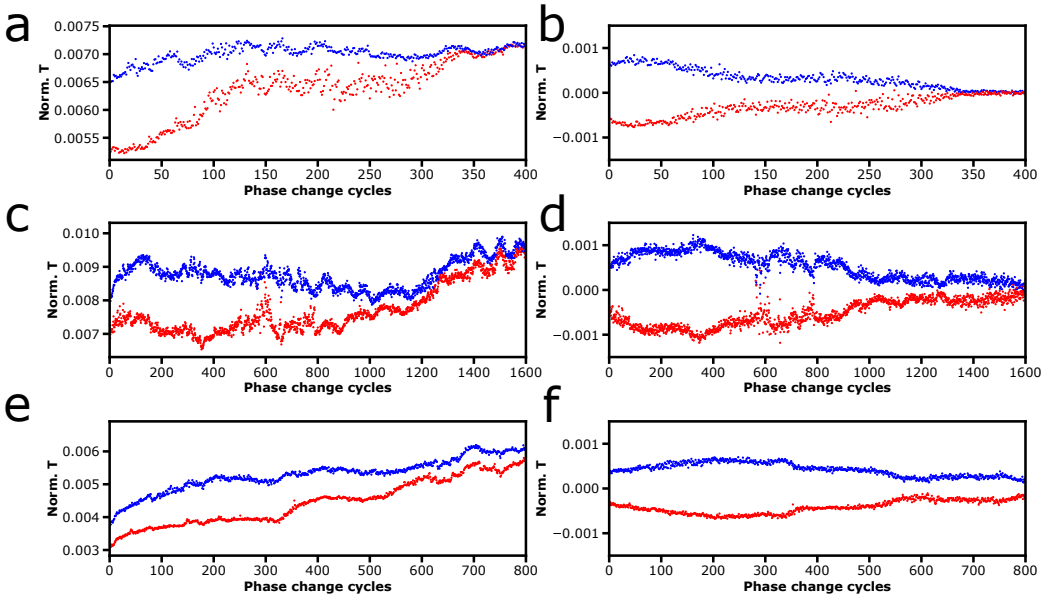

Figure 7.4: (a,c,e) The transmission of an MZI as three different spots were amorphized and crystallized by successive laser pulses. (b,d,f) Using a 10 point moving average the drift in measurements was removed.

A different spot on the same MZI device was tested in the same way (7.4c,d) and a better lifetime of 1600 cycles seen. This may be because when moving to a new test, the objective height relative to the sample changes slightly, varying the pump fluence, or that the alignment of the laser with the waveguide is also different, again changing the fluence. A higher reflection change is seen, suggesting that there was a larger phase change volume in contact with the waveguide, however after the first 400 cycles (where the transmission change increased) again a gradual decrease was seen until, at 1600 cycles, there was no measurable change in transmission between the two laser pulses.

A third site was tested (7.4e,f) with the best lifetime seen. A stable transmission change was seen for the first 350 cycles with a clear transmission change of 20% seen. After this point there is a step change to a lower but still stable transmission change between cycles. It is possible that some environmental factor changed at this point, leading to the difference seen, again likely due to a fluence change. A higher power or smaller spot size

will result in partial damage of the film, lowering the phase change volume in the next cycle, and similarly a lower power or larger spot size will lack the intensity to cause the same level of phase change, again reducing the phase change volume. A second event can be seen at 510 cycles where again the transmission change drops. Unfortunately, it is difficult to isolate the cause of the change, as both a fluence increase or decrease could result in a similar change, as well as if the laser spot drifted so that it only partially intersected the waveguides patch, resulting in a full phase change but at the wrong location. An extension to this experiment would be an automatic focusing system, similar to that used in a DVD drive, where the laser size and position are analyzed after each pulse and small corrections made using the piezo stage that the objective is mounted to. It is unlikely that the results presented here represent the fundamental material limits, as for other similar phase change materials under the right conditions, the lifetime is many orders of magnitude longer than demonstrated here. This assumption is supported that there was little consistency between the lifetime measurements with a wide range of results seen.

7.1.3 MZI reversible phase tuning

The final demonstration using the MZI's was to show a reversible phase tuning using a broadband source. For many applications a reversible 2π phase is sufficient as it encompasses the entire amplitude range in an interference device, such as an MZI. Coupling into an MZI with a 125 μm long patch of 25 nm thick Sb_2Se_3, a 2π reversible phase shift was demonstrated using a series of phase change pulses, as seen in figure 7.5. The initial crystalline spectrum state was recorded, seen in blue, then 100 spots were amorphized using the laser with a spacing of 750 nm between them. A spectrum was taken after every 25 spots. After the full 100 amorphizations needed to achieve a 2π phase shift (shown in black), no measurable change in insertion loss or modulation depth was observed for the MZI, as seen in figure 7.5b, where the spectra are presented with no formatting. In the top plot, the successive spectra have been vertically offset by their extinction ratio depth for readability. The black spectrum was the "set" state, where a 2π phase shift was achieved, before another 100 crystallization pulses returned the device to its initial state (shown in red). The set and reset were not a perfect

match, with some small phase difference between the initial and final states. This is likely due to small misalignments caused by the backlash of the stage creating small areas of phase change that were not reversed. If a perfect 2π phase shift was required, a real-time phase readout could be used as shown in figure 7.3.

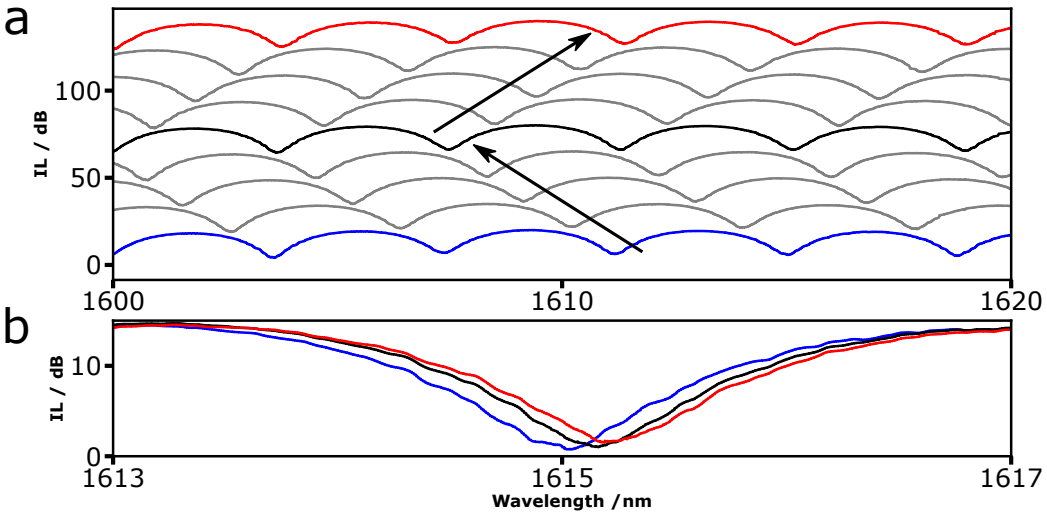

Figure 7.5: Reversible 2π tuning of an MZI using pixels of Sb_2Se_3 to tune the effective index. a) A series of spectra from bottom to top, each after a series of spots is amorphized. The blue spectrum is the initial device response, black is after 100 amorphizations corresponding to a 2π phase shift, and red is after recrystallizing the same 100 spots. All spectra are vertically offset from each other. b) Comparison of the initial, set and reset states without an insertion loss offset.

The optical pulses used for this were low power pulses, compared with the damage threshold, so it is unlikely that the phase change area was the same as the spot size, as has been assumed in previous experiments, however the lower power used resulted in a fully reversible spot, just as during the durability tests. Higher powers did not immediately damage the films, but the complex thermal structure of a narrow waveguide compared to a planar film created challenges in achieving a consistent heating effect. Using a lower power ensured a smaller volume of switching, but no damage to the films. This makes it hard to quantify the area of phase change that corresponded

to the 2π phase shift, however it must be less than 75 μm in length as that is the maximum length over which spots were written. What can be said with confidence is that the phase shift due to a single laser pulse was 0.027π. A 2π phase shift with a 75 μm long device is a fantastic achievement, and is comparable in size to the current best low-loss silicon chip phase tuners, with the added benefit of being a self-holding device. An added benefit is that this approach would work on a variety of platforms, independent of the temperature dependence of the refractive index. For example, silicon nitride has an increased thermal stability compared to silicon so thermal phase shifters are of the order of millimeters in length. A PCM phase tuner could miniaturize circuits within silicon nitride to a larger degree than is possible on silicon, whilst preserving the stability benefits of the silicon nitride.

There are some applications where a greater than 2π phase shift is desirable, as is the case for on-chip Lidar demonstrations. Since this pixel approach is passive it should be scalable with the length of Sb_2Se_3 available. A new MZI was coupled into, with a longer patch length of 250 μm in one arm. For this work the pulse powers were increased to reliably give an amorphization size of 750 nm without any visual damage to the sample or transmission, to increase the phase shift per pulse. 200 spots were written over 150 μm of Sb_2Se_3, again with the same 750 nm spacing, to achieve a 10π phase shift. (Figure 7.6) The phase shift per pulse was increased to 0.07π, more than double the previous demonstration. Again the intermediate states are shown with a vertical offset (a), and a like-for-like comparison of the initial spectrum and final spectrum are in (b). There is a slight reduction in modulation depth of 1 dB, but no change in the overall insertion loss which would be expected if the film was damaged. It should be noted that attempted to reverse the 10π shift was problematic with only a 8.5π shift being shown, leaving a difference of 1.5π between the initial and reset state. It is possible that whilst there was no visible damage to the film there was a change in stoichiometry, reducing the phase change effect, although trying to repeatedly and accurately position a micron size beam over 150 μm was a significant challenge with the stages available. This lack of total reversibility should be explored using a stage with a higher degree of absolute on-axis accuracy.

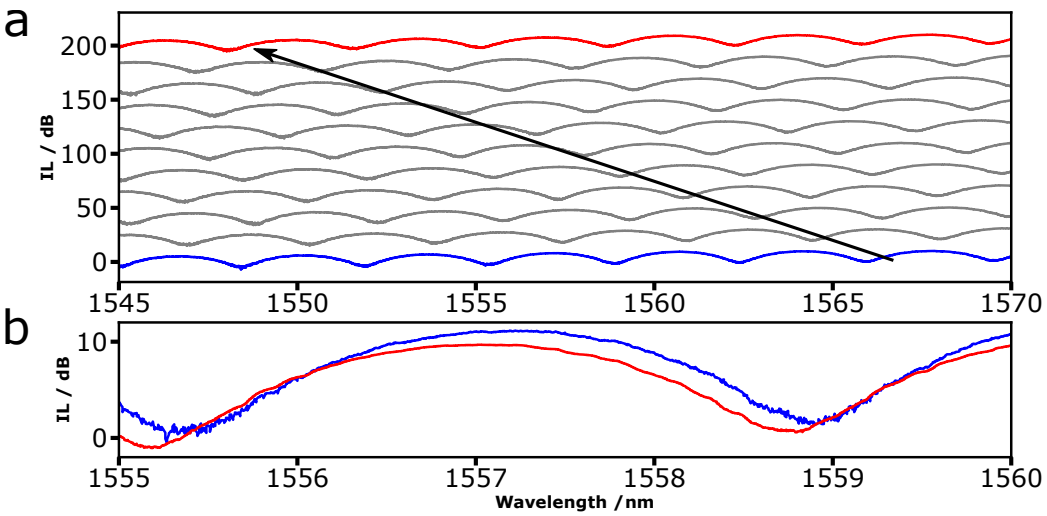

Figure 7.6: Reversible 2π tuning of an MZI using pixels of Sb_2Se_3 to tune the effective index. (a) A series of spectra from bottom to top, each after a series of spots are amorphized. The blue spectrum is the initial device response, black is after 100 amorphizations corresponding to a 2π phase shift, and red is after recrystallizing the same 100 spots. All spectra are vertically offset from each other. (b) Comparison of the initial, set and reset states without an insertion loss offset to allow for direct comparison.

These results are significant as they are currently the first demonstration of reversible, passive low loss phase tuning. This approach could pave the way for passive photonic phase or amplitude tuning in a phase sensitive configuration, whilst consuming less power than conventional thermo-optical tuners and occupying a significantly smaller footprint. They are also inherently insensitive to temperature or wavelength drift making them ideal for low speed applications. Currently the largest drawback is the requirement of incident optical switching, as this is not easily implementable outside of a laboratory and may lack the stability of an integrated solution as the issues with drift would be eliminated. An electrically controlled thermally switched solution would be vital to prove the viability of these materials for phase tuning in more complex circuits. Some work has been done in this direction using Sb_2S_3 [166] which could serve as a starting point to explore the possibility of electrically switching Sb_2Se_3. Doping the Sb_2Se_3 with some tellurium would be an option to improve the conductivity to facilitate electrical switching,

however care would have to be taken to ensure the transparency at 1550 nm is preserved. There are also unanswered questions about the frequency limits of such a device as the switching speeds are yet to be quantified. Here only the speed of the optical pulses has been quantified, which may not reflect the performance of the materials.

7.2 MMI wavefront shaping

The final step in demonstrating a reconfigurable optical router was to use the same approach of index perturbation as used for the MZI's, and apply it to the pixel patterns on an MMI showing in the simulation work. On the same chip as the MZI were fabricated, an array of MMI devices, with a single input and two outputs were all included. The transmission of both outputs of an unclad 1×2 MMI was first measured and compared to a reference waveguide (figure 7.7a) to confirm that the devices were functioning as intended with minimal additional loss. As with the MZI's, the insertion loss was defined by the grating couplers and propagation losses, so was therefore the same for both the reference and MMI outputs. An oscillation is clearly present from the polarization of the input light not being perfectly aligned with the grating couplers. No excess loss was seen for the MMI outputs, as can be seen in figure 7.7b when compared to half the insertion loss of the reference waveguide (as each MZI output accounts for half the inserted power). In fact the MMI outputs showed a small transmission improvement for wavelengths below 1600 nm. As with the unclad MZI's this was unexpected and points towards some additional losses within the reference waveguides that are not present in the other devices. Since the gratings and waveguides dimensions used in both devices are identical by design and the total path length was unchanged in each case it was likely that due to the fabrication tolerances the reference waveguides had an additional loss. A small fabrication error in the gratings for example could easily lead to a difference in loss of the order seen here.

The two MMI outputs were designed to be perfectly balanced, but again due to fabrication tolerances this is never achieved in practice, and whilst the bottom output had a lower transmission on average, the difference across the

whole range was only 0.66 dB, well within the coupling error for our setup. The MMI dimensions were $6 \times 33\mu m$, as modeled in the simulation section, to be a good compromise between functioning when unclad and clad with a PCM. If the dimensions were optimized for an unclad MMI, the transmission was calculated to be 0.06 dB higher, a negligible loss compared to the rest of the device.

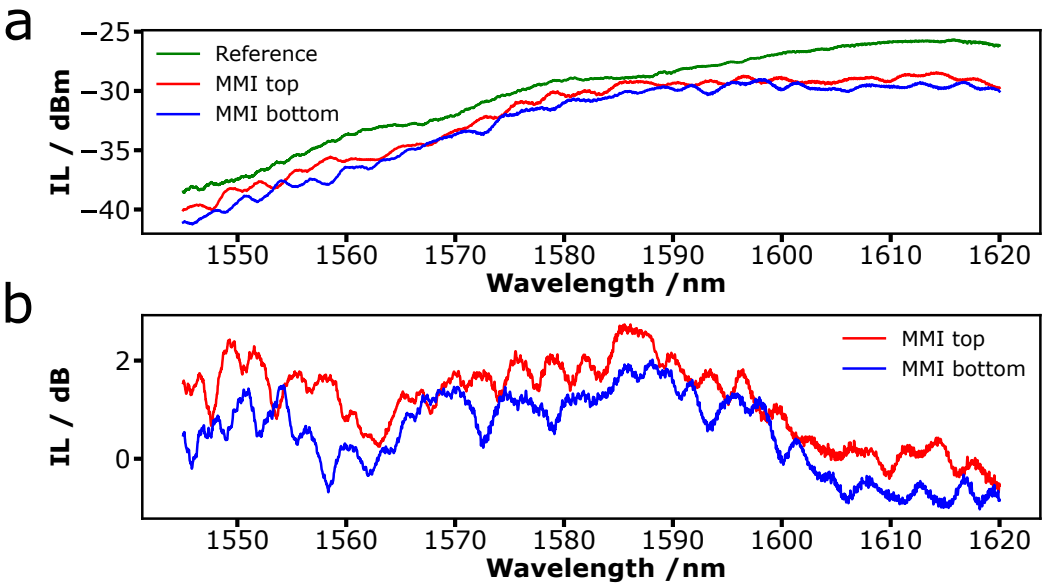

Figure 7.7: (a) The insertion losses of an unclad MMI and a reference waveguide. (b) The MMI insertion losses normalized to the total transmission of a reference waveguide.

7.2.1 Single pixel phase change

The MMIs were clad with a 25 nm thick Sb_2Se_3 film as was the case for the MZI's. From simulations this was the maximum thickness that would not increase the propagation losses of the MMI if the entire PCM film was phase changed. The transmission of the MMIs was again tested and as hoped there was no change to the insertion losses. The increased effective index of the MMIs was compensated for by the dimensions being optimized for an effective index mid-way between the unclad and clad devices resulting in no additional losses.

The final step before writing a full perturbation pattern was to calibrate the laser pulses for the MMI, and to ensure that individual pixels were addressable. An MMI with a crystalline Sb_2Se_3 film was coupled into and a series of pixels written in adjacent positions using the same experimental setup as for the MZI's. Figure 7.8 shows the results, with images 6 and 8 in particular showing the power of this technique. Initially a single pixel was amorphized written in the center of the MMI (2), before adding three more to complete a 2x2 square (3). The pixels were spaced by 750 nm, and at the centers they connected, whilst leaving the very corners of each pixel crystalline. This was approximately consistent with the 750 nm square spot size used for the simulations. In all the images there is a damage site visible (center of MMI) where a previous amorphizing pulse was tested using a duration that caused ablation and not phase change.

In images 5 through 7 the central pixel in a 3x3 array was successfully re-crystallized then re-amorphized, whilst the outer positions remained unchanged. This was an important result, proving that with the correct pulse parameters it was possible to write adjacent pixels without changing the surrounding pattern. Had this not been the case, then the tested pixels patterns would have to allowed a buffer space between pixels, reducing the pattern density and therefore final extinction ratio. In the final image the entire region can be seen after re-crystallization with no permanent changes compared with the initial area.

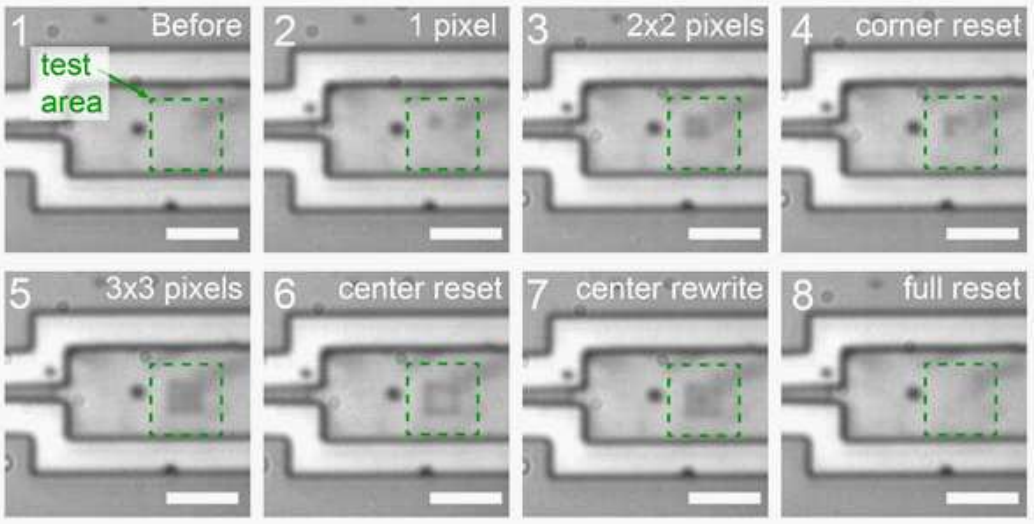

Figure 7.8: A series of pictures taken through the pump laser objective showing the capabilities of the optical writing. Images 6-7 show the ability to write and rewrite a pixel in the middle of a block without altering the surrounding pixels. Panel 8 shows the quality of the resetting, which was able to completely remove the amorphous pixels.

The pulse power and duration for reversible amorphization required a high degree of repeatability, as if a pulse of too high power or duration was used it would cause a permanent change to the local film, with the amorphization being only party reversible. For all this work a pulse power of 50 ms at 19 mW was used for crystallization and 400 ns at 35 mW for amorphization. This gave the highest margin for error in pump fluence without causing permanent changes to the film. Figure 7.9a shows five amorphous pixels written into a crystalline film using 400 ns, 40 mW pulses. After applying a crystallization pulse there is still an obvious darkening to the film in the same area as the previous amorphous pixels. (Figure 7.9b). Attempting to fully reset these positions with increased duration or power crystallization pulses only resulted in damage to the films.

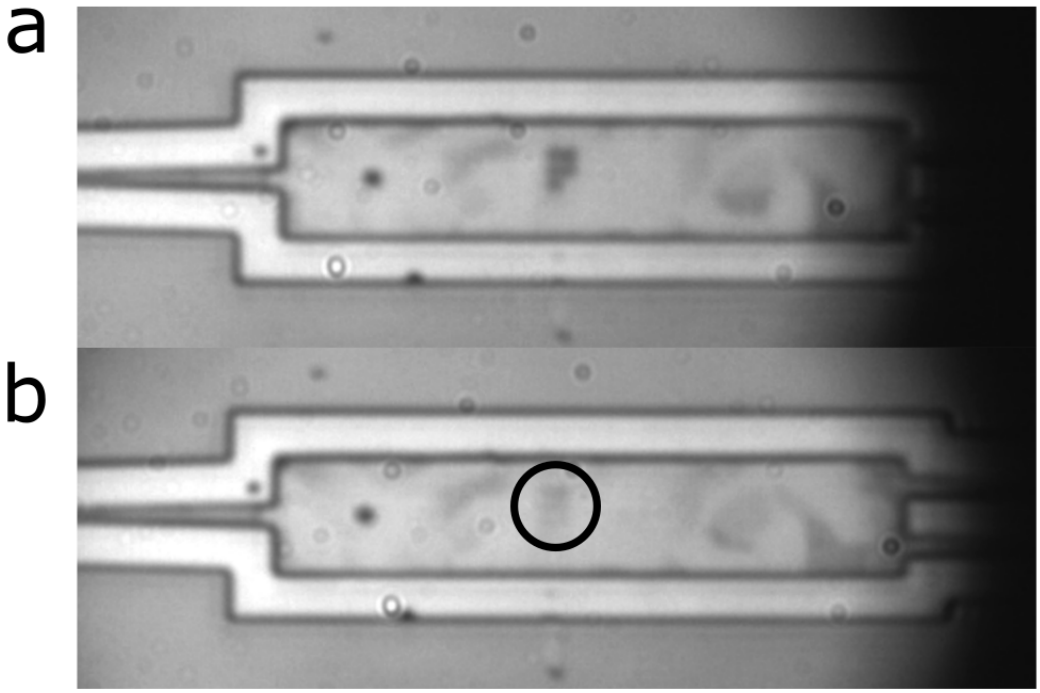

Figure 7.9: Pictures of an MMI before (a) and after (b) attempting to reverse 5 amorphization. The amorphizations are clearly visible even after resetting.

7.2.2 Optical routing using a perturbation pattern

The final demonstration of this technique was to write a guiding pattern into a PCM above an MMI to demonstrate on chip wavefront shaping. A pattern was optimized using the 2D linear simulation approach and written into an MMI with a 25 nm crystalline Sb_2Se_3 cladding, using the same setup as for the MZI. The simulated electric field within the MMI before and after writing the pattern are seen in figures 7.10 a-b. The pixel positions are shown using a translucent white square in 7.10b. Figures 7.10 c-d show the results of experimentally writing this pattern into the MMI. In 7.10c the darker patches are different crystalline orientations within the film, resulting in a lower reflection. This is a result of the nucleation dominated crystal growth from thermally annealing the samples. Figure 7.10d shows the completed pattern, a near-perfect reproduction of the simulated pattern, with some

slight rotation misalignment. The experimental pattern was also shorter than the actual device length as the motor used to step between pixel positions has an internal miscalibration of 2.3%. Whilst not ideal, this error is small and the patterns were numerically shown to be resilient to small misalignments of this order. Figures 7.10 e-f show the real-time transmission for the top and bottom output of the MMI whilst the pattern was written. The dashed green and teal lines show the expected transmission from a 2D simulation at each stage of the pattern. A splitting ratio of 92:8 was seen between the two outputs for the completed pattern, lower than the simulated 99:1, however a very successful result, and the first of its kind for a self-holding router. The final pattern was also simulated using a 3D environment to encompass the out of plane scattering effects of the pixels, which is lost for the 2D simulations. The results of this simulation can be seen as the crosses in 7.10e. Due to the simulation time it was not possible to optimize a pattern in 3D, so the pattern presented here likely leaves room for improvement. The agreement between the experimental and 3D simulated was better than with the 2D simulations and showed a remarkable similarity given the assumptions made and the large margin for experimental error in terms of rotational alignment and absolute pixel positioning. There were previous attempts where a lower splitting ratio was achieved due to these errors, or a partial pattern being written due to incorrect pulse parameters.

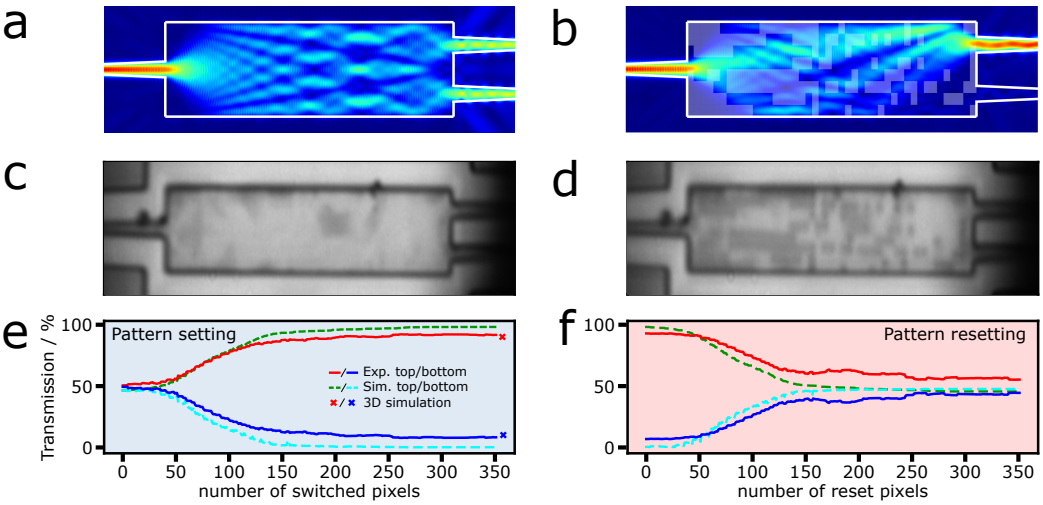

Figure 7.10: (a) Simulated unperturbed electric field intensity inside an MMI. (b) Simulated perturbed electric field inside an MMI with a pattern predicted from modeling. (c) Picture of an MMI with a crystalline Sb_2Se_3 film deposited on top. (d) As in (c) but after the perturbation pattern from (b) has been optically written as amorphous spots into the film. (e) Transmission for the top output (red) and simulated top output (green) compared with the bottom transmission (blue) and simulated bot transmission (teal), as a function of the number of pixels switched in the perturbation pattern. (f) As in (e) but for rewriting the pattern, to a fully crystalline film.

The pattern was reset from the start of the MMI, pixel by pixel so an asymmetric result is expected. Figure 7.10f shows the splitting ratio as the device was reset, with the experimental results diverging from the simulation. The initial 50:50 splitting was never recovered with a 55:45 final splitting ratio between the top and bottom ports. There are several effects that could cause this, although most likely it is due to an imperfect reset of the local phase, either due to damage caused by the initial pass or the resetting optical pulses being too weak to fully reset the initial pixel. Given the lifetimes observed for the MZI switching, it is expected that with careful pulse tuning this could be addressed.

Each complete pattern could be written in approximately ten minutes (depending on the number of amorphization spots), however this slow write

time was due to conservative wait times for the stepper motors to ensure the highest degree of accuracy. Using a digital micromirror device (DMD), similar to one used in a projector, it would be possible to write the entire pattern simultaneously if there was enough pump power available.

Where this technique differentiates itself from other passive reconfigurable approaches is the total transmission. It is easy to achieve a higher extinction ratio between two ports, simply using a loss inducer, such as crystalline GST in one arm, or a destructively interfering MZI. The extinction ratio of 11 dB presented here is not as impressive as the extinction ratio's achieved with these other techniques, however the excess loss in the system is unparalleled for a passive device. In figure 7.11 the total transmission for the same optimization is shown. Normalized to the initial unperturbed transmission, 7.11a shows the transmission as the pattern was written, and 7.11b for the reset. The total transmission increases during the initial setting to a maximum of 1 dB, suggesting this is a lossless technique, and is in fact improving the unperturbed devices' total transmission. This could be a useful application for improving the transmission of a critical component in a larger circuit if there were issues during fabrication. During the resetting of the device there was an overall reduction in transmission to a minimum of -0.5 dB. However the final result was an overall transmission increase for the reset device. Ideally a value equal to the initial level (0 dB) would be recovered, so the discrepancy indicated that there was some error in the measurement. Running the transmission measurements without any perturbations concluded that there was some drift in the recorded values, almost certainly due to changing environmental factors. The setup is very temperature dependent as any temperature change will cause thermal expansion or contraction in the fiber coupling arms and objective mounting, causing misalignment. For example, given the thermal expansion coefficient of 20×10^{-6} m/(m °C, a 1°C temperature change over the 10 cm aluminium fibre coupler arms causes a 2 μm misalignment at both grating couplers, a significant misalignment between a 10 μm grating coupler and an 8 μm mode profile within the fibre.

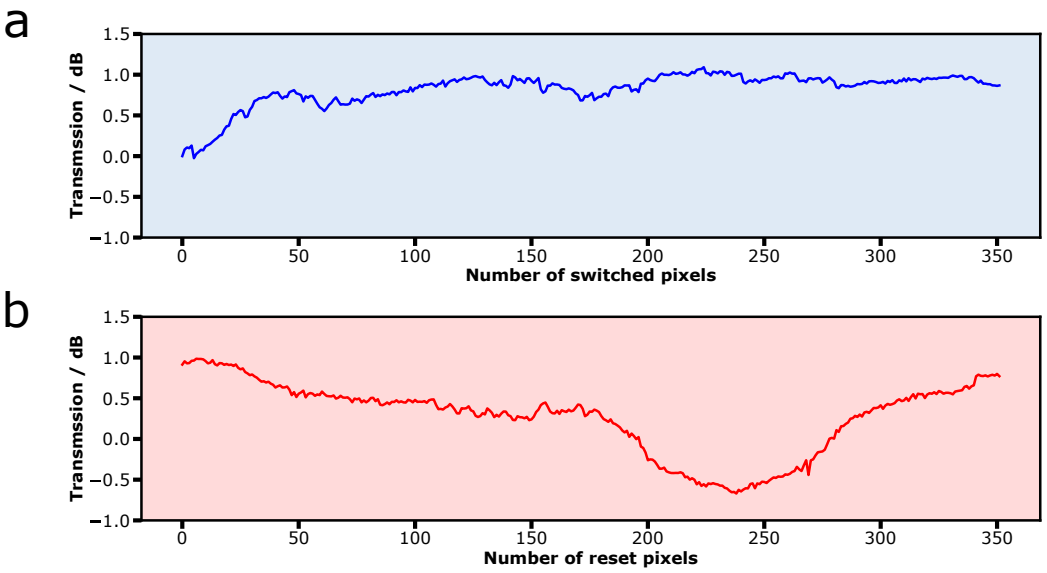

Figure 7.11: The total transmission through both ports of the MMI, as a function of the number of pixels set (a) and reset (b)

7.2.3 Pattern durability

Having shown a pattern could guide light with a high efficiency, it was necessary to test the device for multiple cycles to prove the reconfigurability of this technique. The Sb_2Se_3 film above an MMI was written with a pattern as before, then fully recrystallized several times. The pattern was also rotated around the axis propagation, as due to reciprocity, any pattern that guides light towards the top output would work as efficiently when inverted to guide the light towards the bottom output. Figure 7.12 shows optical images of the MMI taken after each pattern write/rewrite. 7.12a is the initial unperturbed MMI, where different crystalline orientations are clearly visible. Figure 7.12b shows the same MMI after writing a pixel pattern into the Sb_2Se_3 film. In 7.12c-i image differencing has been used to show the pattern after successive writes and resets to highlight the pattern to pattern changes. It is clear from these images that the MMI does not fully recover to the initial state, and that there was successive damage to the edges of the film, particularly in the bottom right corner. As the optical pulses were optimized

using the center of the MMI, where the thermal mass of PCM and silicon differs to the conditions at the edge, they may be unsuited to the corner positions. At the borders of the MMI, a pixel is partially insulated on one side by the ZnS:SiO_2 capping layer used to encapsulate the films. The thermal conductivity of the capping film is two orders of magnitude lower than that of the silicon MMI, leading to a higher local maximum temperature for the same optical pulse. It is no surprise then that this damage first occurs at the corners of the MMI, where the cladding insulation is maximized. Once there is damage to the Sb_2Se_3, the transparency is compromised and successive pulses quickly damage the surrounding areas, leading to growth dominated damage. Calibrating a lower pulse energy for the pixels along the edges and corners of the MMI could mitigate this unwanted effect, or patterns could be found that avoid these pixel positions completely without compromising the performance. This should be possible as the electric field in the corners of the MMI is negligible, and as the perturbation mapping showed, these areas have little contribution to the guiding effect of a pattern. Introducing a small threshold increase needed per pixel would eliminate these positions and reduce this issue, however a different pulse scheme that allows access to the whole parameter space would be preferable.

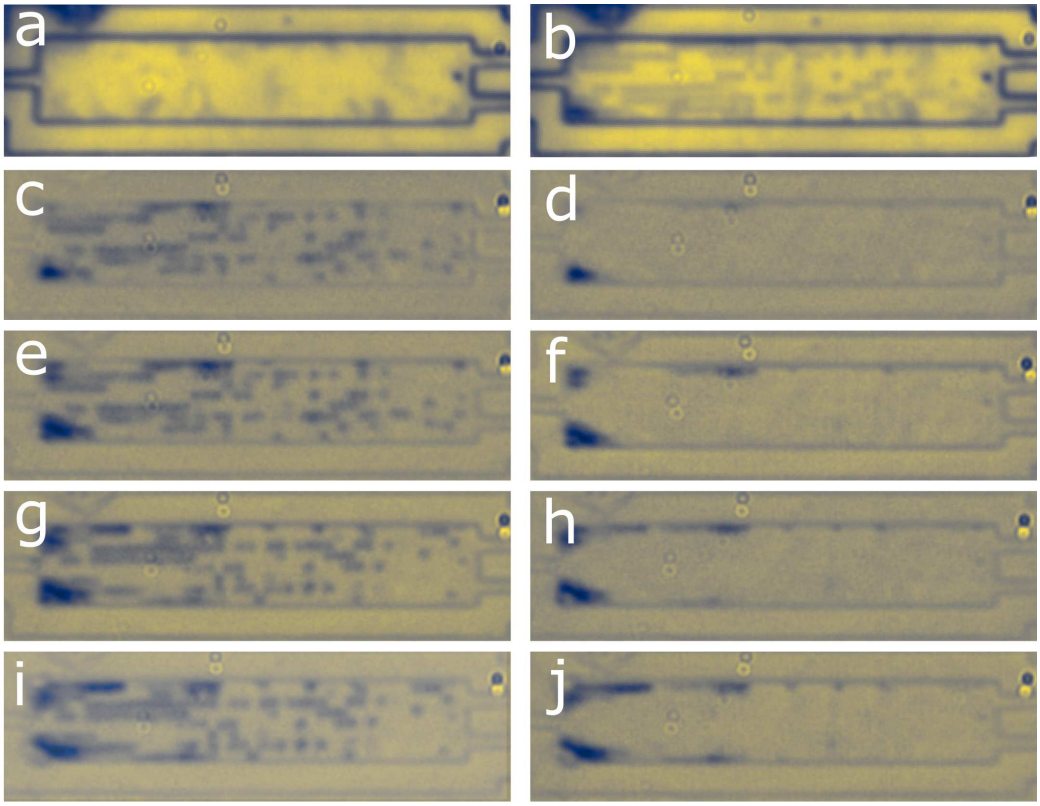

Figure 7.12: (a) Optical images of an MMI before a perturbation pattern was written into a Sb_2Se_3 film. (b) The same MMI with a pixel pattern written into the Sb_2Se_3 film. (c-j) Four successive pattern writes and resets with the final two inverted, pictured using image differencing to isolate any changes between each pattern and the original MMI.

The transmission of the MMI was monitored during this durability test to show any effect on the device performance from the successive patterning. Both outputs were recorded simultaneously and can be seen in figure 7.13. The positions at which the images in 7.12 were taken are shown with the corresponding letter. The first two set and reset cycles (a-e), optimized for the top output, show a high degree of repeatability with the second pattern showing a slightly higher extinction ratio. However, the extinction ratio performance was poor when compared to the previous MMI patterning results. Unlike previous results, the reset was complete with the initial performance

recovered in all cases. For the last two pattern cycles (e-i), the pattern was inverted to optimize transmission for the bottom output. In these cases the extinction ratio was considerably higher than for the previous cases, potentially due to small misalignments between the MMI and the objective used to write the patterns, otherwise a symmetric result would be seen. Figures 7.13 d,f,h,j show the successive changes to the MMI after the reset pulses, where ideally a full reset would be seen (indicated by no change to the image). However the performance was unaffected by the progressive damage seen at the MMI edges due to the lack of light intensity at these points, although if a longer test had been conducted it is likely that this damage would have been propagated into more critical areas of the MMI. These results clearly demonstrate the potential of this work. Being able to guide light towards a selectable output on a single, self-holding device was the original goal of this work and the first demonstration of this has been successfully shown.

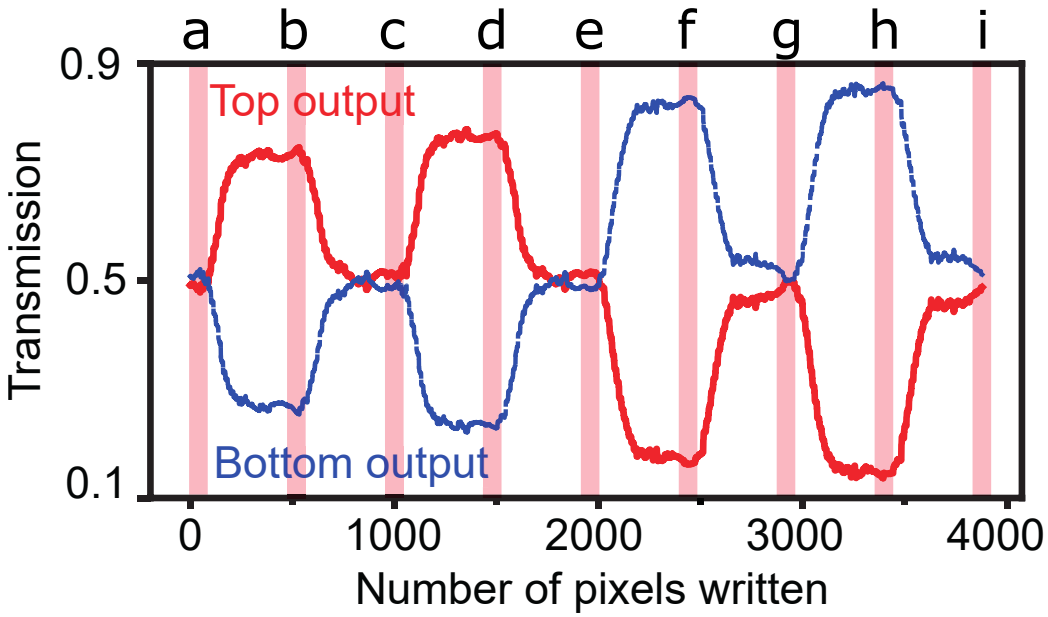

Figure 7.13: Transmission plot for the MMI durability test, where a pattern was written and rewritten twice for both top and bottom port optimizations.

Whilst this work shows the potential of this new perturbation approach paired with Sb_2Se_3 for photonic routing, there are still a number of challenges

to overcome. The most important of these is to demonstrate small-cell electrical switching. If this system is limited to optical switching then it is unlikely to leave the laboratory due to the impracticality of integrating this into a planar device. In this area there is some progress as similar materials are being explored for their electronic memory applications [191, 200]. It appears that minor doping with a metallic element such as tellurium or potassium can greatly affect the resistivity of one or both phases, a useful feature for Joule heating electronic switching. From the results presented here there are obvious improvements that will need to be made. The stability of the experimental setup will need improvement, either with a better controlled environment or by eliminating the drift by mechanical means (e.g. bonding the coupling fibres to the gratings with optical glue). Finally the durability of the phase changing should be studied systematically in a more stable environment to determine where material failure is responsible for the lifetime, and where the degradation is due to a change in fluence caused by external factors. This study should include varying both pulse parameters as a function of phase change cycle in parallel to how GST memory cells are cycled many thousands of times in a "burn in" using a graded pulse scheme to achieve the best stability. Finally a thorough study of the switching speeds and associated energy cost needs to be carried out, as these are some of the most important parameters for an integrated device. In this work the pulse lengths have been used in favor of the fundamental crystallization/amorphization times due to the difficulty of decoupling their optical signals. Electrical switching would enable very accurate optical in-situ measurements of the switching speeds, and provide a basis for testing the whole material family for the optimized stoichiometry/deposition parameters/thicknesses.

Chapter 8

Conclusions and future work

In this thesis, a novel approach of patterning an MMI with an array of rewritable phase change pixels has been combined with a new material family, namely Sb_2S_3 and Sb_2Se_3 to achieve very low-loss, self-holding optical routers. The same properties have also been leveraged to show very low loss phase tuning in an MZI, which does not require a holding voltage in contrast to electro or thermo-optic phase tuners. Both these materials should be explored further by the photonics community. The unparalleled transparency in the c-band wavelength range, coupled with a refractive index difference between their amorphous and crystallization phases enables new types of reconfigurable devices that do not suffer from the high additional losses that are commonly associated with phase change devices, but still maintains the benefit of two stable levels.

This is the first demonstration of their use as reversible phase change materials, with previous work unable to demonstrate reversible phase control. This was achieved after a study of the deposition parameter space, with a sputtering recipe that was optimized for high transparency resulting in a sputtering power of 35 Watts and pressure of 5 mTorr for both materials. The selenium substitution for the sulfur has two key benefits for this work. Firstly, it shifts the bandgap towards higher wavelengths, greatly increasing the practicalities of optical switching using cheaply available diode lasers. Secondly, it lowers the crystallization temperature which, when coupled with the higher absorption for a given wavelength, results in a lower optical power needed for phase switching. This creates a larger fluence window between no phase change and the damage threshold, which proved to hinder the performance of the Sb_2S_3 as it was more sensitive to any change in pump power or spot size. As a result of this the Sb_2Se_3 is more stable over long phase cycling. It is with this in mind that Sb_2Se_3 should be considered the material of choice for integrating with photonic devices such as MZI's and MMI's for

future work. However, as mentioned the Sb_2S_3 has a lower bandgap, just below the visible wavelength range, so should be used in applications where a visible wavelength PCM is sought.

A static testing experiment was built to test the films response to optical stimulus, with a range of pump powers and durations being tested. In combination with ellipsometry results of thermally crystallized samples, the most promising film for photonic applications (a 25 nm thick Sb_2Se_3 film) was identified and a repeatable deposition and encapsulation process found using ZnS:SiO_2. This provided a better capping layer compared to a pure SiO_2 layer by acting as a better barrier to oxidization and delamination. Using straight waveguides on an SOI platform, there were no measurable absorption losses in either phase over the C-band when the waveguide was capped with this material to a thickness of 25 nm thick and up to 750 μm in length. When combined with the thermal stability and glass transition temperature, this material represents the next step in programmable phase change photonics with a change in the real part of refractive index of 0.764 and no measurable absorption at 1550 nm in either phase. Whilst there are other materials with higher index shifts, namely GST and GSST, there are none other than Sb_2S_3 and Sb_2Se_3 that compete with the lack of optical losses which is the limiting factor in using PCM's in larger photonic circuits.

Testing Sb_2Se_3 films over a wide range of pulse powers and lengths showed a highly reversible partial crystallization was achievable, or if the pulse power was increased, a greater but only partially reversible phase change was seen. This was incorporated with current silicon photonic Mach Zehnder Interferometer's to show an impressive reversible 2π phase tuning in a compact footprint (75 μm long), with passive power requirements. Larger phase tuning was also achievable with a 10π phase shift shown using only a 150 μm long device, however this was not fully reversible. Sb_2S_3 was not incorporated into devices due to the difficulty in consistently phase switching the film. If fast electrical switching of Sb_2Se_3 can be demonstrated, then this may displace current phase shifters due to the power and size advantages.

Combining this material with a multimode interference region within a silicon photonic circuit, a pixel perturbation approach was used for on-chip programmable wavefront shaping. A thin film was first sputtered onto the MMI, then pixels of different phases were used to construct a perturbation

pattern. Numerical simulations proved the power of this technique, with a linear optimization scheme used to show very high efficiency arbitrary coupling between any ports on MMIs with multiple input/output ports. This was realized experimentally using precise positioning of a high magnification objective to write pixels of 750 nm^2 into a film. For a device with a single input and two outputs, it was possible to route the light to either of the two output ports with an 8 db extinction ratio between the two ports. Importantly, the total device loss was not increased, and the initial transmission in both ports could be recovered by recrystallizing the entire films. In this way the optical routing is reconfigurable as the same device could be programmed to route light to different outputs using only the reversible phase change film above it. I believe this is the most important result of this work, as optical routing is a challenge at the forefront of photonic design, with this approach solving many of the issues faced by competing techniques, such as power consumption and footprint.

The experimental results agreed with the numerical simulations paving the way for more complex devices in the future with more inputs and outputs. An MMI with three inputs and outputs was simulated, and a perturbation pattern found to route between any input and output with better than -19 dB of cross talk. This provides a clear path to scaling this approach to create routers capable of handling higher port counts. Whilst very encouraging, the approach used for pattern optimization (a discrete linear pixel by pixel simulation) does not scale well with an increased parameter space such as a larger device, smaller perturbation sizes, partial phase change or continuous pixel positions. To fully realize the power of this optical routing technique a faster pattern optimization approach may be needed.

8.1 Outlook

The work shown in this thesis holds a lot of promise towards a phase change photonic future, however there are several issues that need to be addressed before moving forward with complex circuitry. The experimental set up is in need of improvement with more accurate stages, capable of scanning over larger distances, as well as precise temperature control to minimize the

transmission drift that arises from the thermal expansion of the fibre input and output arms. Alternatively a fibre array could be bonded to the surface of the chip to remove this drift. In either case a temperature controlled stage would be important for future applications such as maintaining a phase shift due to the temperature dependence of the silicon waveguides. Stages with a longer travel distances will be particularly important for any tuning applications but will also be necessary as the MMI dimensions are increased to accommodate higher port counts, as this concept is taken beyond the simple case of an MMI with only one input and two outputs.

To move this work beyond pure research I believe that electronically addressable pixels will be required, to enable fully electronic control of the switching. Co-doping with metallic elements may be needed to improve the conductivity, however care must be taken not to compromise the transparency at operation wavelength of the intended device. If electrical switching is achieved then a pre-pattern PCM (to electrically isolate each pixel as its own square), with a common ITO electrode below the film and an insulating cladding between and above the pixels, could lead to a powerful technique for exploring larger devices. If electrical control can be demonstrated, I would like to see larger circuits with many reconfigurable components based on this approach, as a competing technology with the ever increasing thermo-optic MZI meshes that are being proposed as general purpose photonic networks, capable of behaving like an FPGA or neural network.

On the simulation side, there is a lot of potential for improvements, with the linear technique used here a viable solution but probably far from optimal. As the device sizes increase it may be necessary to explore more intelligent optimizations such as using a genetic or swarm algorithm, or training a general small perturbation neural network for this field of photonics. These could also help inform more effective device designs that go beyond the simple case of coating an existing device. The obvious extension would be to try and fabricated waveguides and MMI's directly out of PCM, to greatly enhance the effective index change per unit volume. This could lead to a reduction in size for phase tuners or more efficient routers. Using the film thickness as a parameters, in combination with partial phase change (as has been demonstrated for optical storage) results in a far larger parameter space, again increasing the range of solutions that possible. Thought should also be given to the energy usage, with sparse patterns investigated. Increasing the

effective index shift of each pixel should enable a pattern with significantly fewer pixels, and thus reducing the switching power given the energy per pixel is equivalent..

The switching speeds of these materials should be investigated independently of the applied pulses. It is known from other PCM's that it is possible to tune the switching speeds during the deposition (e.g. by doping), so faster applications such as modulators may require their own unique materials compared to a passive screen, where a slow switching (and therefore low energy cost) are desirable. A comparison should be made between the switching energies for different reconfigurable photonic approaches, both on a per bit basis, as well as the holistic device energy costs. There is likely a great deal of improvement to be made in this direction as it was not the focus of this work.

Whilst current Sb_2S_3 films proved more difficult to work with, they offer the possibility of visible wavelength operation due to it lower absorption edge. This should not be overlooked in favor of Sb_2Se_3's more promising infrared properties if a visible range device is sought to lower circuit footprint or for sensing applications as examples.

Finally, the technique of using a pixel pattern perturbation approach with these novel phase change materials is not limited to the designs presented here, for example photonic crystal cavities could be used with the periodic pillars filled with a PCM, to provide a reconfigurable work space or tunable grating couplers could be written into a waveguide then erased for in-situ testing of circuit components. The applications and uses of these materials are broad and so collaborations should be sought to advance this technology forward in a wide range of applications.

Bibliography

[1] Grand view research Inc. Silicon Photonics Market Size. Technical report, 2016.

[2] Domo. Data Never Sleeps 7.0, 2019.

[3] Richard Brown, Eric Masanet, Bruce Nordman, Arman Shehabi, John Stanley, Dale Sartor, and Peter Chan. Report to Congress on Server and Data Center Energy Efficiency : Public Law 109-431 Environmental Energy Technologies Division Alliance to Save Energy ICF Incorporated. aug 2008.

[4] Sailong Wu, Xin Mu, Lirong Cheng, Simei Mao, and H.Y. Fu. State-of-the-Art and Perspectives on Silicon Waveguide Crossings: A Review. *Micromachines*, 11(3):326, mar 2020.

[5] A. Lugnan, A. Katumba, F. Laporte, M. Freiberger, S. Sackesyn, C. Ma, E. Gooskens, J. Dambre, and P. Bienstman. Photonic neuromorphic information processing and reservoir computing. *APL Photonics*, 5(2):020901, feb 2020.

[6] Azita Emami. Optical interconnects: Design and Analysis. In *Optics InfoBase Conference Papers*, volume Part F40-O, page W4I.1. OSA - The Optical Society, mar 2017.

[7] David Miller. Optical Interconnects. In *Optical Fiber Communication Conference*. OSA, 2010.

[8] Francesco Testa, Stefano Tondini, Fabrizio Gambini, Philippe Velha, Alberto Bianchi, Christophe Kopp, Michael Hofbauer, Costanza Lucia Manganelli, Nikola Zecevic, Stefano Faralli, Gabriel Pares, Reinhard Enne, Aina Serrano, Bernhard Goll, Giorgio Fontana, Astghik Chalyan, Jong Moo Lee, Paolo Pintus, Guido Chiaretti, Horst Zimmermann, Lorenzo Pavesi, Claudio J. Oton, and Stefano Stracca. Integrated reconfigurable silicon photonics switch matrix in IRIS project: Technological achievements and experimental results. *Journal of Lightwave Technology*, 37(2):345–355, jan 2019.

[9] Richard Soref. The Past, Present, and Future of Silicon Photonics. *IEEE Journal of Selected Topics in Quantum Electronics*, 12(6):1678–1687, nov 2006.

[10] Nahum Izhaky, Michael T. Morse, Sean Koehl, Oded Cohen, Doron Rubin, Assia Barkai, Gadi Sarid, Rami Cohen, and Mario J. Paniccia. Development of CMOS-Compatible Integrated Silicon Photonics Devices. *IEEE Journal of Selected Topics in Quantum Electronics*, 12(6): 1688–1698, nov 2006.

[11] Bahram Jalali and Sasan Fathpour. Silicon photonics. *Journal of Lightwave Technology*, 24(12):4600–4615, dec 2006.

[12] C. Dragone, C. A. Edwards, and R. C. Kistler. Integrated Optics N X N Multiplexer on Silicon. *IEEE Photonics Technology Letters*, 3(10): 896–899, oct 1991.

[13] P D Trinh, S. Yegnanarayanan, F. Coppinger, B. Jalali, and Senior Member. Wavelength Multi / Demultiplexer with Extremely Low-Polarization Sensitivity. *IEEE Photonics Technology Letters*, 9(7):940–942, jul 1997.

[14] David A. B. Miller. Attojoule optoelectronics for low-energy information processing and communications. *J. Lightwave Technol.*, 35(3): 346–396, Feb 2017.

[15] David A.B. Miller. Silicon photonics: Meshing optics with applications. *Nature Photonics*, 11(7):403–404, jun 2017.

[16] Benjamin J. Eggleton, Barry Luther-Davies, and Kathleen Richardson. Chalcogenide photonics. *Nature Photonics*, 5(12):725–725, 2011.

[17] M. Wuttig, H. Bhaskaran, and T. Taubner. Phase-change materials for non-volatile photonic applications. *Nature Photonics*, 11(8):465–476, aug 2017.

[18] Kevin J. Miller, Richard F. Haglund, and Sharon M. Weiss. Optical phase change materials in integrated silicon photonic devices: review. *Optical Materials Express*, 8(8):2415, aug 2018.

[19] Fei Ding, Yuanqing Yang, and Sergey I Bozhevolnyi. Dynamic Metasurfaces Using Phase-Change Chalcogenides. *Advanced Optical Materials*, 7(14):1801709, 2019.

[20] J. Feldmann, N. Youngblood, C. D. Wright, H. Bhaskaran, and W. H. P. Pernice. All-optical spiking neurosynaptic networks with self-learning capabilities. *Nature*, 569(7755):208–214, may 2019.

[21] T de Lima, B Shastri, A Tait, M A Nahmias, and P R Prucnal. Progress in neuromorphic photonics. *Nanophotonics*, 6(3):577–599, 2017.

[22] Wim Bogaerts and Abdul Rahim. Programmable Photonics: An Opportunity for an Accessible Large-Volume PIC Ecosystem. *IEEE Journal of Selected Topics in Quantum Electronics*, 26(5), sep 2020.

[23] Daniel Brunner, Alireza Marandi, Wim Bogaerts, and Aydogan Ozcan. Photonics for computing and computing for photonics. *Nanophotonics*, 9(13):4053–4054, oct 2020.

[24] Wim Bogaerts, Daniel Pérez, José Capmany, David A.B. Miller, Joyce Poon, Dirk Englund, Francesco Morichetti, and Andrea Melloni. Programmable photonic circuits. *Nature*, 586(7828):207–216, 2020.

[25] Carlos Garcia-Meca, Sergio Lechago, Antoine Brimont, Amadeu Griol, Sara Mas, Luis Sanchez, Laurent Bellieres, Nuria S Losilla, and Javier Marti. On-chip wireless silicon photonics: from reconfigurable interconnects to lab-on-chip devices. *Light: Science & Applications*, 6(9): e17053–e17053, sep 2017.

[26] G. Dan Hutcheson. Moore's law, lithography, and how optics drive the semiconductor industry. In Nelson M. Felix and Kenneth A. Goldberg, editors, *Extreme Ultraviolet (EUV) Lithography IX*, volume 10583, page 501. SPIE-Intl Soc Optical Eng, mar 2018.

[27] Ran Ding, Yang Liu, Yangjin Ma, Yisu Yang, Qi Li, Andy Eu Jin Lim, Guo Qiang Lo, Keren Bergman, Tom Baehr-Jones, and Michael Hochberg. High-speed silicon modulator with slow-wave electrodes and fully independent differential drive. *Journal of Lightwave Technology*, 32(12):2240–2247, jun 2014.

[28] T. Latchu, M. Pochet, N. G. Usechak, C. DeRose, A. Lentine, D. C. Trotter, and W. Zortman. Power-penalty comparison of push-pull and traveling-wave electrode silicon Mach-Zehnder modulators. In *2014 IEEE Optical Interconnects Conference, OI 2014*, pages 25–26. IEEE Computer Society, 2014.

[29] Tsung Yang Liow, Kah Wee Ang, Qing Fang, Jun Feng Song, Yong Zhong Xiong, Ming Bin Yu, Guo Qiang Lo, and Dim Lee Kwong. Silicon modulators and germanium photodetectors on SOI: Monolithic integration, compatibility, and performance optimization. *IEEE Journal on Selected Topics in Quantum Electronics*, 16(1):307–315, jan 2010.

[30] Po Dong, Long Chen, and Young-kai Chen. High-speed low-voltage single-drive push-pull silicon Mach-Zehnder modulators. *Optics Express*, 20(6):6163, mar 2012.

[31] Ran Ding, Yang Liu, Qi Li, Yisu Yang, Yangjin Ma, Kishore Padmaraju, Andy Eu Jin Lim, Guo Qiang Lo, Keren Bergman, Tom Baehr-Jones, and Michael Hochberg. Design and characterization of a 30-GHz bandwidth low-power silicon traveling-wave modulator. *Optics Communications*, 321:124–133, jun 2014.

[32] Jianfeng Ding, Hongtao Chen, Lin Yang, Lei Zhang, Ruiqiang Ji, Yonghui Tian, Weiwei Zhu, Yangyang Lu, Ping Zhou, and Rui Min. Low-voltage, high-extinction-ratio, Mach-Zehnder silicon optical modulator for CMOS compatible integration. In *2012 Conference on Lasers and Electro-Optics, CLEO 2012*, volume 20, pages 3209–3218. Optical Society of America, jan 2012.

[33] Qiang Xu, Li Chen, Michael G. Wood, Peng Sun, and Ronald M. Reano. Electrically tunable optical polarization rotation on a silicon chip using Berry's phase. *Nature Communications*, 5(1):1–6, nov 2014.

[34] G. T. Reed, G. Mashanovich, F. Y. Gardes, and D. J. Thomson. Silicon optical modulators. *Nature Photonics*, 4(8):518–526, aug 2010.

[35] Zheng Yong, Wesley D. Sacher, Ying Huang, Jared C. Mikkelsen, Yisu Yang, Xianshu Luo, Patrick Dumais, Dominic Goodwill, Hadi Bahrami, Patrick Guo-Qiang Lo, Eric Bernier, and Joyce K. S. Poon.

U-shaped PN junctions for efficient silicon Mach-Zehnder and microring modulators in the O-band. *Optics Express*, 25(7):8425, apr 2017.

[36] Long Chen, Po Dong, and Young Kai Chen. Chirp and dispersion tolerance of a single-drive push-pull silicon modulator at 28 Gb/s. *IEEE Photonics Technology Letters*, 24(11):936–938, jun 2012.

[37] 00BASE-FX Technical Brief, jan 2007.

[38] Michael R. Watts, William A. Zortman, Douglas C. Trotter, Ralph W. Young, and Anthony L. Lentine. Low-voltage, compact, depletion-mode, silicon MachZehnder modulator. *IEEE Journal on Selected Topics in Quantum Electronics*, 16(1):159–164, jan 2010.

[39] Michael R. Watts, William A. Zortman, Douglas C. Trotter, Ralph W. Young, and Anthony L. Lentine. Vertical junction silicon microdisk modulators and switches. *Optics Express*, 19(22):21989, oct 2011.

[40] Erman Timurdogan, Cheryl M. Sorace-Agaskar, Jie Sun, Ehsan Shah Hosseini, Aleksandr Biberman, and Michael R. Watts. An ultralow power athermal silicon modulator. *Nature Communications*, 5(1):1–11, jun 2014.

[41] Xi Xiao, Hao Xu, Xianyao Li, Yingtao Hu, Kang Xiong, Zhiyong Li, Tao Chu, Yude Yu, and Jinzhong Yu. 25 Gbit/s silicon microring modulator based on misalignment-tolerant interleaved PN junctions. *Optics Express*, 20(3):2507, jan 2012.

[42] William A. Zortman, Anthony L. Lentine, Douglas C. Trotter, and Michael R. Watts. Low-voltage differentially-signaled modulators. *Optics Express*, 19(27):26017, dec 2011.

[43] David Patel, Samir Ghosh, Mathieu Chagnon, Alireza Samani, Venkat Veerasubramanian, Mohamed Osman, and David V. Plant. Design, analysis, and transmission system performance of a 41 GHz silicon photonic modulator. *Optics Express*, 23(11):14263, jun 2015.

[44] Hui Yu, Marianna Pantouvaki, Joris Van Campenhout, Dietmar Korn, Katarzyna Komorowska, Pieter Dumon, Yanlu Li, Peter Verheyen, Philippe Absil, Luca Alloatti, David Hillerkuss, Juerg Leuthold, Roel Baets, and Wim Bogaerts. Performance tradeoff between lateral and

interdigitated doping patterns for high speed carrier-depletion based silicon modulators. *Optics Express*, 20(12):12926, jun 2012.

[45] Jianfeng Ding, Ruiqiang Ji, Lei Zhang, and Lin Yang. Electro-optical response analysis of a 40 Gb/s silicon mach-zehnder optical modulator. *Journal of Lightwave Technology*, 31(14):2434–2440, jul 2013.

[46] Matthew Streshinsky, Ran Ding, Yang Liu, Ari Novack, Yisu Yang, Yangjin Ma, Xiaoguang Tu, Edward Koh Sing Chee, Andy Eu-Jin Lim, Patrick Guo-Qiang Lo, Tom Baehr-Jones, and Michael Hochberg. Low power 50 Gb/s silicon traveling wave Mach-Zehnder modulator near 1300 nm. *Optics Express*, 21(25):30350, dec 2013.

[47] Claudio Castellan, Riccardo Franchi, Stefano Biasi, Martino Bernard, Mher Ghulinyan, and Lorenzo Pavesi. Field-Induced Nonlinearities in Silicon Waveguides Embedded in Lateral p-n Junctions. *Frontiers in Physics*, 7:104, jul 2019.

[48] Koen Alexander, John P George, Jochem Verbist, Kristiaan Neyts, Bart Kuyken, Dries Van Thourhout, and Jeroen Beeckman. Nanophotonic Pockels modulators on a silicon nitride platform. *Nature Communications*, 9(1), aug 2018.

[49] Qian Wang, Edward T. F. Rogers, Behrad Gholipour, Chih-Ming Wang, Guanghui Yuan, Jinghua Teng, and Nikolay I. Zheludev. Optically reconfigurable metasurfaces and photonic devices based on phase change materials. *Nature Photonics*, 10(1):60–65, jan 2016.

[50] Alperen Govdeli, Murat Can Sarihan, Utku Karaca, and Serdar Kocaman. Integrated Optical Modulator Based on Transition between Photonic Bands. *Scientific Reports*, 8(1):1–11, dec 2018.

[51] Zhi-Yong Li, Dan-Xia Xu, W. Ross McKinnon, Siegfried Janz, Jens H. Schmid, Pavel Cheben, and Jin-Zhong Yu. Silicon waveguide modulator based on carrier depletion in periodically interleaved PN junctions. *Optics Express*, 17(18):15947, aug 2009.

[52] Hao Xu, Xi Xiao, Xianyao Li, Yingtao Hu, Zhiyong Li, Tao Chu, Yude Yu, and Jinzhong Yu. High speed silicon Mach-Zehnder modulator based on interleaved PN junctions. *Optics Express*, 20(14):15093, jul 2012.

[53] M. Webster, K. Lakshmikumar, C. Appel, C. Muzio, B. Dama, and K. Shastri. Low-power MOS-capacitor based silicon photonic modulators and CMOS drivers. In *Conference on Optical Fiber Communication, Technical Digest Series*, volume 2015-June, page W4H.3. Institute of Electrical and Electronics Engineers Inc., jun 2015.

[54] C. C. Teng. Traveling-wave polymeric optical intensity modulator with more than 40 GHz of 3-dB electrical bandwidth. *Applied Physics Letters*, 60(13):1538–1540, mar 1992. ISSN 00036951. doi: 10.1063/1.107482.

[55] Xiaohui Lin, Tao Ling, Harish Subbaraman, L. Jay Guo, and Ray T. Chen. Printable thermo-optic polymer switches utilizing imprinting and ink-jet printing. *Optics Express*, 21(2):2110, jan 2013. ISSN 1094-4087. doi: 10.1364/oe.21.002110.

[56] Jingdong Luo, Su Huang, Yen Ju Cheng, Tae Dong Kim, Zhengwei Shi, Xing Hua Zhou, and Alex K.Y. Jen. Phenyltetraene-based nonlinear optical chromophores with enhanced chemical stability and electrooptic activity. *Organic Letters*, 9(22):4471–4474, oct 2007. ISSN 15237060. doi: 10.1021/ol701814r.

[57] Yongqiang Shi, Cheng Zhang, Hua Zhang, James H. Bechtel, Larry R. Dalton, Bruce H. Robinson, and William H. Steier. Low (sub-1-volt) halfwave voltage polymeric electro-optic modulators achieved by controlling chromophore shape. *Science*, 288(5463):119–122, apr 2000. ISSN 00368075. doi: 10.1126/science.288.5463.119.

[58] Y. Enami, C. T. Derose, D. Mathine, C. Loychik, C. Greenlee, R. A. Norwood, T. D. Kim, J. Luo, Y. Tian, A. K.Y. Jen, and N. Peyghambarian. Hybrid polymersol-gel waveguide modulators with exceptionally large electro-optic coefficients. *Nature Photonics*, 1(3):180–185, mar 2007. ISSN 17494885. doi: 10.1038/nphoton.2007.25.

[59] Y. Enami, D. Mathine, C. T. Derose, R. A. Norwood, J. Luo, A. K.Y. Jen, and N. Peyghambarian. Hybrid cross-linkable polymer/sol-gel waveguide modulators with 0.65 v half wave voltage at 1550 nm. *Applied Physics Letters*, 91(9):093505, aug 2007. ISSN 00036951. doi: 10.1063/1.2776369.

[60] Larry R. Dalton, Aaron W. Harper, Bo Wu, Rima Ghosn, Joyce Laquindanum, Ziyong Liang, Andrea Hubbel, and Chengzeng Xu. Polymeric Electro-Optic Modulators: Matereials synthesis and processing. *Advanced Materials*, 7(6):519–540, jun 1995. ISSN 0935-9648. doi: 10.1002/adma.19950070603.

[61] Min Cheol Oh, Hua Zhang, Cheng Zhang, Hernan Erlig, Yian Chang, Boris Tsap, Dan Chang, Attila Szep, William H. Steier, Harold R. Fetterman, and Larry R. Dalton. Recent advances in electrooptic polymer modulators incorporating highly nonlinear chromophore. *IEEE Journal on Selected Topics in Quantum Electronics*, 7(5):826–835, sep 2001. ISSN 1077260X. doi: 10.1109/2944.979344.

[62] R. T. Chen. Polymer-based photonic integrated circuits. *Optics and Laser Technology*, 25(6):347–365, dec 1993. ISSN 00303992. doi: 10.1016/0030-3992(93)90001-V.

[63] R. Soref and B. Bennett. Electrooptical effects in silicon. *IEEE Journal of Quantum Electronics*, 23(1):123–129, jan 1987.

[64] R. L. Espinola, M. C. Tsai, James T. Yardley, and R. M. Osgood. Fast and low-power thermooptic switch on thin silicon-on-insulator. *IEEE Photonics Technology Letters*, 15(10):1366–1368, oct 2003.

[65] Nicholas C. Harris, Yangjin Ma, Jacob Mower, Tom Baehr-Jones, Dirk Englund, Michael Hochberg, and Christophe Galland. Efficient, compact and low loss thermo-optic phase shifter in silicon. *Optics Express*, 22(9):10487, may 2014.

[66] Adam Densmore, Siegfried Janz, Rubin Ma, Jens H. Schmid, Dan-Xia Xu, André Delâge, Jean Lapointe, Martin Vachon, and Pavel Cheben. Compact and low power thermo-optic switch using folded silicon waveguides. *Optics Express*, 17(13):10457, jun 2009.

[67] Po Dong, Wei Qian, Hong Liang, Roshanak Shafiiha, Dazeng Feng, Guoliang Li, John E. Cunningham, Ashok V. Krishnamoorthy, and Mehdi Asghari. Thermally tunable silicon racetrack resonators with ultralow tuning power. *Optics Express*, 18(19):20298, sep 2010.

[68] Hooman Abediasl and Hossein Hashemi. Monolithic optical phased-array transceiver in a standard SOI CMOS process. *Optics Express*, 23 (5):6509, mar 2015.

[69] Kyle Murray, Zeqin Lu, Hasitha Jayatilleka, and Lukas Chrostowski. Dense dissimilar waveguide routing for highly efficient thermo-optic switches on silicon. *Optics Express*, 23(15):19575, jul 2015.

[70] Milos Nedeljkovic, Stevan Stanković, Colin J. Mitchell, Ali Z. Khokhar, Scott A. Reynolds, David J. Thomson, Frederic Y. Gardes, Callum G. Littlejohns, Graham T. Reed, and Goran Z. Mashanovich. Mid-infrared thermo-optic modulators in SoI. *IEEE Photonics Technology Letters*, 26(13):1352–1355, jul 2014.

[71] M. W. Geis, S. J. Spector, R. C. Williamson, and T. M. Lyszczarz. Submicrosecond submilliwatt silicon-on-insulator thermooptic switch. *IEEE Photonics Technology Letters*, 16(11):2514–2516, nov 2004.

[72] Peng Sun and Ronald M. Reano. Submilliwatt thermo-optic switches using free-standing silicon-on-insulator strip waveguides. *Optics Express*, 18(8):8406, apr 2010.

[73] Lanlan Gu, Wei Jiang, Xiaonan Chen, and Ray T. Chen. Thermooptically tuned photonic crystal waveguide silicon-on-insulator Mach-Zehnder interferometers. *IEEE Photonics Technology Letters*, 19(5): 342–344, mar 2007.

[74] Michael R. Watts, Jie Sun, Christopher DeRose, Douglas C. Trotter, Ralph W. Young, and Gregory N. Nielson. Adiabatic thermo-optic Mach–Zehnder switch. *Optics Letters*, 38(5):733, mar 2013.

[75] Y. Hashizume, S. Katayose, T. Tsuchizawa, T. Watanabe, and M. Itoh. Low-power silicon thermo-optic switch with folded waveguide arms and suspended ridge structures. *Electronics Letters*, 48(19):1234–1235, sep 2012.

[76] Qing Fang, Jun Feng Song, Tsung Yang Liow, Hong Cai, Ming Bin Yu, Guo Qiang Lo, and Dim Lee Kwong. Ultralow power silicon photonics thermo-optic switch with suspended phase arms. *IEEE Photonics Technology Letters*, 23(8):525–527, apr 2011.

[77] Jinsong Xia. Thermo-optic variable optical attenuator with low power consumption fabricated on silicon-on-insulator by anisotropic chemical etching. *Optical Engineering*, 43(4):789, apr 2004.

[78] Yuya Shoji, Kenji Kintaka, Satoshi Suda, Hitoshi Kawashima, Toshifumi Hasama, and Hiroshi Ishikawa. Low-crosstalk 2×2 thermo-optic switch with silicon wire waveguides. *Optics Express*, 18(9):9071, apr 2010.

[79] Marcel W. Pruessner, Todd H. Stievater, Mike S. Ferraro, and William S. Rabinovich. Thermo-optic tuning and switching in SOI waveguide Fabry-Perot microcavities. *Optics Express*, 15(12):7557, jun 2007.

[80] Reza Fatemi, Aroutin Khachaturian, and Ali Hajimiri. A Nonuniform Sparse 2-D Large-FOV Optical Phased Array With a Low-Power PWM Drive. *IEEE Journal of Solid-State Circuits*, 54(5):1200–1215, may 2019.

[81] Jie Sun, Erman Timurdogan, Ami Yaacobi, Ehsan Shah Hosseini, and Michael R. Watts. Large-scale nanophotonic phased array. *Nature*, 493 (7431):195–199, jan 2013.

[82] Jie Sun, Erman Timurdogan, Ami Yaacobi, Zhan Su, Ehsan Shah Hosseini, David B. Cole, and Michael R. Watts. Large-scale silicon photonic circuits for optical phased arrays. *IEEE Journal on Selected Topics in Quantum Electronics*, 20(4), jul 2014.

[83] SungWon Chung, Makoto Nakai, and Hossein Hashemi. Low-power thermo-optic silicon modulator for large-scale photonic integrated systems. *Optics Express*, 27(9):13430, apr 2019.

[84] Niels Quack, Hamed Sattari, Alain Yuji Takabayashi, Yu Zhang, Peter Verheyen, Wim Bogaerts, Pierre Edinger, Carlos Errando-Herranz, and Kristinn B. Gylfason. MEMS-Enabled Silicon Photonic Integrated Devices and Circuits. *IEEE Journal of Quantum Electronics*, 56(1), feb 2020.

[85] Zengguang Cheng, Carlos Ríos, Nathan Youngblood, C. David Wright, Wolfram H.P. Pernice, and Harish Bhaskaran. Device-Level Photonic

Memories and Logic Applications Using Phase-Change Materials. *Advanced Materials*, 30(32), aug 2018.

[86] Sangyoon Han, Tae Joon Seok, Niels Quack, Byung-Wook Yoo, and Ming C. Wu. Large-scale silicon photonic switches with movable directional couplers. *Optica*, 2(4):370, apr 2015.

[87] Tae Joon Seok, Niels Quack, Sangyoon Han, Richard S. Muller, and Ming C. Wu. Large-scale broadband digital silicon photonic switches with vertical adiabatic couplers. *Optica*, 3(1):64, jan 2016.

[88] Tae Joon Seok, Kyungmok Kwon, Johannes Henriksson, Jianheng Luo, and Ming C. Wu. Wafer-scale silicon photonic switches beyond die size limit. *Optica*, 6(4):490, apr 2019.

[89] Franck Chollet. Devices based on co-integrated MEMS actuators and optical waveguide: A review. *Micromachines*, 7(2):18, jan 2016.

[90] D. T. Fuchs, H. B. Chan, H. R. Stuart, F. Baumann, D. Greywall, M. E. Simon, and A. Wong-Foy. Monolithic integration of MEMS-based phase shifters and optical waveguides in silicon-on-insulator. *Electronics Letters*, 40(2):142–143, jan 2004.

[91] Tianran Liu, Francesco Pagliano, and Andrea Fiore. Nano-opto-electro-mechanical switch based on a four-waveguide directional coupler. *Optics Express*, 25(9):10166, may 2017.

[92] W. C. L. Hopman, K. O. van der Werf, A. J. F. Hollink, W. Bogaerts, V. Subramaniam, and R. M. de Ridder. Nano-mechanical tuning and imaging of a photonic crystal micro-cavity resonance. *Optics Express*, 14(19):8745, sep 2006.

[93] Marcel W. Pruessner, Doweon Park, Todd H. Stievater, Dmitry A. Kozak, and William S. Rabinovich. Broadband opto-electro-mechanical effective refractive index tuning on a chip. *Optics Express*, 24(13): 13917, jun 2016.

[94] T. A. Strasser and J. L. Wagener. Wavelength-selective switches for ROADM applications. *IEEE Journal on Selected Topics in Quantum Electronics*, 16(5):1150–1157, sep 2010.

[95] José Capmany, Ivana Gasulla, and Daniel Pérez. Microwave photonics: The programmable processor. 10(1):6–8, jan 2016.

[96] Yuta Akihama and Kazuhiro Hane. Single and multiple optical switches that use freestanding silicon nanowire waveguide couplers. *Light: Science and Applications*, 1:e16, jun 2012.

[97] Haining Yang, Brian Robertson, Peter Wilkinson, and Daping Chu. Low-cost CDC ROADM architecture based on stacked wavelength selective switches. *Journal of Optical Communications and Networking*, 9(5):375–384, may 2017.

[98] J. J. Ackert, J. K. Doylend, D. F. Logan, P. E. Jessop, R. Vafaei, L. Chrostowski, and A. P. Knights. Defect-mediated resonance shift of silicon-on-insulator racetrack resonators. *Opt. Express*, 19(13):11969–11976, jun 2011.

[99] Milan M. Milosevic, Xia Chen, Wei Cao, Antoine F.J. Runge, Yohann Franz, Callum G. Littlejohns, Sakellaris Mailis, Anna C. Peacock, David J. Thomson, and Graham T. Reed. Ion Implantation in Silicon for Trimming the Operating Wavelength of Ring Resonators. *IEEE Journal of Selected Topics in Quantum Electronics*, 24(4), jul 2018.

[100] Milan M Milosevic, Xia Chen, Xingshi Yu, Nicholas J Dinsdale, Ozan Aktas, Swe Zin Oo, Ali Z Khokhar, David J Thomson, Otto L Muskens, Harold M H Chong, Anna C Peacock, Shinichi Saito, Graham T Reed, M M Milosevic, X Chen, X Yu, O Aktas, A Z Khokhar, D J Thomson, A C Peacock, G T Reed, H M H Chong, and S Saito. Ion Implantation of Germanium Into Silicon for Critical Coupling Control of Racetrack Resonators. *Journal of Lightwave Technology*, 38(7), jan 2020.

[101] Hanyu Zhang, Linjie Zhou, Liangjun Lu, Zhanzhi Guo, Jian Xu, Xuecheng Fu, Jianping Chen, and B. M. A. Rahman. Electro-optical switch using ge2sb2te5 phase-change material in a silicon mzi structure. In *2017 Conference on Lasers and Electro-Optics Pacific Rim*, page s1972. Optical Society of America, 2017.

[102] B. T. Kolomiets. Vitreous Semiconductors (II). *physica status solidi (b)*, 7(3):713–731, 1964.

[103] G M Graham, A C Hollis Hallett, and Stanford R Ovshinsky. Reversible electrical switching phenomena in disordered structures. *Phys. Rev. Phys. Rev. J. Phys. Soc. Japan G. J. Vander Berg J. Kondo, Progr. Theoret. Phys. Phys. Rev*, 21965(153):1473–979, 1967.

[104] Alexander V Kolobov and Junji Tominaga. *Chalcogenides Metastability and Phase Change Phenomena*. Springer, 2012.

[105] Lei Wang, Si-Di Gong, Jing Wen, and Ci Hui Yang. An Improved Electrical Switching and Phase-Transition Model for Scanning Probe Phase-Change Memory. *Journal of Nanomaterials*, 2016:1–5, mar 2016.

[106] Mark D. Mackenzie, James M. Morris, Christian R. Petersen, Andrea Ravagli, Chris Craig, Daniel W. Hewak, Henry T. Bookey, Ole Bang, and Ajoy K. Kar. GLS and GLSSe ultrafast laser inscribed waveguides for mid-IR supercontinuum generation. *Optical Materials Express*, 9 (2):643, feb 2019.

[107] Xuan Li, Nathan Youngblood, C. David Wright, Wolfram H. P. Pernice, and Harish Bhaskaran. Non-volatile silicon photonic memory with more than 4-bit per cell capability. apr 2019.

[108] Carlos Rios, Peiman Hosseini, C. David Wright, Harish Bhaskaran, and Wolfram H.P. Pernice. On-chip photonic memory elements employing phase-change materials. *Advanced Materials*, 26(9):1372–1377, mar 2014.

[109] Q. Wang, J. Maddock, E. T F Rogers, T. Roy, C. Craig, K. F. MacDonald, D. W. Hewak, and N. I. Zheludev. 1.7 Gbit/ in 2 gray-scale continuous-phase-change femtosecond image storage. *Applied Physics Letters*, 104(12):16–19, 2014.

[110] Wolfram H P Pernice and Harish Bhaskaran. Photonic non-volatile memories using phase change materials. *Applied Physics Letters*, 101 (17):1–6, 2012.

[111] Sajjad Abdollahramezani, Omid Hemmatyar, Hossein Taghinejad, Alex Krasnok, Yashar Kiarashinejad, Mohammadreza Zandehshahvar, Andrea Alu, and Ali Adibi. Tunable nanophotonics enabled by chalcogenide phase-change materials. *Nanophotonics*, 9(5), jan 2020.

[112] M Wuttig. Phase-change materials: towards a universal memory? *Nat. Mater.*, 4:265–266, apr 2005.

[113] Simone Raoux, Feng Xiong, Matthias Wuttig, and Eric Pop. Phase change materials and phase change memory. *MRS Bulletin*, 39(08): 703–710, aug 2014.

[114] Carlos Rios, Matthias Stegmaier, Peiman Hosseini, Di Wang, Torsten Scherer, C. David Wright, Harish Bhaskaran, and Wolfram H.P. Pernice. Integrated all-photonic non-volatile multi-level memory. *Nature Photonics*, 9(11):725–732, 2015.

[115] N Yamada M Wuttig. Phase-change materials for rewriteable data storage. *Nat. Mater.*, 6:824–832, nov 2007.

[116] S Raoux. Phase Change Materials. *Annual Review of Materials Research*, 39:25–48, 2009.

[117] Eiichi Kuramochi and Masaya Notomi. Optical memory: Phase-change memory. *Nature Photonics*, 9(11):712–714, oct 2015.

[118] Miquel Rudé, Josselin Pello, Robert E. Simpson, Johann Osmond, Gunther Roelkens, Jos J.G.M. Van Der Tol, and Valerio Pruneri. Optical switching at 1.55 μm in silicon racetrack resonators using phase change materials. *Applied Physics Letters*, 103(14), 2013.

[119] Hiroyuki Tsuda. Ultra-compact optical switch using phase-change material. *2010 Asia Communications and Photonics Conference and Exhibition, ACP 2010*, (1):540–541, 2010.

[120] Zhaojian Zhang, Junbo Yang, Wei Bai, Yunxin Han, Xin He, Jie Huang, Dingbo Chen, Siyu Xu, and Wanlin Xie. All-optical switch and logic gates based on hybrid silicon-Ge2Sb2Te5 metasurfaces . *Applied Optics*, 58(27):7392, sep 2019.

[121] Kentaro Kato, Masashi Kuwahara, Hitoshi Kawashima, Tohru Tsuruoka, and Hiroyuki Tsuda. Current-driven phase-change optical gate switch using indium-tin-oxide heater. *Applied Physics Express*, 10(7): 072201, jul 2017.

[122] Hanyu Zhang, Linjie Zhou, Jian Xu, Ningning Wang, Hao Hu, Liangjun Lu, B.M.A. Rahman, and Jianping Chen. Nonvolatile waveguide transmission tuning with electrically-driven ultra-small GST phase-change material. *Science Bulletin*, 64(11):782–789, jun 2019.

[123] Tatsuya Toyosaki, Daiki Tanaka, Yuya Shoji, Masashi Kuwahara, and Xiaomin Wang. Reversible Switching of an Optical Gate Based on Si Rib Waveguides with a Ge2Sb2Te5 Thin Film. *2011 1st International Symposium on Access Spaces (ISAS) IEEE*, 7943(c):1–8, 2011.

[124] Daiki Tanaka, Yuya Shoji, Masashi Kuwahara, Xiaomin Wang, Kenji Kintaka, Hitoshi Kawashima, Tatsuya Toyosaki, Yuichiro Ikuma, and Hiroyuki Tsuda. Ultra-small, self-holding, optical gate switch using Ge2Sb2Te5 with a multi-mode Si waveguide. *Opt. Express*, 20(9): 10283–10294, apr 2012.

[125] Y. Ikuma, Y. Shoji, M. Kuwahara, X. Wang, K. Kintaka, H. Kawashima, D. Tanaka, and H. Tsuda. Small-sized optical gate switch using Ge2Sb2Te5 phase-change material integrated with silicon waveguide. *Electronics Letters*, 46(5):1–2, apr 2010.

[126] Takumi Moriyama, Daiki Tanaka, Paridhi Jain, Hitoshi Kawashima, Masashi Kuwahara, Xiaomin Wang, and Hiroyuki Tsuda. Ultra-compact, self-holding asymmetric Mach-Zehnder interferometer switch using Ge2Sb2Te5 phase-change material. *IEICE Electronics Express*, 11(15), jul 2014.

[127] Peipeng Xu, Jiajiu Zheng, Jonathan K. Doylend, and Arka Majumdar. Low-Loss and Broadband Nonvolatile Phase-Change Directional Coupler Switches. *ACS Photonics*, 6(2):553–557, feb 2019.

[128] Ann-Katrin U. Michel, Peter Zalden, Dmitry N. Chigrin, Matthias Wuttig, Aaron M. Lindenberg, and Thomas Taubner. Reversible optical switching of infrared antenna resonances with ultrathin phase-change layers using femtosecond laser pulses. *ACS Photonics*, 1(9): 833–839, aug 2014.

[129] Miquel Rudé, Vahagn Mkhitaryan, Arif Engin Cetin, Timothy Alan Miller, Albert Carrilero, Simon Wall, Francisco Javier García de Abajo, Hatice Altug, and Valerio Pruneri. Ultrafast and Broadband Tuning

of Resonant Optical Nanostructures Using Phase-Change Materials. *Advanced Optical Materials*, 4(7):1060–1066, jul 2016.

[130] Carlota Ruiz de Galarreta, Arseny M. Alexeev, Yat Yin Au, Martin Lopez-Garcia, Maciej Klemm, Martin Cryan, Jacopo Bertolotti, and C. David Wright. Nonvolatile Reconfigurable Phase-Change Metadevices for Beam Steering in the Near Infrared. *Advanced Functional Materials*, 28(10), mar 2018.

[131] Indranil Chakraborty, Gobinda Saha, and Kaushik Roy. Photonic In-Memory Computing Primitive for Spiking Neural Networks Using Phase-Change Materials. *Phys. Rev. Appl.*, 11:14063, 2019.

[132] Behrad Gholipour, Jianfa Zhang, Kevin F. MacDonald, Daniel W. Hewak, and Nikolay I. Zheludev. An all-optical, non-volatile, bidirectional, phase-change meta-switch. *Advanced Materials*, 25(22):3050–3054, jun 2013.

[133] Weiling Dong, Yimei Qiu, Xilin Zhou, Agnieszka Banas, Krzysztof Banas, Mark B.H. Breese, Tun Cao, and Robert E. Simpson. Tunable Mid-Infrared Phase-Change Metasurface. *Advanced Optical Materials*, 6(14), jul 2018.

[134] Q Wang, R Rogers, B Gholipour, C Wang, G Yuan, J Teng, and N Zheludev. Optically reconfigurable metasurfaces and photonic devices based on phase change materials. *Nat. Photon.*, 10:60–65, dec .

[135] D Strand, DV Tsu, and R Miller. Optical Routers Based on Ovonic Phase Change Materials. *Proceedngs of E*PCOS 06*, pages 1–8, 2006.

[136] Yuichiro Ikuma, Toshiharu Saiki, and Hiroyuki Tsuda. Proposal of a small self-holding 2×2 optical switch using phase-change material. *IEICE Electronics Express*, 5(12):442–445, june 2008.

[137] Nadir Ali and Rajesh Kumar. Mid-infrared non-volatile silicon photonic switches using Ge2Sb2Te5 embedded in SOI waveguide. *Nanotechnology*, 31(11), dec 2019.

[138] Richard Soref, Joshua Hendrickson, Haibo Liang, Arka Majumdar, Jianwei Mu, Xun Li, and Wei-Ping Huang. Electro-optical switching

at 1550 nm using a two-state GeSe phase-change layer. *Optics Express*, 23(2):1536, jan 2015.

[139] Hiroyuki Tsuda, Daiki Tanaka, Tatsuya Toyosaki, Yuichiro Ikuma, Yuya Shoji, Masashi Kuwahara, Xiaomin Wang, Kenji Kintaka, and Hitoshi Kawashima. Small-Sized Self-Holding Optical Switch Using Phase-Change Material. *2011 13th International Conference on Transparent Optical Networks IEEE*, 1(1):4–7, jun 2011.

[140] Carlos Ríos, Nathan Youngblood, Zengguang Cheng, Manuel Le Gallo, Wolfram H P Pernice, David Wright, Abu Sebastian, and Harish Bhaskaran. In-memory computing on a photonic platform.

[141] Yat Yin Au, Harish Bhaskaran, and C. David Wright. Phase-change devices for simultaneous optical-electrical applications. *Scientific Reports*, 7(1), dec 2017.

[142] Qihang Zhang, Yifei Zhang, Junying Li, Richard Soref, Tian Gu, and Juejun Hu. Broadband nonvolatile photonic switching based on optical phase change materials: beyond the classical figure-of-merit. *Optics Letters*, 43(1):94, jan 2018.

[143] Yifei Zhang, Jeffrey B. Chou, Junying Li, Huashan Li, Qingyang Du, Anupama Yadav, Si Zhou, Mikhail Y. Shalaginov, Zhuoran Fang, Huikai Zhong, Christopher Roberts, Paul Robinson, Bridget Bohlin, Carlos Ríos, Hongtao Lin, Myungkoo Kang, Tian Gu, Jamie Warner, Vladimir Liberman, Kathleen Richardson, and Juejun Hu. Broadband transparent optical phase change materials for high-performance nonvolatile photonics. *Nature Communications*, 10(1), dec 2019.

[144] Hyun Tak Kim, Bong Jun Kim, Sungyoul Choi, Byung Gyu Chae, Yong Wook Lee, T. Driscoll, M. M. Qazilbash, and D. N. Basov. Electrical oscillations induced by the metal-insulator transition in VO2. *Journal of Applied Physics*, 107(2):023702, jan 2010.

[145] F. J. Morin. Oxides which show a metal-to-insulator transition at the neel temperature. *Physical Review Letters*, 3(1):34–36, jul 1959.

[146] Shuai Yang, Mohammad Vaseem, and Atif Shamim. Fully Inkjet-Printed VO2-Based Radio-Frequency Switches for Flexible Reconfig-

urable Components. *Advanced Materials Technologies*, 4(1):1800276, jan 2019.

[147] Burak Gerislioglu, Arash Ahmadivand, Mustafa Karabiyik, Raju Sinha, and Nezih Pala. VO2-Based Reconfigurable Antenna Platform with Addressable Microheater Matrix. *Advanced Electronic Materials*, 3(9):1700170, sep 2017.

[148] Chenghao Wan, Zhen Zhang, David Woolf, Colin M. Hessel, Jura Rensberg, Joel M. Hensley, Yuzhe Xiao, Alireza Shahsafi, Jad Salman, Steffen Richter, Yifei Sun, M. Mumtaz Qazilbash, Rüdiger Schmidt-Grund, Carsten Ronning, Shriram Ramanathan, and Mikhail A. Kats. On the Optical Properties of Thin-Film Vanadium Dioxide from the Visible to the Far Infrared. *Annalen der Physik*, 531(10):1900188, oct 2019.

[149] Marc Currie, Michael A Mastro, and Virginia D Wheeler. Characterizing the tunable refractive index of vanadium dioxide. *Optical Materials Express*, 7(5):1697, apr 2017.

[150] Mohsen Jafari and Mina Rais-Zadeh. Zero-static-power phase-change optical modulator. *Optics Letters*, 41(6):1177, mar 2016.

[151] Mohsen Jafari and Mina Rais-Zadeh. An ultra-high contrast optical modulator with 30 dB isolation at 1.55 µm with 25 THz bandwidth. In Shizhuo Yin and Ruyan Guo, editors, *Photonic Fiber and Crystal Devices: Advances in Materials and Innovations in Device Applications XI*, volume 10382, page 38. SPIE, aug 2017.

[152] Ping Xie Ping Xie, Bin Li Bin Li, Suying Zhang Suying Zhang, and Dingquan Liu, and Dingquan Liu. Using lead germanium telluride as a high-index coating material in the mid-wavelength infrared narrow bandpass filters. *Chinese Optics Letters*, 13(12):123101–123104, dec 2015.

[153] Mohsen Jafari, L. Jay Guo, and Mina Rais-Zadeh. RGB tunable color filters using germanium telluride. In Ganapathi S. Subramania and Stavroula Foteinopoulou, editors, *Active Photonic Platforms X*, volume 10721, page 16. SPIE-Intl Soc Optical Eng, sep 2018.

[154] Julian Pries, Yuan Yu, Peter Kerres, Maria Häser, Simon Steinberg, Fabian Gladisch, Shuai Wei, Pierre Lucas, and Matthias Wuttig. Approaching the Glass Transition Temperature of GeTe by Crystallizing Ge 15 Te 85. *physica status solidi (RRL) – Rapid Research Letters*, page pssr.202000478, nov 2020.

[155] W. M. Yim, E. V. Fitzke, and F. D. Rosi. Thermoelectric properties of Bi2Te3-Sb2Te3-Sb2Se3 pseudo-ternary alloys in the temperature range 77 to 300 K. *Journal of Materials Science*, 1(1):52–65, feb 1966.

[156] Ying Zhou, Liang Wang, Shiyou Chen, Sikai Qin, Xinsheng Liu, Jie Chen, Ding Jiang Xue, Miao Luo, Yuanzhi Cao, Yibing Cheng, Edward H. Sargent, and Jiang Tang. Thin-film Sb2Se3 photovoltaics with oriented one-dimensional ribbons and benign grain boundaries. *Nature Photonics*, 9(6):409–415, jun 2015.

[157] Ying Zhou, Meiying Leng, Zhe Xia, Jie Zhong, Huaibing Song, Xinsheng Liu, Bo Yang, Junpei Zhang, Jie Chen, Kunhao Zhou, Junbo Han, Yibing Cheng, and Jiang Tang. Solution-Processed Antimony Selenide Heterojunction Solar Cells. *Advanced Energy Materials*, 4(8): 1301846, jun 2014.

[158] Xinsheng Liu, Jie Chen, Miao Luo, Meiying Leng, Zhe Xia, Ying Zhou, Sikai Qin, Ding Jiang Xue, Lu Lv, Han Huang, Dongmei Niu, and Jiang Tang. Thermal evaporation and characterization of Sb2Se3 thin film for substrate Sb2Se3/CdS solar cells. *ACS Applied Materials and Interfaces*, 6(13):10687–10695, jul 2014.

[159] Liang Wang, Deng Bing Li, Kanghua Li, Chao Chen, Hui Xiong Deng, Liang Gao, Yang Zhao, Fan Jiang, Luying Li, Feng Huang, Yisu He, Haisheng Song, Guangda Niu, and Jiang Tang. Stable 6%-efficient Sb2Se3 solar cells with a ZnO buffer layer. *Nature Energy*, 2(4):17046, mar 2017.

[160] A Shongalova, M R Correia, J P Teixeira, J P Leito, J C Gonzlez, S Ranjbar, S Garud, B Vermang, J M V Cunha, P M P Salom, and P A Fernandes. Growth of Sb2Se3 thin films by selenization of RF sputtered binary precursors. *Solar Energy Materials and Solar Cells*, 187:219–226, dec 2018.

[161] Chao Chen, David C. Bobela, Ye Yang, Shuaicheng Lu, Kai Zeng, Cong Ge, Bo Yang, Liang Gao, Yang Zhao, Matthew C. Beard, and Jiang Tang. Characterization of basic physical properties of Sb2Se3 and its relevance for photovoltaics. *Frontiers of Optoelectronics*, 10(1):18–30, mar 2017.

[162] P Arun, A G Vedeshwar, and N C Mehra. Laser-induced crystallization in Sb2S3 films. *Materials Research Bulletin*, 32(7):907–913, jul 1997.

[163] P. Arun and A. G. Vedeshwar. Potential of Sb2Se3 films for photothermal phase change optical storage. *Thin Solid Films*, 335(1-2):270–278, nov 1998.

[164] P. Arun, A. G. Vedeshwar, and N. C. Mehra. Laser-induced crystallization in amorphous films of Sb2C3 (C = S, Se, Te), potential optical storage media. *Journal of Physics D: Applied Physics*, 32(3):183–190, feb 1999.

[165] P. Arun and A.G. Vedeshwar. Effect of heat treatment on the optical properties of amorphous Sb2S3 film: The possibility of optical storage. *Journal of Non-Crystalline Solids*, 220(1):63–68, oct 1997.

[166] Weiling Dong, Hailong Liu, Jitendra K Behera, Li Lu, Ray J H Ng, Kandammathe Valiyaveedu Sreekanth, Xilin Zhou, Joel K W Yang, and Robert E Simpson. Wide band gap phase change material tuned visible photonics. Technical report, 2018.

[167] N. Shylashree, B. V. Uma, S. Dhanush, Sagar Abachi, A. Nisarga, K. Aashith, and B. G. Sangeetha. Preparation and characterization of Sb2Se3 devices for memory applications. In *AIP Conference Proceedings*, volume 1966, page 020032. American Institute of Physics Inc., may 2018.

[168] Roman Bruck, Kevin Vynck, Philippe Lalanne, Ben Mills, David J Thomson, Goran Z Mashanovich, Graham T Reed, and Otto L Muskens. An all-optical spatial light modulator for field-programmable silicon photonic circuits. *Optica*, 3(4):396–402, 2016.

[169] K. S. Chiang. Analysis of optical fibers by the effective-index method. *Appl. Opt.*, 25(3):348–354, Feb 1986. doi: 10.1364/AO.25.000348. URL `http://ao.osa.org/abstract.cfm?URI=ao-25-3-348`.

[170] Lucas B Soldano and Erik C M Pennings. Optical Multi-Mode Interference Devices Based on Self-Imaging : Principles and Applications. *Journal of Lightwave Technology*, 13(4), 1995.

[171] J.E. Zucker, K.L. Jones, T.H. Chiu, B. Tell, and K. Brown-Goebeler. Strained quantum wells for polarization-independent electrooptic waveguide switches. *Journal of Lightwave Technology*, 10(12): 1926–1930, dec 1992.

[172] R.J. Deri, E.C.M. Pennings, A. Scherer, A.S. Gozdz, C. Caneau, N.C. Andreadakis, V. Shah, L. Curtis, R.J. Hawkins, J.B.D. Soole, and J.-I. Song. Ultracompact monolithic integration of balanced, polarization diversity photodetectors for coherent lightwave receivers. *IEEE Photonics Technology Letters*, 4(11):1238–1240, nov 1992.

[173] R. van Roijen, E. C. M. Pennings, M. J. N. van Stalen, T. van Dongen, B. H. Verbeek, and J. M. M. van der Heijden. Compact InP-based ring lasers employing multimode interference couplers and combiners. *Applied Physics Letters*, 64(14):1753–1755, apr 1994.

[174] Yingjie Liu, Zhiyu Li, Shuai Wang, Nan Zhang, Yong Yao, Jiangbing Du, Zuyuan He, Qinghai Song, and Ke Xu. Ultra-compact and polarization-insensitive MMI coupler based on inverse design. In *2019 Optical Fiber Communications Conference and Exhibition (OFC)*, pages 1–3, 2019.

[175] Olof Bryngdahl. Image formation using self-imaging techniques. *J. Opt. Soc. Am.*, 63(4):416–419, apr 1973.

[176] Letian Wang, Matthew Eliceiri, Yang Deng, Yoonsoo Rho, Wan Shou, Heng Pan, Jie Yao, and Costas P. Grigoropoulos. Fast Reversible Phase Change Silicon for Visible Active Photonics. *Advanced Functional Materials*, 30(17), apr 2020.

[177] Christian Lang, Se Ahn Song, Duc Nguyen Manh, and David J.H. Cockayne. Building blocks of amorphous Ge2 Sb2 Te5. *Physical Review B - Condensed Matter and Materials Physics*, 76(5):054101, aug 2007.

[178] Juarez L.F. Da Silva, Aron Walsh, Su Huai Wei, and Hosun Lee. Atomistic origins of the phase transition mechanism in Ge 2Sb2Te5. *Journal of Applied Physics*, 106(11):113509, dec 2009.

[179] Dominic Lencer, Martin Salinga, and Matthias Wuttig. Design rules for phase-change materials in data storage applications. *Advanced Materials*, 23(18):2030–2058, may 2011.

[180] J. Akola and R. O. Jones. Structural phase transitions on the nanoscale: The crucial pattern in the phase-change materials Ge2 Sb2 Te5 and GeTe. *Physical Review B - Condensed Matter and Materials Physics*, 76(23):235201, dec 2007.

[181] Noboru Yamada, Eiji Ohno, Kenichi Nishiuchi, Nobuo Akahira, and Masatoshi Takao. Rapid-phase transitions of GeTe-Sb 2 Te 3 pseudobinary amorphous thin films for an optical disk memory. *Journal of Applied Physics*, 69(5):2849, jun 1991.

[182] Alexander V Kolobov, Paul Fons, Anatoly I Frenkel, Alexei L Ankudinov, Junji Tominaga, and Tomoya Uruga. Understanding the phase-change mechanism of rewritable optical media. *Nature Materials*, 3 (10):703–708, sep 2004.

[183] Noboru Yamada and Toshiyuki Matsunaga. Structure of laser-crystallized Ge2Sb2+xTe5 sputtered thin films for use in optical memory. *Journal of Applied Physics*, 88(12):7020–7028, nov 2000.

[184] S Privitera, E Rimini, C Bongiorno, R Zonca, A Pirovano, and R Bez. Crystallization and phase separation in Ge2+xSb 2Te5 thin films. *Journal of Applied Physics*, 94(7):4409–4413, sep 2003.

[185] M. Wakagi, K. Ogata, and A. Nakano. Structural study of a-Si and a-Si:H films by EXAFS and Raman-scattering spectroscopy. *Physical Review B*, 50(15):10666–10671, oct 1994.

[186] Walter K Njoroge, Han-Willem Wöltgens, and Matthias Wuttig. Density changes upon crystallization of Ge2Sb2.04Te4.74 films. *Journal of Vacuum Science Technology A: Vacuum, Surfaces, and Films*, 20(1): 230–233, jan 2002.

[187] B. Hyot. Chalcogenide for phase change optical and electrical memories. In *Chalcogenide Glasses*, pages 597–631. Woodhead Publishing, jan 2013.

[188] P. Arun and A. G. Vedeshwar. Phase modification by instantaneous heat treatment of Sb2S3 films and their potential for photothermal optical recording. *Journal of Applied Physics*, 79(8):4029–4036, apr 1996.

[189] Y. A. Sorb, V. Rajaji, P. S. Malavi, U. Subbarao, P. Halappa, S. C. Peter, S. Karmakar, and C. Narayana. Pressure-induced electronic topological transition in Sb 2 S 3. *Journal of Physics Condensed Matter*, 28(1):15602, jan 2016. ISSN 1361648X. doi: 10.1088/0953-8984/28/1/015602.

[190] Ilias Efthimiopoulos, Cienna Buchan, and Yuejian Wang. Structural properties of Sb2S3 under pressure: Evidence of an electronic topological transition. *Scientific Reports*, 6(1):1–9, apr 2016. ISSN 20452322. doi: 10.1038/srep24246.

[191] Saiful M. Islam, Lintao Peng, Li Zeng, Christos D. Malliakas, Duck Young Chung, D. Bruce Buchholz, Thomas Chasapis, Ran Li, Konstantinos Chrissafis, Julia E. Medvedeva, Giancarlo G. Trimarchi, Matthew Grayson, Tobin J. Marks, Michael J. Bedzyk, Robert P.H. Chang, Vinayak P. Dravid, and Mercouri G. Kanatzidis. Multi-states and Polyamorphism in Phase-Change K2Sb8Se13. *Journal of the American Chemical Society*, 140(29):9261–9268, jul 2018. ISSN 15205126. doi: 10.1021/jacs.8b05542.

[192] Jia Ming Liu. *Photonic devices*. Cambridge University Press, jan 2005.

[193] Louise F. Frellsen, Yunhong Ding, Ole Sigmund, and Lars H. Frandsen. Topology optimized mode multiplexing in silicon-on-insulator photonic wire waveguides. *Optics Express*, 24(15):16866, jul 2016.

[194] Alexander Y Piggott, Jesse Lu, Konstantinos G Lagoudakis, Jan Petykiewicz, Thomas M Babinec, and Jelena Vučković. Inverse design and demonstration of a compact and broadband on-chip wavelength demultiplexer. *Nature Photonics*, 9:374–377, may 2015.

[195] Bing Shen, Peng Wang, Randy Polson, and Rajesh Menon. Integrated metamaterials for efficient and compact free-space-to-waveguide coupling. *Optics Express*, 22(22):27175, nov 2014.

[196] Nicholas J. Dinsdale, Peter R. Wiecha, Matthew Delaney, Jamie Reynolds, Martin Ebert, Ioannis Zeimpekis, David J. Thomson, Graham T. Reed, Philippe Lalanne, Kevin Vynck, and Otto L. Muskens. Deep learning enabled design of complex transmission matrices for universal optical components. *ACS Photonics*, 8(1):283–295, jan 2021.

[197] David V. Tsu and Takeo Ohta. Mechanism of properties of noble ZnS-SiO2 protection layer for phase change optical disk media. *Japanese Journal of Applied Physics, Part 1: Regular Papers and Short Notes and Review Papers*, 45(8 A):6294–6307, aug 2006. ISSN 00214922. doi: 10.1143/JJAP.45.6294.

[198] Matthew Delaney, Ioannis Zeimpekis, Daniel Lawson, Daniel W. Hewak, and Otto L. Muskens. A New Family of Ultralow Loss Reversible Phase-Change Materials for Photonic Integrated Circuits: Sb2S3 and Sb2Se3. *Advanced Functional Materials*, 30(36):2002447, jul 2020.

[199] H Zhang, L Zhou, B M A Rahman, X Wu, L Lu, Y Xu, J Xu, J Song, Z Hu, L Xu, and J Chen. Ultracompact Si-GST Hybrid Waveguides for Nonvolatile Light Wave Manipulation. *IEEE Photonics Journal*, 10 (1):1–10, feb 2018.

[200] Weihua Wu, Yuemei Sun, Xiaoqin Zhu, Bo Shen, Jiwei Zhai, and Zhenxing Yue. Physical properties and structure characteristics of titanium-modified antimony-selenium phase change thin film. *Applied Physics Letters*, 118(8):081903, feb 2021. ISSN 00036951. doi: 10.1063/5.0024839.

[201] R. Parize, T. Cossuet, O. Chaix-Pluchery, H. Roussel, E. Appert, and V. Consonni. In situ analysis of the crystallization process of Sb2S3 thin films by Raman scattering and X-ray diffraction. *Materials & Design*, 121:1–10, may 2017.

[202] Pedro Vidal-Fuentes, Maxim Guc, Xavier Alcobe, Tariq Jawhari, Marcel Placidi, Alejandro Pérez-Rodriguez, Edgardo Saucedo, and Victor Izquierdo Roca. Multiwavelength excitation Raman scattering study of Sb2Se3 compound: fundamental vibrational properties and secondary phases detection. *2D Materials*, 6(4):45054, sep 2019.

Appendix

Film compositional analysis

The material properties of thin Sb_2S_3 and Sb_2Se_3 films were studied using Raman spectroscopy and XPS. Ioannis Zeimpekis performed the peak analysis for the Raman and XPS, as well as performing the XPS spectroscopy.

8.1.1 Raman

To confirm that the change in index seen after thermal crystallization, Raman spectroscopy was used to confirm that it was associated with crystallization, and not any other effect such as photo-darkening or a stoichiometric change. A 638 nm Raman laser was used to observe the vibrational modes present in each phase of both materials, without any capping layers. As seen in figure 8.1 two main peaks were easily detectable for the as-deposited (amorphous) Sb_2S_3 at 103 and 300 cm^{-1} [201], corresponding to the Sb-S and S=S vibrational nodes. The Sb_2S_3 film annealed at 270°C showed a very clear crystalline response, with sharp peaks for the modes of symmetry groups A_g at 125, 154, 284 and 312 cm^{-1}, $B1_g/B3_g$ at 240 cm^{-1} and $B2_g$ at 188 cm^{-1}. The mode at 188 cm^{-1} arises from Sb_2O_3, a thin surface oxide layer that forms during the uncapped anneal, despite the furnace being held under vacuum.

The as-deposited (amorphous) Sb_2Se_3 film again shows only broad peaks, indicative of an amorphous phase with numerous overlapping peaks. The peak at 190 cm^1 corresponds to the Sb_2Se_3, and the silicon substrate is visible as a sharp peak at 302 cm^1, do to the transparency of the film in visible wavelengths. The substrate was not visible in the Sb_2S_3 spectrum as it overlaps with the stronger modes from the material. The annealed Sb_2Se_3 sample (at 200°C) was found to be crystalline with strong A_g at 117, 190 and 211 cm^{-1} peaks, and two Bx_g at 150 and 153 cm^{-1} all corresponding to Sb_2Se_3 [160, 202]

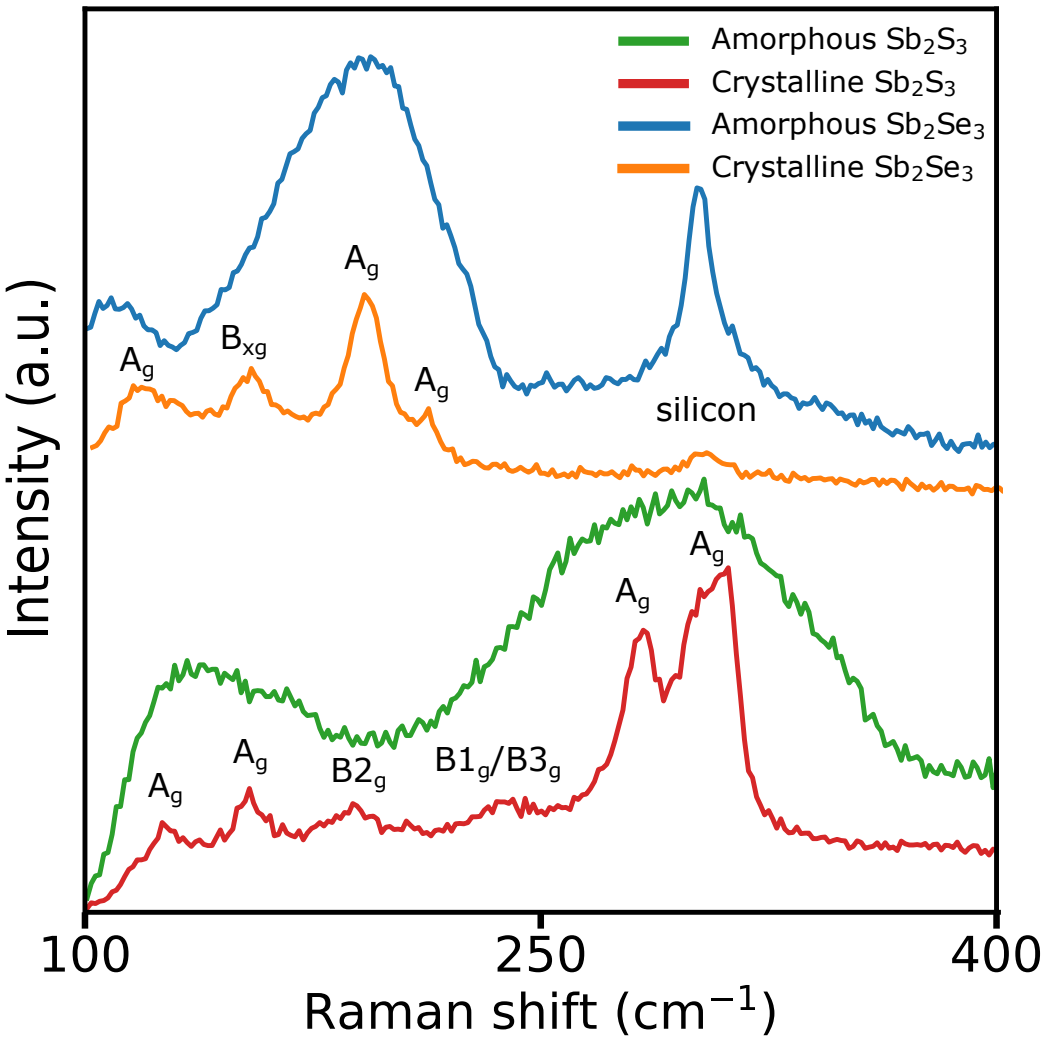

Figure 8.1: Raman spectrum for amorphous and crystalline Sb_2S_3 and Sb_2Se_3 films.

8.1.2 XPS

With a thermal process established that yielded high quality crystalline films, as characterized by Raman spectroscopy, the stoichiometry of the films was tested using X-ray photoelectron spectroscopy (XPS). To remove the thin native oxide layer that had formed on the samples, a 40 second ion beam

milling was used before the measurement was taken. The peaks were referenced to the adventitious carbon at 284.4 eV, and a flood gun was used to neutralize any charge energy shifting. The films were found to be close to the 2:3 stoichiometric ratio expected, however there was preferential sputtering of the S and Sb due to the lower atomic weights, leaving the films slightly chalcogen deficient. The atomic ratios were 44.95% Sb and 55.05% S in the Sb_2S_3, and 45.23% Sb and 54.77% Se in the Sb_2Se_3. Energy Dispersive X-Ray spectroscopy (EDX) showed the same result for films sputtered over a range of pressures and powers, with a 45:55 ratio being measured in all cases. Since the spin-orbit components of Sb 3d are well separated (by 9.4±0.2 eV), only the Sb 3d5/2 components are discussed here. In the case of Sb_2S_3, the 3d5/2 peak was found at 529.40 eV in line with literature. Trace amounts of metallic Sb showed up with a 3d5/2 peak centered at 528.28 eV. Despite the ion milling, a 3d5/2 peak from Sb_2O_3 surface oxidization can be seen at 530.12 eV, close to the elemental oxygen peak at 529.67 eV. A sulfur 2p3/2 peak at 161.46 eV is also seen.

The Sb_2Se_3 shows a similar result, with the main 3d5/2 peak at 529.74 eV. Again a metal Sb 3d5/2 peak arises at 529.15 eV, with surface oxide again present at 530.92 eV and a 1s oxygen peak at 530.69 eV. The reason for the 0.5 eV shift between the Sb_2S_3 and Sb_2Se_3 was attributed to a poor discharge during the prolonged run. As such the Sb_2Se_3 peaks are blue-shifted without affecting the carbon peak which was measured initially. The selenium peak was seen at 53.99 eV, again in line with published data.

Sputtering recipes

All materials used in this work were sputtered using an AJA RF sputter with an argon purge. A rotation carousel was used with no applied heating.

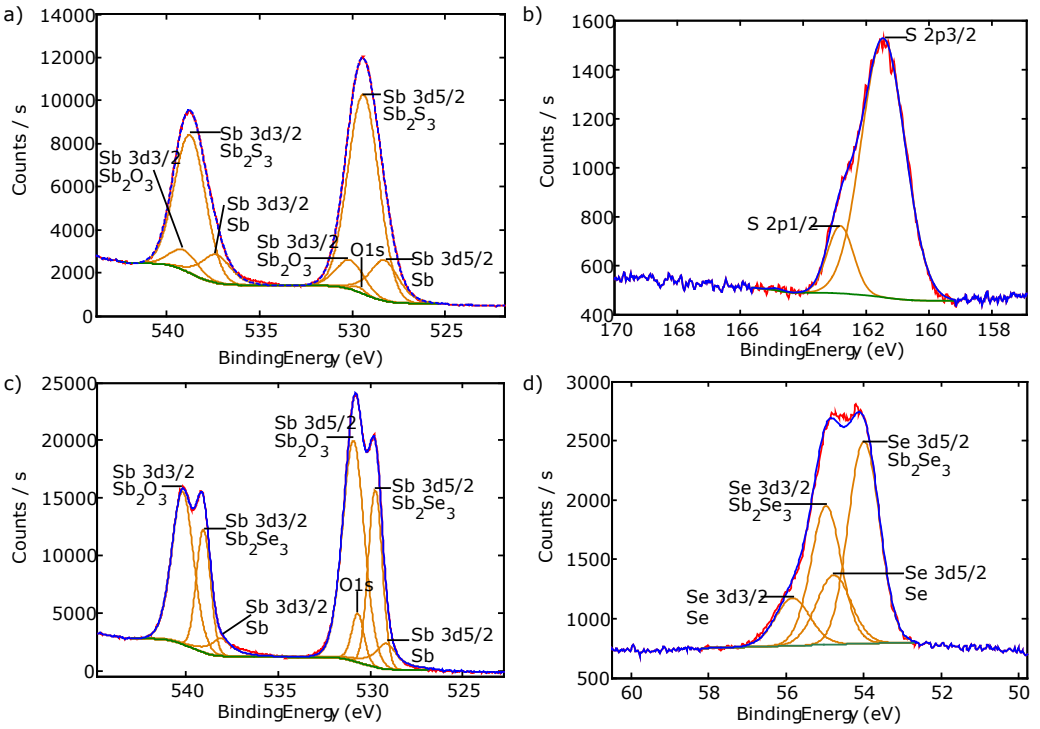

Figure 8.2: X-ray photoelectron spectroscopy of amorphous a,b) Sb_2S_3 and c,d) Sb_2Se_3.

Material	Sputtering Power (W)	Sputtering Pressure (mTorr)	Gas
$ZnS:SiO_2$	100	2	Ar
GST	100	1	Ar
Sb_2S_3	35	2	Ar
Sb_2Se_3	35	2	Ar

Table 8.1: Sputtering recipe for the different materials used.